An Imaging Ammeter for High Throughput Electrochemical Research

Submitted in partial fulfillment of the requirements for

the degree of

Doctor of Philosophy

in

Chemical Engineering

Reza M. Rock

BChE, Chemical Engineering, University of Delaware

Carnegie Mellon University

Pittsburgh, PA

May, 2013

Acknowledgement of support

The National Science Foundation supported this research under CBET 1133082. The doctoral committee for this thesis includes John R. Kitchin, Frederick Lanni and James B. Miller, along with doctoral advisors Paul J. Sides and Dennis C. Prieve.

Acknowledgements

To my friends, family, advisors and teachers at all stages of my life who have supported and guided me, I am eternally grateful. This work, and indeed most of what I have accomplished in my life thus far, would never have been possible without them.

My parents Andy and Melanie, and siblings Elias and Bilqis, have been there for me at every step along the way, making me into the person I am today. They continue to inspire me to work hard and try to make the world a better place, one little bit at a time.

I cannot imagine two people I would have rather spent my time in graduate school working with than Paul Sides and Dennis Prieve. Throughout my time at Carnegie Mellon, they have encouraged my growth as a researcher and as a person, and that mentorship has been an invaluable part of my experience here.

I would like to also thank all of the teachers who took a specific interest in me over the years. I can say with confidence that without people like Cyrus Ishikawa and Gail Ernst in MCPS, I would not be where I am today.

To every friend, colleague and relative not mentioned: thank you. If we are the sum of our experiences, every one of you is has been an important part of my journey to this point, and I look forward to learning and growing with you in the future.

Abstract

Rapid testing of electrocatalysts and corrosion resistant alloys accelerates discovery of promising new materials. Imaging amperometry, based on the deployment of colloidal particles as probes of the local current density, allows simultaneous electrochemical characterization of the entire composition space represented in a thin-film alloy "library" electrode. Previous work has shown that nanometer scale variations in particle-electrode distance for single particles in electric fields can be measured optically and translated into local current density, independent of electrical measurements. Implementation of this method to enable simultaneous measurements across non-uniform samples involves using a sparse, uniform layer of particles, which requires modification of previously existing theory and methods. Imaging individual particles for this application is infeasible at the low magnification levels needed to image an entire macroscopic (~1 square cm) sample. Mapping of electrochemical activity across the surface can be achieved nevertheless by imaging the entire electrode surface and gridding the resulting images into a mosaic of square “patch” areas 100 μm to a side, each containing 15-30 particles. The work presented in this dissertation shows that the integrated light intensity in each patch is the sum of the light scattering from all of the particles present in that patch, and that this total measured intensity can be used to infer the current density in the patch during electrochemical experiments.

In addition to scaling the imaging ammeter up to ensembles of particles, the theory for translating measured particle motion to current density has been substantially improved. These improvements involve proper modeling of the

current distribution on the electrode below the particles, which has a profound impact on the forces acting on each particle. This work demonstrates that the use of realistic kinetic models for the imaging ammeter is both vital and a discovered opportunity to increase its sensitivity. Finite element analysis was used to explore the variable space of the parameters involved, to better understand the impact of factors such as the current density and solution conductivity on the motion of the particles. Going forward, this information will be leveraged to improve the accuracy of the macroscopic imaging ammeter.

To complete the groundwork for the imaging ammeter laid out in this thesis, proof of concept experiments using a nickel/iron composition spread alloy film were performed. In a 1×5 mm^2 area containing alloy compositions from 20% iron to 100% iron, expected trends in electrochemical activity were observed during experiments, i.e. the current density as a function of voltage increased with increasing nickel content on the electrode surface. Future work will probe Fe/Ni alloy compositions with less iron, subsequently moving on to other binary and eventually ternary alloy systems.

Table of Contents

List of Tables

List of Figures

Chapter 1.

Chapter 2.

solutions in the limit of uniform current density and uniform potential on the electrode, respectively. The upwards and downwards triangles indicate FEM results in these same limits. The other points indicate FEM results for different values of J, at a fixed δ=0.0066.

Fig. 2.4. Force and potential are plotted for h* = 0.04. (a) Force on the particle in the z-direction is plotted against the angle coordinate, where ∠=0 indicates the bottom of the particle and ∠=π indicates the top. The force here is calculated by multiplying the stress at a given ∠ and multiplying by the differential wedge area $2\pi a^2 \sin(\angle)$. The solid line indicates the case of uniform potential on the electrode and the dashed line indicates the case of uniform current. The force on the top half of the particle is magnified in the inset, to clearly show the convergence and sign change. (b) The potential on the particle surface as a function of angle, relative to the potential at the top of the particle. With this frame of reference, convergence between the two curves is again observed for angles greater than π/2.

Fig. 2.5. Fluid flow streamlines calculated around a 10 μm particle given a uniform current density on the electrode under the particle, with h*=0.04, $\zeta_p = \zeta_w$, and $E_\infty = 33$ V/m. This plot illustrates the two separate circulation cells that exist given electroosmotic flow originating from the particle and the electrode. Streamline spacing is *not* indicative of fluid velocity.

Fig. 2.6. The ratio of F_{EP} to F_{EO} as a function of particle-wall separation, in the uniform current distribution limit and for four values of J, with δ=0.01. The increase with increasing h* is due to the diminishing impact of the electroosmotic flow originating at the electrode as the particle-electrode separation increases.

Fig. 2.7. F_{EP} and F_{EO} as a function of J and δ, for h*=0.02. As seen in Fig. 2.6, $F_{EP}^* > F_{EO}^*$ for $h^* > 0$, and that is seen here for all J and δ. As J becomes large, F_{EP}^* approaches C(h), which is 4.92 for h*=0.02. In that limit, F_{EO}^* approaches 0, as seen here.

Fig. 2.8. Two contours of the total force on the particle, where $F_{Tot} = 0.95F_{Yariv}$ and $F_{Tot} = 1.05F_{Yariv}$, plotted for $\zeta_p = \zeta_w = -100$ mV and $h^* = 0.06$. The intervening space represents a region of J and δ where Eq. 2.2 is accurate to within 5% of the actual force on the particle.

Fig. 2.9. Current density normal to the an electrode tangent a dielectric colloidal sphere, as a function of the radial distance away from the point of contact, normalized by the current density far from the particle. The inset shows the same data on a linear/log scale, to illustrate the behavior of the system at small values of r/a. The dotted line indicates data calculated assuming a uniform potential on the electrode surface.

electrokinetic forces F_{eo} and F_{ep} both pull the particle down towards the electrode surface. If E < 0, these forces would reverse direction as well.

Fig. 3.5. Schematic of the TIRM apparatus used in patch-level ensemble average experiments. The working electrode (WE) and counter electrode (CE) are conductive layers of ITO on glass slides. The reference electrode (RE) is a thin Ag/AgCl sheet sandwiched between two Teflon gaskets to ensure insulation and seal.

Fig. 3.6. (a)The probability density functions for simulated total scattering intensity (divided by the number of particles) and (b) the mean height h of ensembles of varying numbers of particles during open circuit experiments. Simulated parameters correspond to expected experimental values: a=2.65μm, ζ_p=-80mV, ζ_w=-123mV, $\sigma = 25\ \Omega^{-1}cm^{-1}$. I_0 is the intensity of light scattering when h=0. Note (see (b)) that the peak of the mean height distribution shifts from the most probable height of the particles, h_m, towards the time-averaged mean height of the particles, h_a, with increasing ensemble size.

Fig. 3.7. θ is the ratio of I_a measured in ensemble experiments, which is also the mean light scattering intensity of a single particle, to the actual average I_m for the particles in that ensemble, defined as the light scattering intensity of the particles at the minimum of their potential energy wells. The larger the particle, the more symmetric the probability distribution and the closer the mean and mode heights are to each other.

Fig. 3.8. Currents calculated from ensemble average electrochemical TIRM experiments, for particles of two sizes, with and without correcting the scattered light intensity to account for the difference between the mean of the scattering intensity distribution and the desired scattering intensity corresponding to the most probable height of the particles. The agreement is much improved when heavier particles, with smaller differences between the mean and mode heights, are used.

Fig. 3.9. Light scattering intensity measured from ensembles of particles adjacent to two portions of the same electrode: one region where the electrode surface was gold, and another region of exposed indium doped tin oxide (ITO), as a function of applied voltage vs. a Ag/AgCl reference electrode. From these raw intensity data, the differentiation between the two regions of the electrode is clear. Direction of the CV sweep is indicated by the arrow.

Fig. 3.10. The average of the most probable heights of particles in ensembles adjacent to two portions of the same electrode: one region where the electrode surface was gold, and another region of exposed indium doped tin oxide (ITO), as a function of applied voltage vs. a Ag/AgCl reference electrode. The particles over the gold portion of the electrode move in response to the electric field in

Fig. 4.4. Schematic of the working electrode surface with the Ni/Fe CSAF deposited on top. The CSAF was deposited in the middle of the glass slide, as pictured here. The composition on the CSAF surface are shown below. The red dotted rectangle represents the region over which imaging was performed in this study. Thanks to Matthew Payne for deposition and characterization of the CSAF electrode.

Fig. 4.5. Scattering intensities and current densities over the region of interest. (a) Light scattering intensity at open circuit. (b),(e) Light scattering during negative and positive polarization, respectively. (c),(f) Current density calculated with circular pillbox averaging during negative and positive polarization, respectively. (d),(g) Current density calculated averaging over 1×5 mm^2 patch regions during negative and positive polarization, respectively. In (c),(d),(f) and (g), lighter regions indicate greater positive current, with a maximum of 1 A/m^2.

Fig. 4.6. Current densities inferred from light scatter measurements as a function of applied voltage for the upwards sweep of a CV, averaged over ten cycles, for three different alloy compositions are plotted here. Also plotted in green is the mean current density across the entire electrode surface, measured electronically.

Fig. 4.7. The maximum current densities during the CV experiments described here, inferred from light scattering measurements, as a function of electrode composition, plotted as diamonds against the right ordinate axis. Also plotted against the left ordinate axis are current densities at a fixed overpotential of 360 mV on an alloy oxide electrode coated onto a nickel mesh support, as described by Landon et al. Both current densities trend downwards with increasing iron content in the electrode, above 20% iron. Axis scaling is arbitrary, and was chosen to illustrate the qualitative agreement between the two data sets.

Chapter 1

Introduction

1.0 Background

High throughput testing of electrocatalysts and corrosion resistant materials accelerates discovery. Some current methods for rapid testing utilize electrodes made from composition spread alloy films (CSAFs), which exhibit continuously varying surface concentrations.[1–6] While the use of these electrodes enables rapid testing of many different alloy compositions in parallel or rapid succession, location-specific electrochemical measurements are difficult to perform, and the optimal method combining flexibility, speed, and resolution has yet to be fully developed.[7–9]

Using classical electrochemical methods, testing of electrocatalyst alloy combinations is a time consuming and costly process, involving synthesizing multiple samples with different compositions and testing each individually.[7] Combinatorial screening of electrocatalysts allows for rapid testing of alloy compositions.[1–3] Some current methods for combinatorial screening involve the use of microelectrode array or composition spread alloy film (CSAF) samples, which have different alloy compositions at different locations on the sample.[4,10–14] Characterizing local electrochemical properties for different points on a single sample is difficult to do using traditional electrochemical methods, since these require the presence of electrolyte solution, which spreads across the entire electrode surface. The use of a scanning drop cell (SDC) electrode can be used to

circumvent this problem, and some imaging methods have also been investigated.[1–3,13,15–18]

SDC makes use of a small drop of electrolyte, radius 50-500 μm, at the bottom of a scanning tip. In this serial method, the tip rasters along the bottom electrode surface, stopping to perform electrochemical characterization at different points on the surface. Resolution of 1/10th of the drop diameter has been reported for this method, with particle diameters ranging from 1-500 μm.[17] This method has been used to characterize the electrochemical activity on an Al_xCu_{1-x} CSAF surface with continuously varying composition.[1] As this is a serial method, the measurement time for each location on the surface limits the amount of information that can be gathered in a reasonable amount of time. In a practical sense this greatly reduces the resolution of this method, since separate ~10 minute experiments must be performed at each point on the surface for which data is to be gathered. While this method has proven effective for characterizing binary alloy systems, time restraints limit the use of the method to these systems.

Imaging methods have also been proposed for determining electrochemical activity across inhomogeneous surfaces, which have the advantage of simultaneous measurements over the entire imaged surface. In 1992, Engstrom et al. demonstrated a method for imaging amperometry using pH sensitive Fluoroscein to indicate hydrogen evolution, followed by Reddington et al. who used quinine as a fluorescent pH indicator in 1998.[3,19] The test reaction in this work was the oxidation of methanol, which produces protons and changes the pH accordingly. This method is only valid for examining reactions that directly

affect the pH of the solution, and even when that condition is met, molecular diffusion makes it difficult to resolve features on a varying surface. In a more recent study, Shan et al. showed that surface plasmon resonance (SPR) could be used to measure electrochemical activity simultaneously at different points on an inhomogeneous surface: specifically, one which had a fingerprint deposited onto it.[18] Unsurprisingly, portions of the surface which were not covered by skin oils were more electrochemically active than portions which were. While this is a promising approach, only noble metal surfaces are candidates for SPR measurements, which reduces this method's scope.

These contributions indicate substantial interest in high throughput methods in the electrochemistry community. By imaging colloidal particles as probes of local electrochemical current, we are able to combine the strengths of SDC (accurate measurement, independent of reaction) with those of imaging techniques (rapid, parallel measurements over the entire surface). Although the method described here requires a transparent electrode and a constant ionic strength, its advantages should allow for rapid identification of new alloy combinations for electrocatalytic applications through the testing of electrochemical activity across CSAF surfaces.

1.1 Electrocatalysis of the oxygen evolution reaction

The work presented here explores the oxygen evolution reaction (OER) in alkaline solution as a test system. The OER is an electrochemical reaction implicitly linked to many energy storage problems through electrolysis of water for H^+ generation. The OER requires more energy than the opposing hydrogen

evolution reaction, and makes hydrogen evolution, as a whole, much less efficient than it could be since both reactions must progress at the same rate.[20] This is the motivation behind the search for effective, inexpensive electrocatalysts for the OER. Traditionally, alloy electrocatalyst samples are prepared and tested one alloy composition at a time— given the large composition space of alloy electrocatalyst systems, testing to determine the ideal composition is a time consuming proposition. Development of a method for rapidly testing a CSAF sample and analyzing the data would assist researchers in this field.

The OER is a convenient test reaction for the imaging ammeter for several reasons. TIRM is most accurate at very small particle-wall distances, meaning that it is a much better at detecting changes in particle height when the particles are being electrophoretically drawn towards the electrode than when they are being pushed away. The electrodes under investigation generally have a layer of oxide at the electrolyte interface, resulting in a large negative equilibrium charge on the surface. As such, negatively charged particles must be used in these experiments, as they can be levitated above the surface due to electrostatic repulsion. Conveniently, negative particles are drawn towards the electrode in the anodic current developed during oxygen evolution on the nearby electrode, enabling very accurate TIRM measurements.

Many alloy systems have been investigated for use in the OER. Trasatti reported results for mixtures of nickel and iron oxides and for mixtures of $NiCo_2O_4$ and FeO_x.[21] Mixing FeO_x and NiO_x, he found a “sharp maximum” in oxygen generation in the range of 10-20 mol% Fe.[22] Later, Trasatti found that the

mixed component system $NiCo_2O_4$ and FeO_x is effective in alkaline solutions, but reported only slight dependence on composition. The NiFe system represents an excellent basis for investigating the proposed method for high throughput screening of electrocatalysts. Enough is known about its performance to serve as a reference for the findings, and it is a technologically relevant system.

1.2 Motion of particles under the influence of an electric field

Microparticles adjacent to an electrode surface are levitated hundreds of nanometers from the surface, at an equilibrium height where the gravity, electrostatic repulsion, electrophoretic and viscous forces all sum to zero.[23,24] Microparticles levitated over an electrode surface are pictured in Fig. 1.1, where the bottom electrode is polarized positively with respect the top electrode. Given sufficient polarization, oxidation occurs at the bottom electrode, resulting in a positive electric field, and anodic current indicated by the large red arrow. The electric field results in an electrokinetic force felt by the negatively charged particles, which are attracted to the electrode, resulting in smaller average particle-wall separations. Were the direction of the electric field reversed, the particles would instead be propelled away from the bottom electrode, which would be passing cathodic current. It is important to note that the strength of the electrokinetic force acting on the particles, and therefore their departure from their equilibrium height, is dependent on the strength of the local electric field, which in turn is proportional to the local current density.

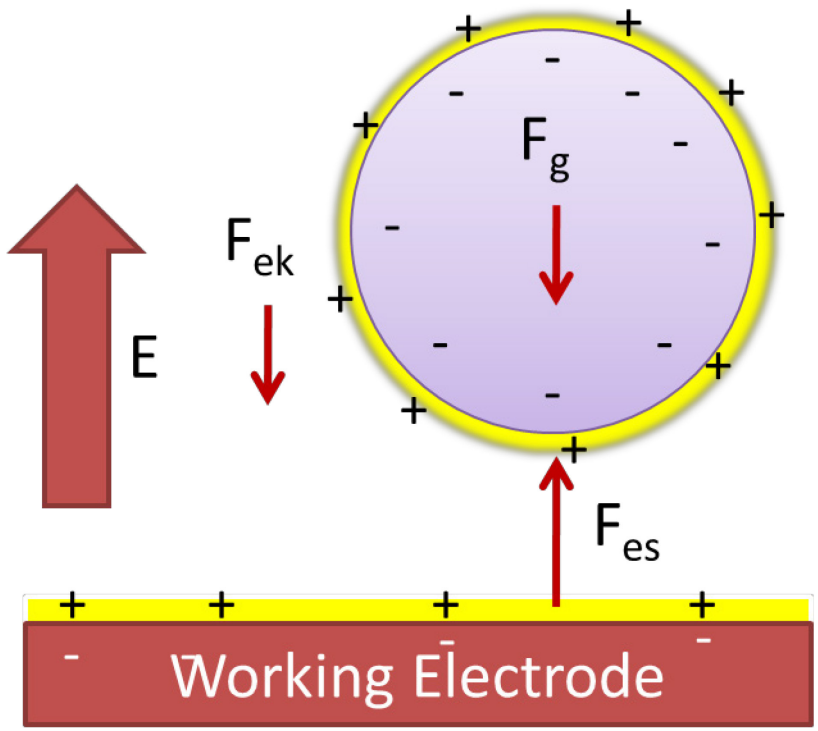

Fig. 1.1. Schematic of the particle-electrode system, where ζ_p and ζ_w are negative. Electrostatic repulsion pushes the particle away from the electrode while gravity pulls the particle down. With E > 0 as shown here, the sum of the electrokinetic forces F_{ek} pulls the particle down towards the electrode surface. If E < 0, F_{ek} would reverse direction as well.

1.3 Relationship between particle motion and current density

The distance between a colloidal particle and a nearby surface can be measured very accurately through the use of total internal reflection microscopy (TIRM).[25] In this method, a laser is directed at the electrode/electrolyte interface at an angle of incidence $\theta > \theta_c$, where θ_c is the critical angle for that interface, resulting in total internal reflection. An evanescent light wave forms which travels parallel to the interface and has an intensity that decays exponentially with distance from the interface. Fig. 1.2 is a schematic of a particle scattering light

from the evanescent wave. As the particle approaches the surface, light from the evanescent wave scatters more intensely. The scattering intensity can be measured and used to determine the absolute height of the particle with a height resolution of 1 nm.

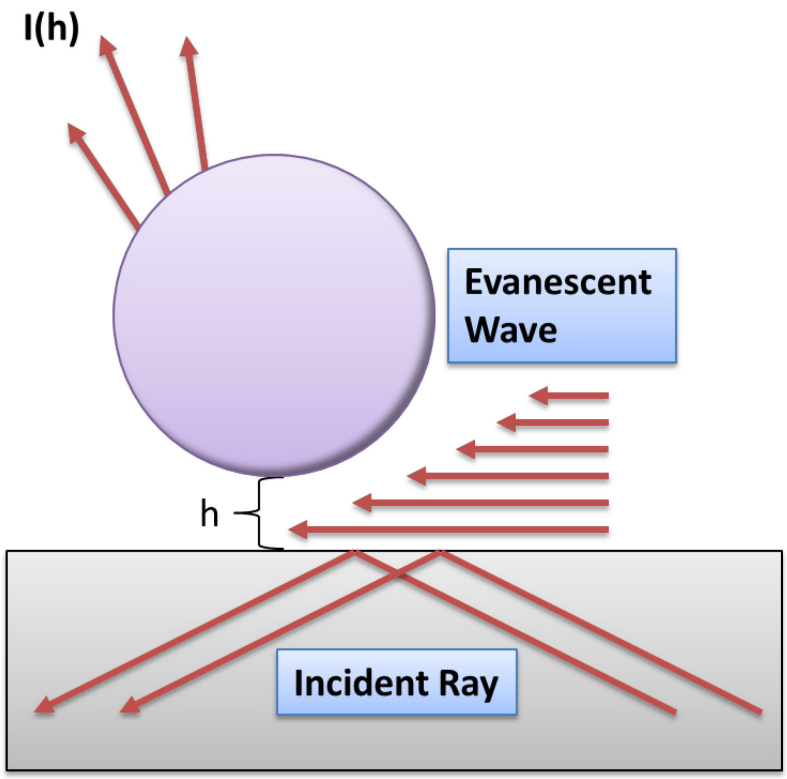

Fig. 1.2. A diagram of a particle scattering light during a TIRM experiment. Light strikes the interface from within a transparent electrode at an angle greater than the critical angle for that interface, engendering an evanescent wave adjacent to the interface. A particle in close proximity to the interface scatters light with an intensity I(h) that depends on the particle height h.

Averaging over long times or many cycles to eliminate Brownian fluctuations, the departure of the particle height from its equilibrium value can be used to determine the local electrochemical current density, as shown by Wirth et al.[26] Fig. 1.3 shows data from a cyclic voltammogram (CV), which shows current

density across an electrochemical cell as a function of applied potential. Inset are images taken of light from an evanescent wave scattering from sulfonated polystyrene particles levitated above the electrode. At middling voltages ($-0.5 < V < 0.7$), the only current being passed is from capacitive charging of the electrode double layer, and the scattering off the particles is visible, but not intense. As the applied voltage is increased, oxygen begins to evolve at the working electrode and anodic passes through the working electrode, drawing the particles closer to the electrode. This increases the scattering intensity, as seen by the larger and brighter dots in the top right inset as compared to the middle inset, where negligible current is passing through the electrode. At voltages less than -0.5 V, cathodic current is passed at the working electrode, and the particles are expelled away from the surface, out of the evanescent wave. In traditional single particle TIRM experiments, the light scattering intensity is measured with a photomultiplier tube (PMT), which measures total light intensity over the entire field of view with great accuracy and time resolution.[25] The integrated intensity of scattering of the ensembles shown in these insets can be measured in the same way.

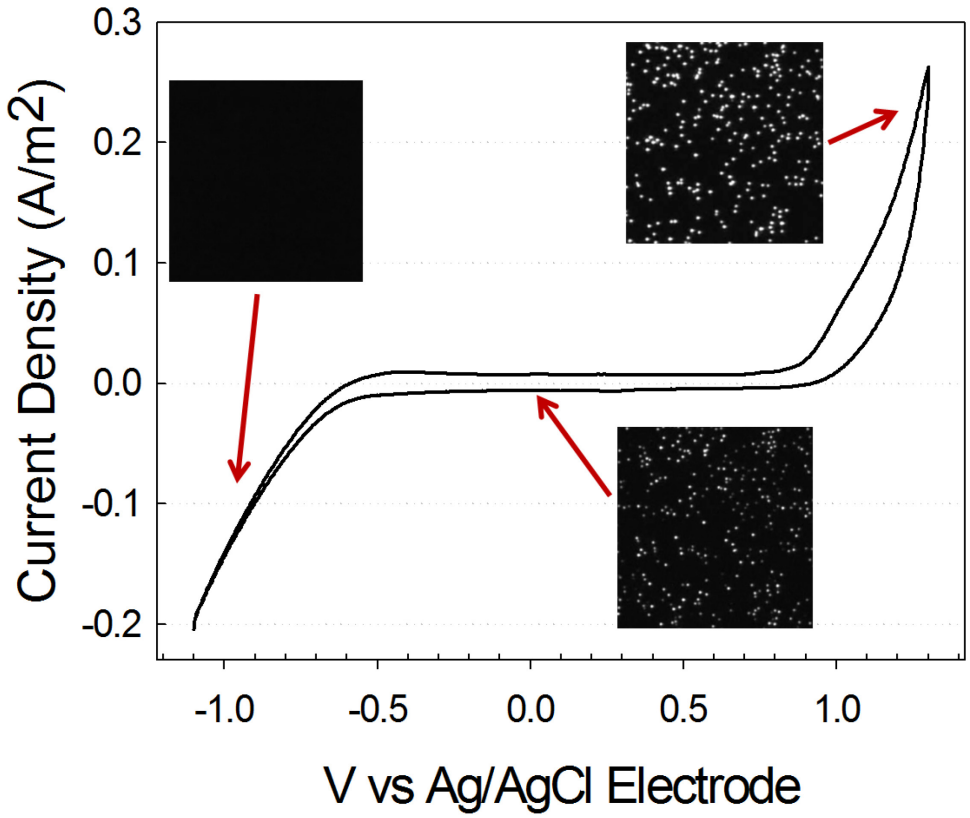

Fig. 1.3. Data from a cyclic voltammogram (CV), showing current density across an electrochemical cell as a function of applied potential. The surface here is tin-doped indium oxide (ITO), the particles are 10 μm sulfonated polystyrene bead and the electrolyte is 0.15 mM KOH. Inset are images taken of particles levitated above the electrode, scattering light from the evanescent wave with an intensity that corresponds to the distance between the particles and the wall. Positive current pulls the particles towards the electrode, and negative current drives them away.

Thesis Summary

The end goal of this project is to create maps of electrochemical activity for non-uniform macroscopic alloy samples, to identify the locations of greatest (or least) electrochemical activity. Previous work established the fundamental feasibility of this method, and this thesis represents the theoretical and experimental refinement and development of the imaging ammeter for

macroscopic CSAF electrodes. This work can be partitioned into three sections. Initial work involved refinement of the basic theory for translating particle motion into local current density, based on a computational study of the particle-electrode system. After this, the experimental and theoretical foundation for the imaging ammeter was expanded to allow for current determinations based on ensemble average light scatter measurements—a necessary step towards the macroscopic imaging ammeter. Finally, the new apparatus to allow for measurements of particle light scatter over large areas was constructed and used to probe electrochemical current as a function of applied voltage across a nickel/iron CSAF surface.

Accurate determination of current density from particle motion requires an accurate model for the relationship between the electric field strength local to the particles and the electrokinetic forces that act on those particles. The electrokinetic force acting on the particle is a strong function of the kinetics of the electrode reaction under the particle; for a given electric field, the force acting on the particle in the case of slow reaction kinetics can differ from the force acting on the particle in the case of fast reaction kinetics by an order of magnitude. Previous theoretical studies probed the limiting cases of infinitely fast and infinitely slow reaction kinetics, and developed expressions for the relationship between the electric field strength and the electrokinetic force on particles given these assumptions.[24,27,28] In the original imaging amperometry work by Wirth et al., the infinitely fast reaction kinetics assumption was invoked for the sake of simplicity,[26,29] but the actual reaction kinetics of these systems lies somewhere

between the two limiting cases. Finite element analysis was used to explore the variable space of the kinetic parameters involved, to better understand the impact of factors such as the current density and solution conductivity on the motion of the particles. This allowed for the determination of an empirical relationship between the reaction kinetics of the system and the magnitude of the electrokinetic forces acting on the colloidal particles adjacent to the electrode, which is applied in the later experimental work presented in this thesis.

The next step in the realization of the imaging ammeter was the theoretical and experimental adaptation of the method to allow for determination of current density from ensemble average light scattering measurements from many particles arrayed across a macroscopic CSAF electrode surface. Due to optical and computational constraints, imaging individual particles across the entire ~1cm^2 surface is not a feasible approach to the problem. Mapping of electrochemical activity across the surface can be achieved nevertheless by imaging the entire electrode surface and gridding the resulting images into a mosaic of square "patch" areas 100 μm to a side, each containing 15-30 particles. The work presented in Chapter 3 demonstrates that the integrated light intensity in each patch is the sum of the light scattering from all of the particles present in that patch, and that this total measured intensity can be used to infer the current density in the patch during electrochemical experiments. This requires a correction to the collected data to address the fact that the ensemble average intensity values measured to not correspond directly to the minimum energy location of the particles. This correction was derived and applied to the collected

data, resulting in much improved agreement between current densities inferred from particle scatter and externally measured current densities.

Additionally, light scatter from colloidal particles over different regions on an electrode surface with two areas of differing electrochemical activity (one region 100% gold, one region 100% ITO) was measured and used to infer current densities for each corresponding electrode region. Since gold is a much better catalyst for the OER than ITO, the difference in particle motion above the two regions of the electrode was well pronounced. The currents inferred from the light scatter measurements corresponded to the actual current densities passing through these two regions of the same electrode, as well.

The final experiments were performed with a new experimental apparatus that allows for optical measurements of macroscopic samples. To illuminate particles across the entire macroscopic sample, the new apparatus involves treating the working electrode as a wave guide, which results in multiple reflections of the laser onto the surface of interest. These experiments provide final proof-of-concept for the imaging ammeter, by inferring the current over a 1×5 mm region of a binary Fe/Ni CSAF electrode from the motion of colloidal particles during electrochemical experiments. The inferred currents agree with established trends for that alloy system.[20]

<u>Major accomplishments of this thesis:</u>

1. Development of an empirical relationship between electrode kinetics and the electrokinetic forces acting on particles proximate to the electrode. This allows

for more accurate determination of current density from particle motion measurements.

2. Development of theory and experimental techniques to allow for quantitative imaging amperometry from ensemble average TIRM measurements. This was a necessary step towards the macroscopic imaging ammeter.
3. Proof of concept experimentation of the macroscopic imaging ammeter, probing electrochemical activity across an iron/nickel binary alloy electrode film. Observed trends agree with the established behavior of this alloy system.

1.4 Works Cited

(1) Klemm, S. O.; Kollender, J. P.; Walter Hassel, A. *Corrosion Science* **2011**, *53*, 1–6.

(2) Mardare, A. I.; Yadav, A. P.; Wieck, A. D.; Stratmann, M.; Hassel, A. W. *Science and Technology of Advanced Materials* **2008**, *9*, 035009.

(3) Reddington, E. *Science* **1998**, *280*, 1735–1737.

(4) Prochaska, M.; Jin, J.; Rochefort, D.; Zhuang, L.; DiSalvo, F. J.; Abruña, H. D.; Van Dover, R. B. *Review of Scientific Instruments* **2006**, *77*, 054104.

(5) Jin, J.; Prochaska, M.; Rochefort, D.; Kim, D.; Zhuang, L.; Disalvo, F.; Vandover, R.; Abruna, H. *Applied Surface Science* **2007**, *254*, 653–661.

(6) Priyadarshini, D.; Kondratyuk, P.; Miller, J. B.; Gellman, A. J. *Journal of Vacuum Science & Technology A: Vacuum, Surfaces, and Films* **2012**, *30*, 011503.

(7) Smotkin, E. S.; Diaz-Morales, R. R. *Annu. Rev. Mater. Res* **2003**, *33*, 557–79.

(8) Muster, T. H.; Trinchi, A.; Markley, T. A.; Lau, D.; Martin, P.; Bradbury, a.; Bendavid, a.; Dligatch, S. *Electrochimica Acta* **2011**, *56*, 9679–9699.

(9) Neirinck, B.; Van der Biest, O.; Vleugels, J. *The Journal of Physical Chemistry. B* **2012**.

(10) Jiang, R. *The Review of Scientific Instruments* **2007**, *78*, 072209.

(11) Russell, A. E. *Physical Chemistry Chemical Physics : PCCP* **2008**, *10*, 3607–8.

(12) Spong, a *Journal of Power Sources* **2003**, *119-121*, 778–783.

(13) Mardare, A. I.; Ludwig, A.; Savan, A.; Wieck, A. D.; Hassel, A. W. *Electrochimica Acta* **2009**, *54*, 5171–5178.

(14) Whitacre, J. F.; Valdez, T. I.; Narayanan, S. R. *Electrochimica Acta* **2008**, *53*, 3680–3689.

(15) Williams, C. G.; Edwards, M. a; Colley, A. L.; Macpherson, J. V; Unwin, P. R. *Analytical chemistry* **2009**, *81*, 2486–95.

(16) Hassel, A. W.; Seo, M. *Electrochimica Acta* **1999**, *44*, 3769–3777.

(17) Lohrengel, M. M.; Moehring, A.; Pilaski, M. *Fresenius' Journal of Analytical Chemistry* **2000**, *367*, 334–9.

(18) Shan, X.; Patel, U.; Wang, S.; Iglesias, R.; Tao, N. *Science (New York, N.Y.)* **2010**, *327*, 1363–6.

(19) Engstrom, R. C.; Ghaffari, S.; Qu, H. *Anal. Chem.* **1992**, 2525–2529.

(20) Landon, J.; Demeter, E.; Nilay, I.; Keturakis, C.; Wachs, I. E.; Vasic, R.; Frenkel, A. I.; Kitchin, J. R. *ACS Catalysis* **2012**, *2012*, 1793–1801.

(21) Guerrini, E.; Piozzini, M.; Castelli, A.; Colombo, A.; Trasatti, S. *Journal of Solid State Electrochemistry* **2007**, *12*, 363–373.

(22) Krstajić, N.; Trasatti, S. In *Oxygen Electrochemistry*; Adzic, R.; Anson, F.; Kinoshita, K., Eds.; The Electrochemical Society, 1996; pp. 155–165.

(23) Prieve, D. C.; Sides, P. J.; Wirth, C. L. *Current Opinion in Colloid & Interface Science* **2010**, *15*, 160–174.

(24) Yariv, E. *Journal of Fluid Mechanics* **2010**, *645*, 187.

(25) Prieve, D. *Advances in Colloid and Interface Science* **1999**, *82*, 93–125.

(26) Sides, P. J.; Wirth, C. L.; Prieve, D. C. *Electrochemical and Solid-State Letters* **2010**, *13*, F10–F12.

(27) Keh, H.-J.; Lien, L.-C. *J. Chin. Inst. Chem. Eng.* **1989**, *20*, 283–290.

(28) Solomentsev, Y.; Bohmer, M.; Anderson, J. L. *Langmuir* **1997**, *13*, 6058–6068.

(29) Wirth, C. L.; Sides, P. J.; Prieve, D. C. *Journal of Colloid and Interface Science* **2011**, *357*, 1–12.

Chapter 2

The effect of electrode kinetics on electrophoretic forces

Reproduced in part from:

"The effect of electrode kinetics on electrophoretic forces", R.M. Rock, P.J. Sides, D.C. Prieve, Journal of Colloid and Interface Science 393 (2013) 306.

2.0 Abstract

Electric fields are commonly used to deposit colloidal particles on electrode surfaces and can even be used in directed assembly. The electric field beneath each particle changes as the particle approaches the wall; the proximity of the wall breaks the fore/aft symmetry and drives complicated flows that exert forces on the particle. While two limiting cases have been partially analyzed, constant electrode potential and uniform current density, the full problem has not been explored. Here, the electroosmotic flows in the region between the particle and the electrode are analyzed and the forces are computed for arbitrary electrode kinetic boundary conditions. Finite element analysis is employed to explore the current distribution beneath a particle and its impact on the net force acting on the particle. Previously established dimensionless kinetic parameters are used to scale between the two limiting cases. The forces on particles are an order of magnitude larger than the bulk electrophoretic force and are profoundly sensitive to the current distribution beneath the particle as it approaches the electrode.

2.1 Introduction

Electrokinetic flows around insulating colloidal particles in close proximity to an electrode surface of like charge can move individual particles and particle aggregates both in the direction of the imposed field and orthogonally to it, with implications for colloidal assembly, electrophoretic deposition, and colloidal sensing.[1–8] Long-range repulsive and attractive lateral forces between these particles arise in the presence of AC or DC electric fields perpendicular to the electrode surface. These forces lead to particle aggregation and the formation of colloidal crystal lattices.[1,2,4,5,8–10] Exploitation of this self-assembly has been proposed as a method for fabrication of a variety of devices such as photonic crystals, for a variety of applications.[5,11,12]

Theory and experiment have established that the motion of particles is a result of mutual entrainment in toroidal fluid flow originating from the interaction of an imposed electric field with the electric double layer of the particle, and in some cases, with the double layer of the electrode beneath the particle.[2,4,13,14] Experimental studies have been performed in DC electric fields to probe interactions between particle pairs and particle ensembles, resulting in an empirical understanding of how this behavior changes with particle separation and concentration, as well as other control parameters such as electric field direction and cell confinement.[9,12] Much of the theoretical work in this field has focused on determination of the flow profiles in the vicinity of the particle, to determine what impact this flow might have on neighboring particles. The boundary condition used on the electrode surface has a profound impact on the magnitude of the

electric field underneath the particle, and thereby affect fluid flow and pressure gradients that determine the force on the particle and its neighbors.

As a dielectric colloidal particle approaches an electrode, the geometric constraint of passing current through the gap between the electrode and the particle alters the relationship between current density and electric potential under the particle. To our knowledge this problem has been treated only in two limiting cases: either the electrode potential is uniform and the normal current density is non-uniform, or the current density is uniform and the potential is non-uniform.[9,13–17] These two conditions are termed the primary and uniform current distributions, respectively.[18] The primary current distribution occurs in the limit of infinitely fast reaction kinetics and low solution conductivity, while the uniform current distribution occurs in the limit of infinitely slow reaction kinetics and high solution conductivity. In other words, the primary current distribution develops when the only resistance to current is ohmic resistance in the electrolyte, and the secondary current distribution develops when the only resistance to current is the slow electrochemical kinetics at the electrode.

The simpler of these two cases is the primary current distribution because the uniform potential does not generate electroosmotic flow along the electrode.[9,15] This condition also generates a minimum electroosmotic flow originating near the particle. A uniform current distribution does, however, drive substantial electroosmotic flow on the surface of the electrode under the particle, due to the tangential electric field adjacent to that surface. This potential gradient

on the electrode also accentuates the gradient on the particle surface, resulting in increased electroosmotic flow there as well.[13]

The consequence of these considerations is that the electrokinetic force on the particle perpendicular to the wall depends strongly on the details of the electrical boundary condition on the electrode surface. Regardless of the boundary condition on the electrode, the perpendicular force increases as the particle approaches the electrode surface, due to a combination of changes in the pressure gradient around the particle and the potential gradient along the particle surface. We refer to the force on the particle due to electroosmotic flow along the particle as the electrophoretic force, F_{EP}. Additionally, if the potential on the electrode surface is not uniform, a force resulting from these effects is present and referred to here as the electroosmotic force, F_{EO}. Like the distribution of current density itself, these forces have also only been systematically studied in the limits of the primary and uniform current distribution. For a wide range of physical and electrochemical parameters, the total electrokinetic force in these two cases can differ by an order of magnitude or more and varies continuously between the extremes.[13–15,19] In this work, we examine these forces on the particle as a function of the current distribution on the electrode and around the particle. Finite element analysis is used to explore the effect of boundary conditions between the two limiting cases. The goal is to quantify the relationship between the force on the particle and the physicochemical conditions that determine the current distribution, such as electrode kinetic constants and electrolyte conductivity.

The current distribution itself under a particle in contact is also examined as a function of these same parameters, to provide a greater understanding of how the environment under the particle changes with changing electrode conditions. This computational approach follows the theoretical work other researchers have done to investigate the current distribution on axisymmetric surfaces and around particles, and allows for exploration of the variable space between the two limiting cases of uniform potential and uniform current density on the electrode surface.[20,21]

2.2 Theory

2.2.0 Uniform potential and uniform current density

Consider a single colloidal particle separated from an electrode by distance h, as in the axisymmetric domain shown in Fig. 2.1. Given sufficient like charges on the electrode and the particle surface, the downward force of gravity on the particle and electrostatic repulsion between the particle and the electrode balance one another, resulting in an effective equilibrium separation distance h_{eq} between the particle and the wall. Force balances and potential energy distributions for these particles have been explored in previous works.[3,22] When current flows through the electrode surface, a potential gradient develops in the z-direction, resulting in electroosmotic flow originating from the action of the electric field on the diffuse part of the electric double layer of the particle. Similarly, an electric field may also develop along the electrode surface, which can act on the diffuse part of the electrode's double layer to drive electroosmotic flow along that interface.

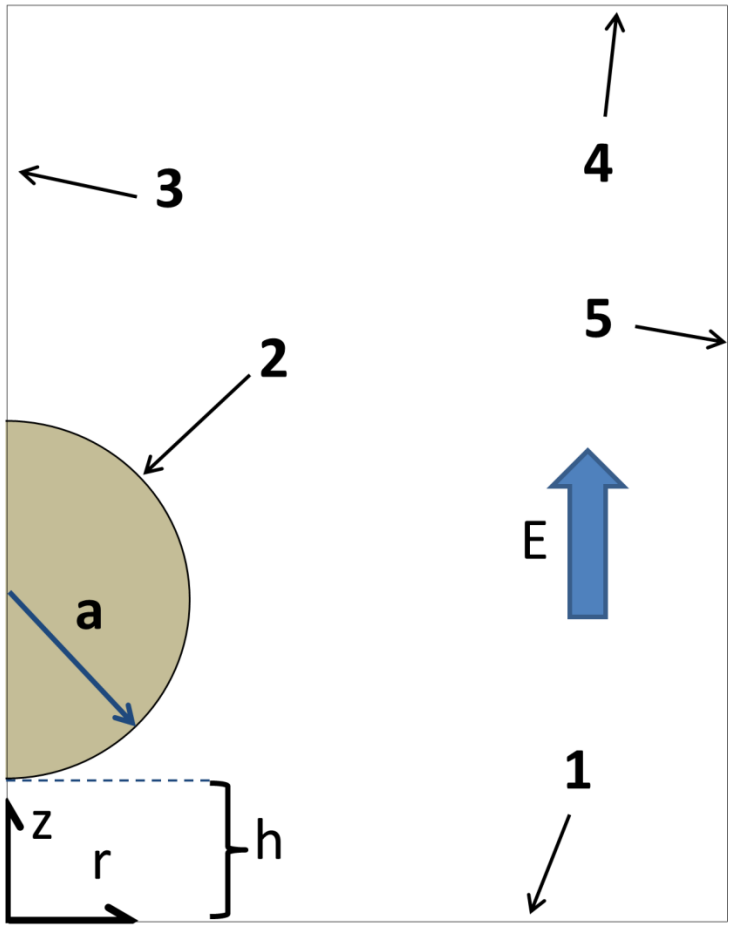

Fig. 2.1. A schematic of the axisymmetric domain space simulated in these studies. Numbered interfaces indicate boundaries at which boundary conditions are applied. E indicates the electric field, positive in this work, and h indicates the particle-wall separation. A and B refer to the electroosmotic flow originating in the double layer of the particle and electrode, respectively. The particle-wall separation is indicated by h. Boundaries 1, 2, and 3 correspond to the electrode, particle and axisymmetric axis, respectively, while 4 and 5 are open fluid boundaries.

The tangential electric fields along the particle and electrode surfaces both depend on the distribution of the electric potential at the electrode, $\phi|_{z=0}$, which is defined as the potential of a reference electrode of the same kind as the working electrode and located just outside the diffuse layer.[13,15,23] Two limiting cases bound the range of possible potential distributions. When the electrode offers no

electrochemical charge transfer resistance to current, $\phi|_{z=0}$ equals the applied voltage V_0 at every location on the surface, and the tangential electric field $E_r|_{z=0} = 0$. Given the uniform driving force for current on the electrode surface and the large ohmic resistance resulting from the constrained geometry under the particle, a non-uniform current distribution develops under the particle, known as the primary current distribution.[18] The primary current distribution for an insulating sphere tangent to an electrode surface, one limiting case of this problem, was described in 1980.[21]

A very different limiting behavior occurs when the electrochemical kinetic barrier to current at the electrode is very high and the ohmic resistance in the electrolyte very low; this combination results in a uniform current distribution on the electrode under the particle. If the current density normal to the electrode is uniform and if the particle is very close to the wall ($h/a \ll 1$, where a is particle radius), the current density in the electrolyte between the particle and the wall significantly exceeds the current density far from the particle. Since current is passing through the electrolyte under the particle, a radial potential gradient appears in the electrolyte adjacent to the electrode; that is to say, $E_r|_{z=0} \neq 0$. The potential immediately adjacent to the electrode surface and the current normal to the electrode are shown in Fig. 2.2 as a function of radial distance from the bottom of a tangent insulating particle, for the uniform current density and uniform potential cases, respectively. These data were computed numerically following the method described in this work, for a current density far from the

particle of +0.1 A/m^2, a particle size of a=5μm and a solution conductivity of 30 μS/cm.

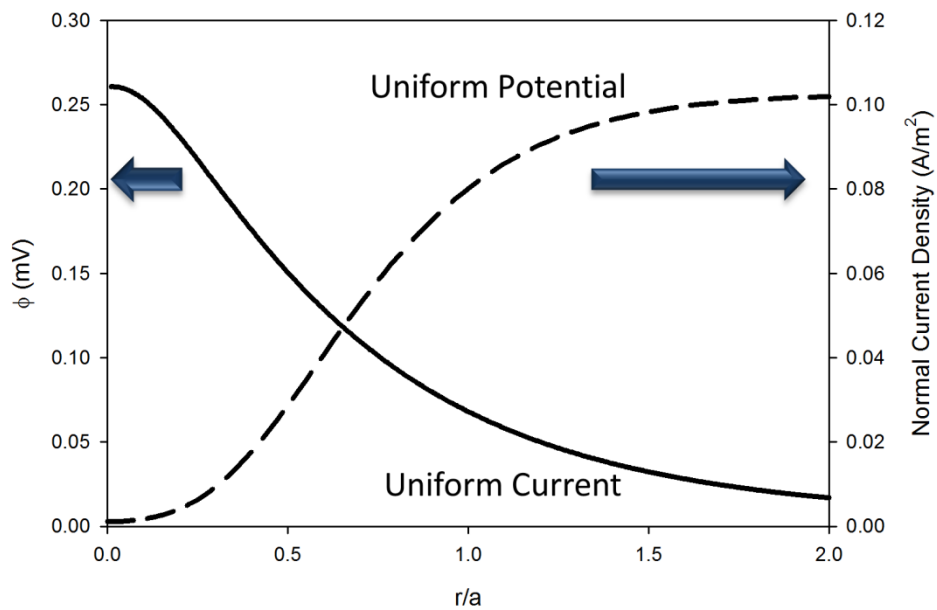

Fig. 2.2. Potential and normal current density on the electrode surface are plotted against radial distance from r=0, directly beneath the particle, for h/a=0.04 and $E_\infty = 33\ \mathrm{V/m}$. The dashed line indicates the current density given a uniform potential distribution on the electrode: this is the primary current distribution. The solid line indicates the potential given a uniform current density on the electrode, relative to the electrode potential far from the particle.

In the limit of an infinitesimally thin double layer, any tangential component of the electric field appears to cause the fluid to "slip" along a charged solid surface at a speed given by Smoluchowski's equation:

$$u_t = \frac{\varepsilon \zeta E_t}{\mu}$$

where u_t is the fluid velocity tangent to the surface, ζ is the zeta potential of the surface (either particle ζ_p or electrode ζ_w), E_t is the electric field tangent to the

surface, and μ is the viscosity of the electrolyte. In the example of E>0 and $\zeta_p < 0$, the direct action of the electric field on the negatively charged particle pulls it toward the electrode while the same electric field acts to push the positively charged cloud of counterions away from the electrode and up over the surface of the particle; the net electrophoretic force on the particle is downward and denoted by F_{EP}. As the particle approaches the wall, both the electric field tangent to the particle surface and the hydrodynamic resistance to movement of the particle increase. Assuming a primary current distribution under the particle, Keh & Lien[15] calculated the electrophoretic mobility of the particle as a function of h, and Solomentsev et al. [9] offered an expression for the electrophoretic force, F_{EP}, on the particle, given by Eq. 2.1.

$$F_{tot} = F_{EP} = 6\pi\varepsilon a\zeta_p E_\infty C(h) \qquad (2.1(a))$$

$$C(h) = \frac{h+1.554a}{h+0.300a} \qquad (2.1(b))$$

where E_∞ is the electric field far away from the particle, ε is the dielectric permittivity of the electrolyte, $F_{bulk} = 6\pi\varepsilon a\zeta_p E_\infty$ is the electrophoretic force the particle feels far away from the wall in the limit of an infinitesimally thin double layer, and C(h) is a correction for the proximity of the wall. As the particle approaches the wall (h→0), C(h) approaches a constant value of 5.18, and at large h, C(h) approaches unity, indicating that $F_{EP} = F_{bulk}$. It is important to note again that in this limit, there is no electroosmotic flow along the electrode because $\phi|_{z=0}$ is uniform over the electrode surface.

In the limit of a uniform current density under the particle, a non-zero potential gradient exists on the electrode surface under the particle, as shown in Fig. 2.2. This electric field component drives radial electroosmotic flow along the electrode, in addition to the electroosmotic flow on the particle surface. The entrainment force from the flow on the electrode, F_{EO}, can be of the same order of magnitude as the electrophoretic force on the particle, F_{EP}. In the limit of thin double-layers and small particle-wall separation, Yariv[13] calculated the combined electrophoretic and electroosmotic force on the particle, shown in Eq. 2.2.

$$F_{tot} = F_{EP} + F_{EO} = 3\varepsilon\pi E_{\infty}\left(\frac{a^2}{h}\right)\left(\zeta_w + \zeta_p\right) \qquad (2.2)$$

Here, ζ_w is the zeta potential of the electrode. The equal weighting of ζ_w and ζ_p in this equation indicates that, at infinitesimally small particle-wall separations, $F_{EO} = F_{EP}$ if the two zeta potentials are equal. Yariv[13] points out that in the limit of $h \to 0$ most of the contribution to either force arises from the narrowest region of the gap between the sphere and the plate where the two surfaces are virtually parallel to each other. In this limit, the tangential component of the electric field is independent of z and thus the same for either surface.

Given that Yariv's analysis applies only asymptotically as $h \to 0$, it should not be applied when the particle is far from the electrode; the boundary conditions on the electrode as well as ζ_w become irrelevant and $F_{tot}|_{h\to\infty} = F_{bulk}$.

2.2.1 The intermediate case: nonuniform current density and potential

The current distribution in the general case falls somewhere between these two special cases. A more general boundary condition on the electrode surface is the Bulter-Volmer equation which relates the current density to the potential via the kinetics of the electrode reaction:

$$i_z = i_0 \left\{ \exp\left[\frac{\alpha_a F}{RT}\left(V_0 - \phi|_{z=0}\right)\right] - \exp\left[\frac{-\alpha_c F}{RT}\left(V_0 - \phi|_{z=0}\right)\right]\right\} \quad (2.3)$$

In this equation, i_z is the normal current density at the electrode, i_0 is the exchange current density of the electrode material, α_a and α_c are anodic and cathodic symmetry coefficients, respectively, F is the Faraday constant, R is the gas constant, T is the temperature, and V_0 is the voltage applied to the electrode. Linearizing this expression around $V_0 - \phi|_{z=0} = 0$ and stating it in terms of the electric field on the electrode gives

$$\left.\frac{\partial\phi}{\partial z}\right|_{z=0} = i_0 \frac{(\alpha_a+\alpha_c)F}{\sigma RT}\left(V_0 - \phi|_{z=0}\right) \quad (2.4)$$

where σ is the conductivity of the electrolyte. This expression can be nondimensionalized by scaling the electric potential with V_0 and the axial distance z with the radius of the particle. Grouping the constants on the right hand side of the resulting expression, one obtains a dimensionless group that represents the ratio of the ohmic resistance to current in the electrolyte to the kinetic resistance to current at the electrode. This group, J, is given in Eq. 2.5. [24]

$$J \equiv \frac{(\alpha_a+\alpha_c)aF}{\sigma RT} i_0 \quad (2.5)$$

When $i \ll i_0$ and $V_0 - \phi$ is small compared to RT/F, J uniquely characterizes the current distribution under the particle, as demonstrated by Newman.[18] At large values of J, the charge transfer kinetics are fast and the ohmic resistance in the electrolyte is large, which leads to the uniform potential electrode condition. As J becomes small, kinetic resistance at the electrode dominates, yielding the uniform current distribution condition.

At large current densities, such as $i \gtrsim i_0$, linearization of Eq. 2.3 is no longer possible, and an additional parameter, δ, becomes important in determining the distribution of current and potential under the particle.[20]

$$\delta \equiv \frac{(\alpha_a+\alpha_c)aF}{\sigma RT} i_{avg} \tag{2.6}$$

Here, i_{avg} is the current density on the electrode far from the particle. When $i \gg i_0$, δ has a qualitatively similar impact on current distribution as J does when $i \ll i_0$. When $i \approx i_0$, the current and potential distribution under the particle is affected by both J and δ if they are within a few orders of magnitude of each other. To calculate the force on the particle, three other quantities are needed: the ratio of the particle-wall separation to the radius of the particle, h* = h/a, and the zeta potentials of the particle and the electrode.

2.2.2 Equations and boundary conditions

In the limit of an infinitesimally thin double layer, where the Debye length of the electrolyte is substantially shorter than the other length scales in the system, the fluid is electrically neutral virtually everywhere and the problem of

determining the electrostatic potential is decoupled from the mass-transfer and fluid flow problems. The electric potential is calculated first by solving Laplace's equation with current conservation at every point in the domain, given by Eq. 2.7.

$$\nabla \cdot \mathrm{i} = 0 \tag{2.7(a)}$$

$$\mathrm{i} = \sigma \mathrm{E} \tag{2.7(b)}$$

$$\mathrm{E} = -\nabla \phi \tag{2.7(c)}$$

Here, i is the current density vector and E is the electric field strength. Next, the fluid flow is calculated from Stokes equation with continuity as seen in Eq. 2.8.

$$0 = -\nabla \mathrm{p} + \mu \nabla^2 \mathrm{u} \tag{2.8(a)}$$

$$\nabla \cdot \mathrm{u} = 0 \tag{2.8(b)}$$

Where u is the velocity vector of the fluid and p is the pressure.

The electric field boundary conditions are the Butler-Volmer equation at the electrode, axial symmetry at the axis of the particle, ground at the boundary opposite the electrode and insulation on the particle and the last boundary. The fluid flow boundary conditions are Smoluchowski flow along the particle and electrode surfaces, axial symmetry at r=0 and open boundaries at the other edges. The domain and boundary equations are shown in Table 2.1, numbered by the boundaries given in Fig. 2. The thin double layer approximation for the electric double layer is implicit in these expressions.

Table 2.1. Computational boundary conditions.

Boundary	EC BC	Fluids BC
1	$-\sigma \frac{\partial \phi}{\partial z}\Big\|_{z=0} = i_0 \left\{ \exp\left[\frac{\alpha_a F}{RT}(V_0 - \phi\|_{z=0})\right] - \exp\left[\frac{-\alpha_c F}{RT}(V_0 - \phi\|_{z=0})\right]\right\}$	$u_r = \frac{\varepsilon \zeta_w E_r}{\mu}$
2	$n \cdot i = 0$	$u_t = \frac{\varepsilon \zeta_p E_t}{\mu}$
3	$\frac{\partial \phi}{\partial r} = 0$	$\frac{\partial u}{\partial r} = 0$
4	$\phi = 0$	$n \cdot T = 0$
5	$n \cdot i = 0$	$n \cdot T = 0$

In the equations of Table 2.1, n is the vector normal to the interface and T is the total stress tensor, including contributions from viscous stress and isotropic pressure, but not the electrical Maxwell stress. Analytical analyses of this type of problem commonly specify a uniform electric field as an asymptote at infinity for mathematical convenience. The analogous condition would be specification of a uniform field on boundary 4, with $\partial\phi/\partial z = -i_{avg}/\sigma$, instead of the zero (ground) voltage used here.[13,15] In this numerical analysis specifying either the average flux or a uniform potential on boundary 4 are functionally equivalent conditions, if the distance between boundaries 1 and 4 is many times the particle

diameter. In this analysis, we chose to specify V_0 and calculate the current on the electrode (boundary 1).

After the fluid flow is known, the z-component of the total force on the particle is calculated from Eq. 2.9:

$$F_{EK} = \oint_A n \cdot T \cdot e_z da \tag{2.9}$$

where e_z is the unit vector in the z direction.

2.3 Methods

2.3.0 Simulation of electric field and fluid flow

Finite element method (FEM) calculations were performed using Comsol Multiphysics V4.2 to mesh the system depicted in Fig. 2.1 and solve the equations presented in Table 2.1. The fixed computational parameters are presented are presented in Table 2.2. These values correspond roughly to the particles and tin-doped indium oxide (ITO) electrodes in 0.15 mM KOH electrolyte used in previous ETIRM experiments.[3,19] The values of the dimensionless parameters governing the system were varied by changing the exchange current density and the applied voltage V_0.

Table 2.2. Dimensional parameters used for FEM calculations.

Parameter	Value
Particle radius	a =5 μm
Solution conductivity	σ =30 μS/cm
Electrolyte viscosity	$\mu = 8.8\times10^{-4}$ Pa×s
Zeta potential of particle	ζ_p = -100 mV
Zeta potential of electrode	ζ_e =-100 mV
Electrolyte density	ρ = 1000 kg/m^3

The calculations were performed in a domain 200×200 μm^2, which was large enough to mitigate the effect of the finite domain size on the fluid flow immediately surrounding the particle. The domain was meshed with approximately 36,000 mesh points, over 60% of which were within 2a of the particle surface. The particle was bounded by 400 mesh elements, and the electrode by 150. Refining the mesh beyond this complexity did not change the results.

The accuracy of the calculation was validated by comparing the output to established theory for the uniform potential limit. The current normal to an electrode in contact with a dielectric sphere was computed and compared to the theory presented by Sides & Tobias[21], and the fluid flow around the particle was compared to the results presented by Keh & Lien[15]. The FEM results matched the published theory and data to within one percent.

2.3.1 Calculation of EO and EP forces

The electrokinetic forces on the particle were calculated from the integral presented in Eq. 2.9, along the particle surface. To confirm that the forces were correctly calculated, the force on a microparticle sedimenting through the center of an infinite vertical cylinder of finite radius, F_c, was calculated as a function of cylinder radius.[25] Comparing this result to output of the simulation again showed a difference of less than 1% between the theoretical and computational results.

F_{EP} and F_{EO} were calculated individually by setting the electrode zeta potential $\zeta_w = 0$ and the particle zeta potential $\zeta_p = 0$, respectively.

*2.3.2 Variation of J, δ,h**

The variable space explored in this work consists of J and δ values ranging from 0.01 to 10, and h*=h/a values ranging from 0.02 to 10. These values reflected the range of likely physical operating parameters in electrophoretic deposition or imaging amperometry experiments. With all other physical properties kept constant, changing V_0 changed δ; changing both i_o and V_o, while keeping δ constant, varied J. Variations of all of the physical parameters were tested, while keeping the dimensionless groups constant; it was concluded that the state of the system is uniquely defined by the set $\{J, \delta, h^*, \zeta_p, \zeta_w\}$.

Fitting was performed to establish the empirical relationship between the force on the particle, and the parameters J, δ and h*. The forces F_{EO} and F_{EP} were normalized as shown in Eq. 2.10 and mapped to the 3D parameter space (J,δ,h*).

$$F_{EO}^{*}(J,\delta,h^{*}) = \frac{F_{EO}}{6\pi\varepsilon a\zeta_{w}E_{\infty}} \tag{2.10(a)}$$

$$F_{EP}^{*}(J,\delta,h^{*}) = \frac{F_{EP}}{6\pi\varepsilon a\zeta_{p}E_{\infty}} \tag{2.10(b)}$$

This scaling nondimensionalizes the forces on the particle, while accounting for the fact that F_{EO}^{*} originates from flow on the electrode, while F_{EP}^{*} originates from flow on the particle. A more complete description of the fitting and the equations generated are included in the appendix.

2.3.3 Current distribution around tangent particle

Minor adjustments were made to the methods presented above to calculate the current density around a particle tangent to the electrode surface. The simulated particle was 10 μm in diameter, and particle-wall contact was approximated by h=500 pm, giving $h^{*}=5\times10^{-5}$. Smaller h values did not substantially change the calculated current distributions, but did increase the computational time prohibitively. Electrokinetic fluid flow was not calculated, which simplified the problem and allowed for much finer meshing in the region of interest underneath the particle. In these calculations, the domain was meshed with ~350,000 mesh units, 90% of which were within 2r of the particle surface. Aside from this, the parameter scaling was performed in an identical manner to the methods described for the electrokinetic fluid flow and force calculations.

2.4 Results & Discussion

2.4.0 Limiting Cases

We illustrate the principal finding of this work by showing the total electrokinetic force on a particle for varying electrode reactivity at a constant current level, calculated with FEM and plotted with Eqs. 2.1 and 2.2 is shown in Fig. 2.3. The two limiting cases, the primary and uniform current distributions, were simulated by setting the boundary condition at the electrode to uniform potential and uniform current density, respectively, while all of the other simulations were performed with the Butler-Volmer relation at the boundary, as defined in Table 2.1. Agreement between the force calculated with FEM and Eqs. 2.1 and 2.2 is very good in both of the limiting cases. The difference between the force calculated for larger h* using Eq. 2.2 and from the simulation is expected, because Eq. 2.2 was derived for asymptotically small values of h*. This expression vanishes at large particle-wall separations, while the true value of $F^*_{EP} + F^*_{EO}$ approaches 1 at large values of h*; one therefore expects the simulated values to exceed Yariv's predictions as the separation between the particle and the wall increases. The simulations accurately reflected this difference.

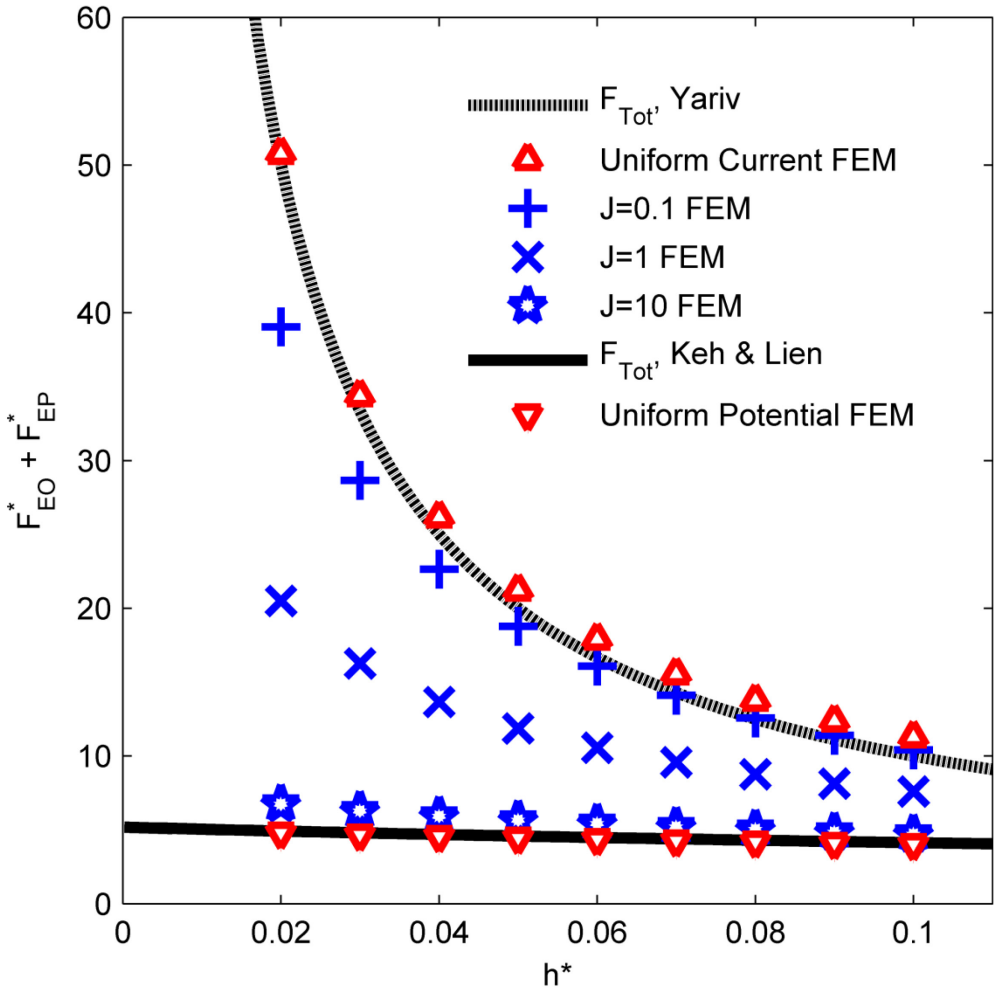

Fig. 2.3. The total force on the particle in the z-direction, normalized by $F_{bulk} = 6\pi\varepsilon a\zeta E_\infty$, where $\zeta = \zeta_p = \zeta_w$. The dotted and solid lines indicate analytical solutions in the limit of uniform current density and uniform potential on the electrode, respectively. The upwards and downwards triangles indicate FEM results in these same limits. The other points indicate FEM results for different values of J, at a fixed δ=0.0066.

This plot clearly demonstrates that the primary current distribution and the uniform current distribution are associated with the minimum and the maximum in the force on the particle, respectively, and that varying the parameter J at a constant value (for example, in Fig. 2.3 δ=0.0066) adjusts the force between these two limiting cases. Fixing J and varying δ yields a qualitatively similar trend of decreasing force with increasing δ. This decrease in total electrokinetic

force is due to a decrease in both F^*_{EP} and F^*_{EO}, because the strength of the tangential electric fields near the particle and the electrode are both minimized in the case of uniform potential on the electrode surface. As expected, the force on the particle given a uniform current distribution on the electrode is greater than given a uniform potential distribution. In this case, the total force varies between the two current distributions by about a factor of 6.

Two notable properties at the particle surface are plotted in Fig. 2.4: the force in the z-direction and the potential relative to the potential at the top of the particle. The abscissa on these plots is the angle at the particle center $\angle$, where $\angle = 0$ indicates the bottom of the particle (closest to the electrode) and $\angle = \pi$ the top. These results were calculated for $\zeta_p = \zeta_w = -100\text{mV}$, $h^* = 0.04$, and $E_\infty = 33\ \text{V/m}$, which are typical values for the polystyrene particles and ITO electrodes used in ETIRM experiments.[3,22] The force plotted is the stress multiplied by differential area $2\pi a^2 \sin\angle$, which is why the force goes to zero at $\angle = 0$, even though the stress at that location is at a maximum due to the rapidly increasing pressure differential approaching the bottom of the particle.

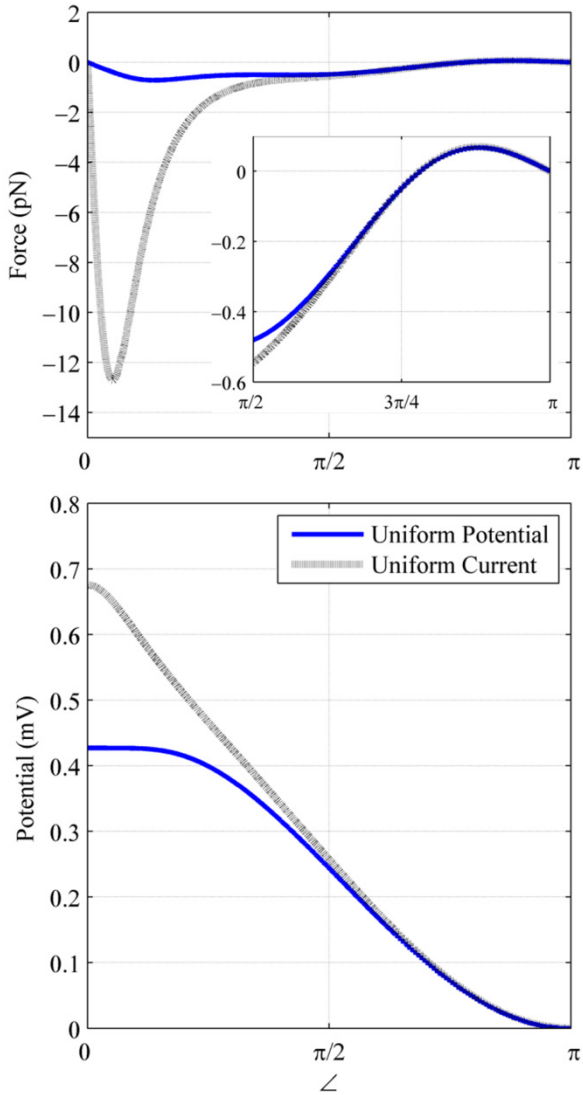

Fig. 2.4. Force and potential are plotted for h* = 0.04. (a) Force on the particle in the z-direction is plotted against the angle coordinate, where ∠=0 indicates the bottom of the particle and ∠=π indicates the top. The force here is calculated by multiplying the stress at a given ∠ and multiplying by the differential wedge area $2\pi a^2 \sin(\angle)$. The solid line indicates the case of uniform potential on the electrode and the dashed line indicates the case of uniform current. The force on the top half of the particle is magnified in the inset, to clearly show the convergence and sign change. (b) The potential on the particle surface as a function of angle, relative to the potential at the top of the particle. With this frame of reference, convergence between the two curves is again observed for angles greater than π/2.

Most of the force in Fig. 2.4 acts on the bottom half of the particle—both the force on the particle and the potential converge around $\angle = \pi/2$, moving towards the top of the particle. Note also that the force actually reverses at the top of the particle, as seen in the inset. This is an effect of the reduced pressure around the top of the particle—the electroosmotic flow along the particle is away from the electrode at every point on the particle surface and therefore viscous forces can only act in the –z direction in this case.

The fluid streamlines around a 10 μm particle given a uniform current appear in Fig. 2.5, which highlights the existence of two separate closed streamlines in the vicinity of the particle. This pattern follows from the fact that the electroosmotic flow along both the particle and the electrode is away from the origin, and therefore the superposition of these flows necessarily results in separate closed streamlines corresponding to the flow originating at each surface. This flow profile can have a profound impact on the aggregation behavior of particles above the electrode. The streamlines of Fig. 2.5 do not correspond to equally spaced values of the stream function, and in most cases the magnitude of the flow in the small toroid corresponding to electrode EO is significantly less than the flow in the toroid resulting from EO generated at the particle.

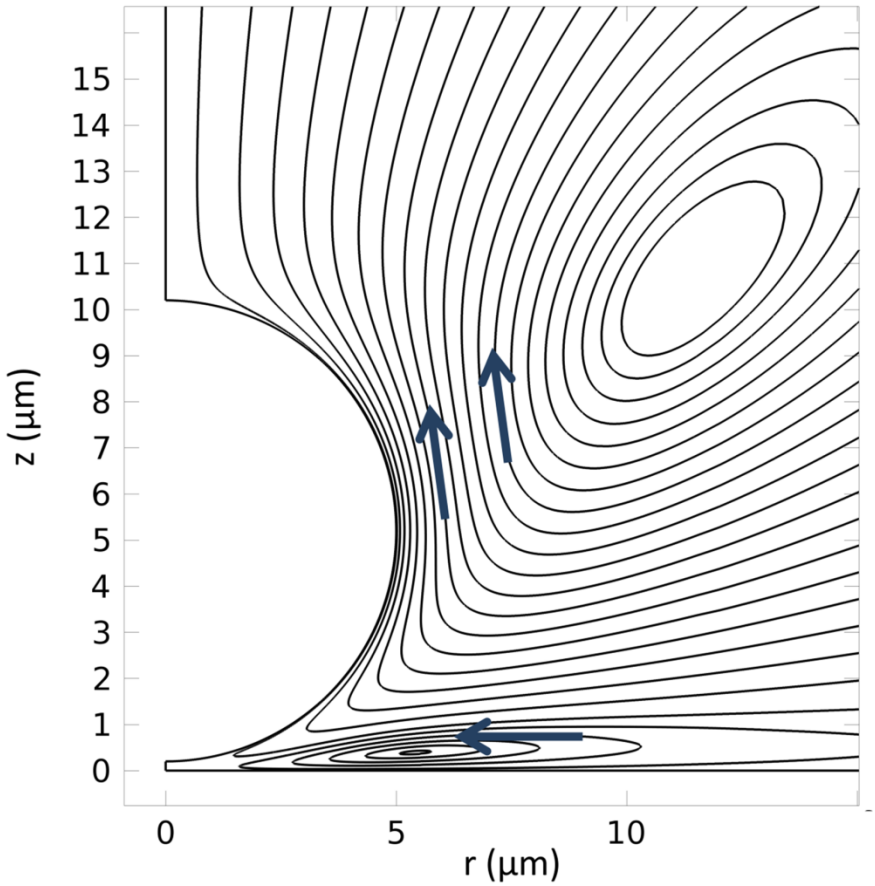

Fig. 2.5. Fluid flow streamlines calculated around a 10 μm particle given a uniform current density on the electrode under the particle, with h*=0.04, $\zeta_p = \zeta_w$, and $E_\infty = 33$ V/m. This plot illustrates the two separate circulation cells that exist given electroosmotic flow originating from the particle and the electrode. Streamline spacing is *not* indicative of fluid velocity.

2.4.1 Dependence of EO and EP forces on parameters

The linearity of the flow equations in these calculations allowed decoupling of the flow originating from the double layer of the particle from the flow originating from the double layer of the electrode. This decoupling allowed the exploration of the impacts various system parameters on the resulting forces, individually. First, we consider the relative strengths of the EP and EO forces on the particle and the limiting behavior described by Yariv for uniform current

density. Yariv assumed an asymptotically small particle-wall separation, that is, $h^* \to 0$. As stated in the theory presented here, in this limit, $F^*_{EO} = F^*_{EP}$, due to the dominance of pressure over viscous forces in this limit and the divergence of the electric field at $r = z = 0$. As the particle moves away from the wall, F^*_{EO} decreases more rapidly than F^*_{EP}, because the particle is moving away from the electrode, the source of the F^*_{EO} entrainment force. To test the validity of the assumptions made in that work, we display the ratio F^*_{EP}/F^*_{EO} as a function of h^* representing common values for electrostatically levitated particles in Fig. 2.6, demonstrating the rapid decrease of F^*_{EO} as the particle moves away from the electrode surface. Extrapolating this plot to $h^* = 0$ gives $F^*_{EP}/ F^*_{EO} = 1.05$, very close to the value of 1 predicted by Yariv. Given a typical particle-wall gap of 4% of the particle's radius, the difference between F^*_{EO} and F^*_{EP} is over 50%. This indicates that for particles levitated above the surface, using theory with the assumption of very small h* overestimates the strength of electroosmotic flow along the electrode surface due to the rapid decay in F^*_{EO} with separation between the particle and electrode.

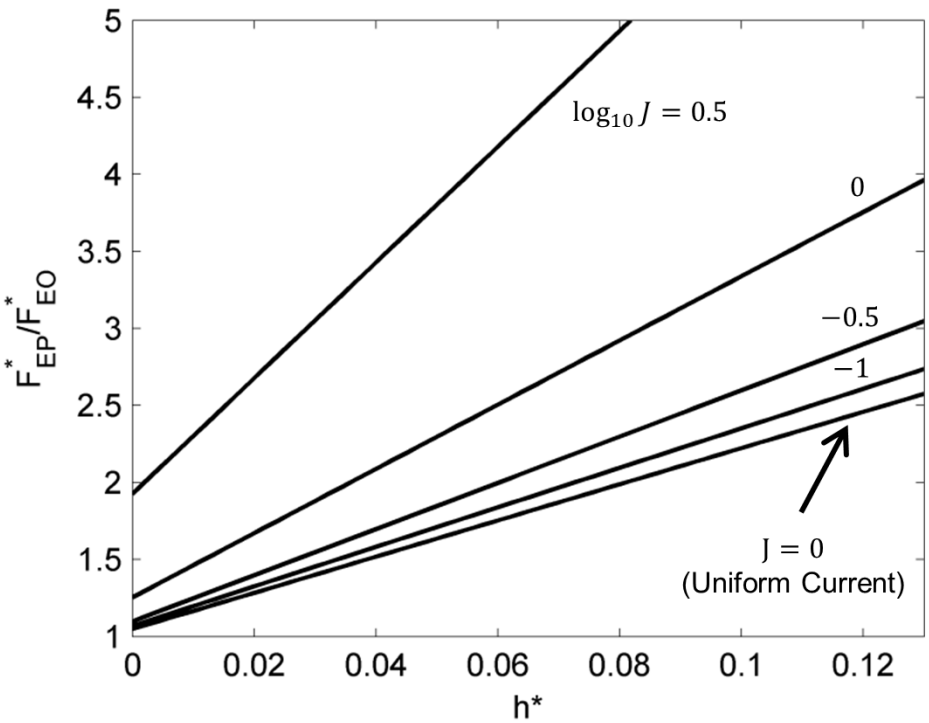

Fig. 2.6. The ratio of F_{EP} to F_{EO} as a function of particle-wall separation, in the uniform current distribution limit and for four values of J, with δ=0.01. The increase with increasing h* is due to the diminishing impact of the electroosmotic flow originating at the electrode as the particle-electrode separation increases.

The simulations also allowed systematic variation of J, δ and h^*. As seen in Fig. 2.3, the total force on the particle decays monotonically in a roughly exponential manner with increasing h^*. Fig. 2.7 shows the dependence of F^*_{EP} and F^*_{EO} on J and δ at a fixed particle-wall separation of $h^* = 0.02$. These plots show the expected trends: In the limit of small J and small δ, for which the current density is uniform, the force is maximal. When either J or δ is large, the force approaches a minimum described by Eq. 2.1, for the case of uniform potential on the electrode surface where $F^*_{EP} = C(h)$ and $F^*_{EO} = 0$. Surfaces such as these were calculated for heights between $h^* = 0.02$ and $h^* = 0.1$, and the forces

decayed monotonically as a function of height for every value of J and δ. The full set of data from these calculations is available in the supplementary materials.

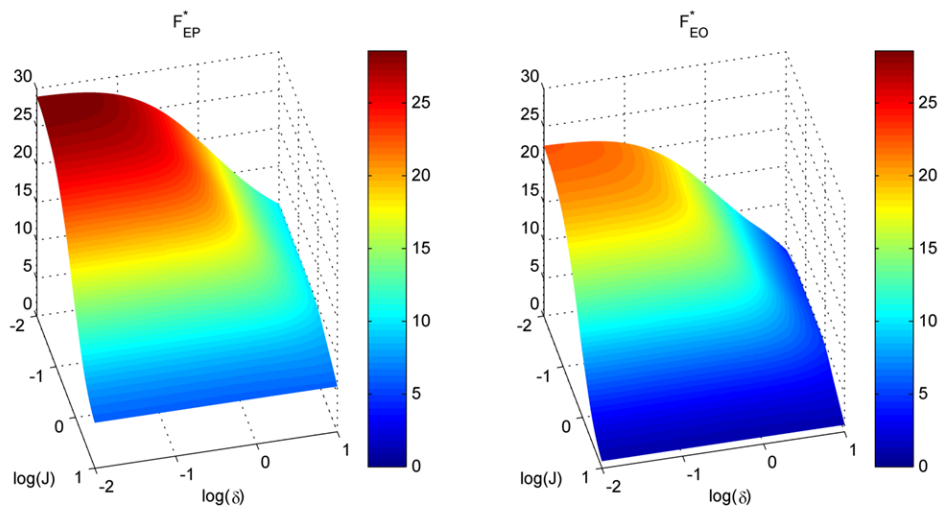

Fig. 2.7. F_{EP} and F_{EO} as a function of J and δ, for h*=0.02. As seen in Fig. 2.6, $F_{EP}^* > F_{EO}^*$ for $h^* > 0$, and that is seen here for all J and δ. As J becomes large, F_{EP}^* approaches C(h), which is 4.92 for h*=0.02. In that limit, F_{EO}^* approaches 0, as seen here.

Fig. 2.7 shows that the forces on the particles are 20 to 30 times the corresponding bulk electrophoretic force. It is also possible using these results to determine where on the J-δ variable space it is appropriate to refer to the analytical solutions derived in the uniform potential and uniform current density kinetic limits. In Fig. 2.8, contours are plotted against J and δ for $\mathrm{F_{Tot}} = \mathrm{F_{EO}^*} + \mathrm{F_{EP}^*} = \mathrm{F_{Yariv}}(1 \pm 0.05)$, where $\mathrm{F_{Yariv}}$ is the force calculated from Eq. 2.2 for $\zeta_\mathrm{p} = \zeta_\mathrm{w} = -100$ mV and $\mathrm{h}^* = 0.06$. At first glance, the lower left boundary on the use of this approximation in this plot seems counterintuitive, since $\mathrm{F_{Yariv}}$ was derived in the limit of uniform current distribution, which occurs in the limit J=δ=0. Without the assumption of $\mathrm{h}^* \to 0$ in the derivation of Eq. 2.2, only one

boundary would be present, at $F_{Tot} = 0.95F_{Yariv}$, and the force would asymptotically approach F_{Yariv} heading towards J=δ=0. As seen in Fig. 2.3, Eq. 2.2 underestimates the actual force in the uniform current limit, for all $h^* > 0$, with increasing deviations as the particle-wall separation increases. This means that instead of approaching F_{Yariv} asymptotically as moving towards J=δ=0, the total force actually crosses through F_{Yariv} as the current approaches uniformity on the electrode surface. As a result of this, at moderate values of h*, F_{Yariv} is accurate only for a narrow range of J and δ, as pictured here. A similar contour can be plotted to illustrate the accuracy of Eq. 2.1 for the uniform potential limit, but does not appear on this plot because it is beyond the extent of the parameter space shown here, representing likely physical parameters. The best agreement here between F_{Tot} and the force determined by Eq. 2.1, F_{KL}, occurs at J=δ=10, where $F_{Tot} = 1.23F_{KL}$.

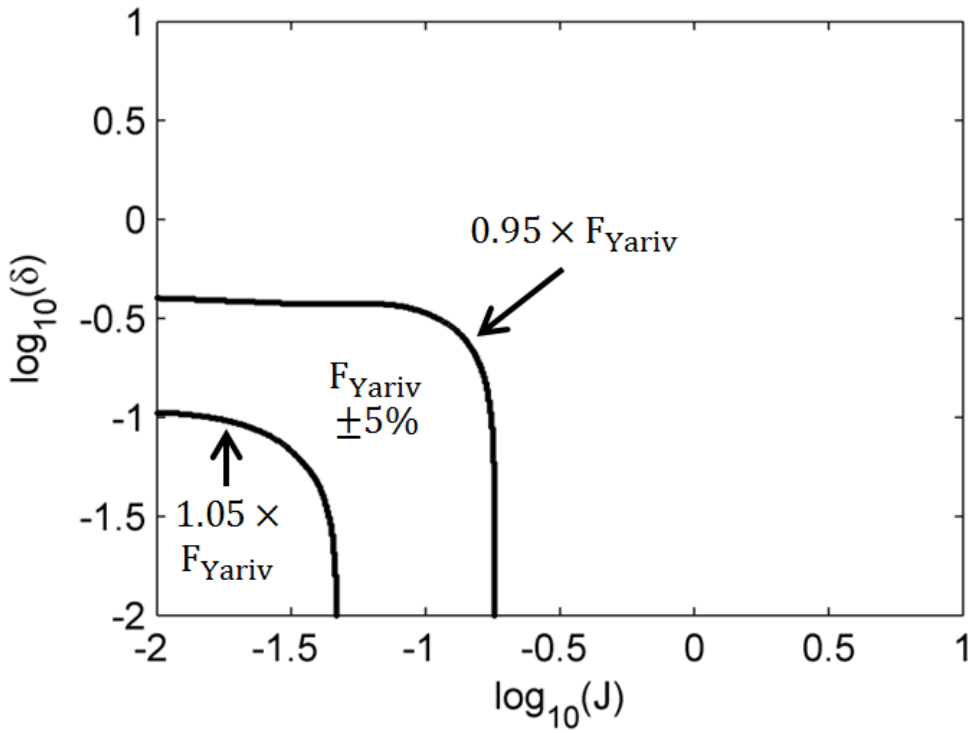

Fig. 2.8. Two contours of the total force on the particle, where $F_{Tot} = 0.95F_{Yariv}$ and $F_{Tot} = 1.05F_{Yariv}$, plotted for $\zeta_p = \zeta_w = -100$ mV and $h^* = 0.06$. The intervening space represents a region of J and δ where Eq. 2.2 is accurate to within 5% of the actual force on the particle.

2.4.2 Current distribution under a particle tangent to the electrode

The finite element method approach demonstrated here was also used to examine the current distribution itself under a particle tangent to the electrode surface. Since the particle is assumed to be a perfect dielectric, this system is mathematically identical to the electrode-bubble system explored by Sides and Tobias[21] for the uniform potential case. This computational method allows for exploration of the intermediate parameter space between the primary and uniform current density distributions, to illustrate how the current density distribution changes with changing electrode reaction kinetics. As with the force calculations, the current distribution was determined for varying values of J and δ. The current

distribution on the electrode for a constant value of J=0.01 and varying values of dimensionless current density δ is shown in Fig. 2.9. As expected, the current distribution becomes increasingly uniform with decreasing values of δ, as the resistance to current flow at the electrode increases with respect to the ohmic resistance to current flow in the electrolyte. In the limit of large values of δ, the potential distribution approaches uniformity, and the current density on the electrode drops below $i/i_{ave} = 0.01$ at a radial distance of $r/a \approx 0.3$, as reported in previous work.[21] The current density also goes through a shallow maximum around r/a=2 for all cases aside from the uniform current density case. The system represented here is axisymmetric, which means that the derivative of current density with respect to r/a must be zero at r/a=0, although this does not appear to be the case upon initial examination of the data shown in this figure.

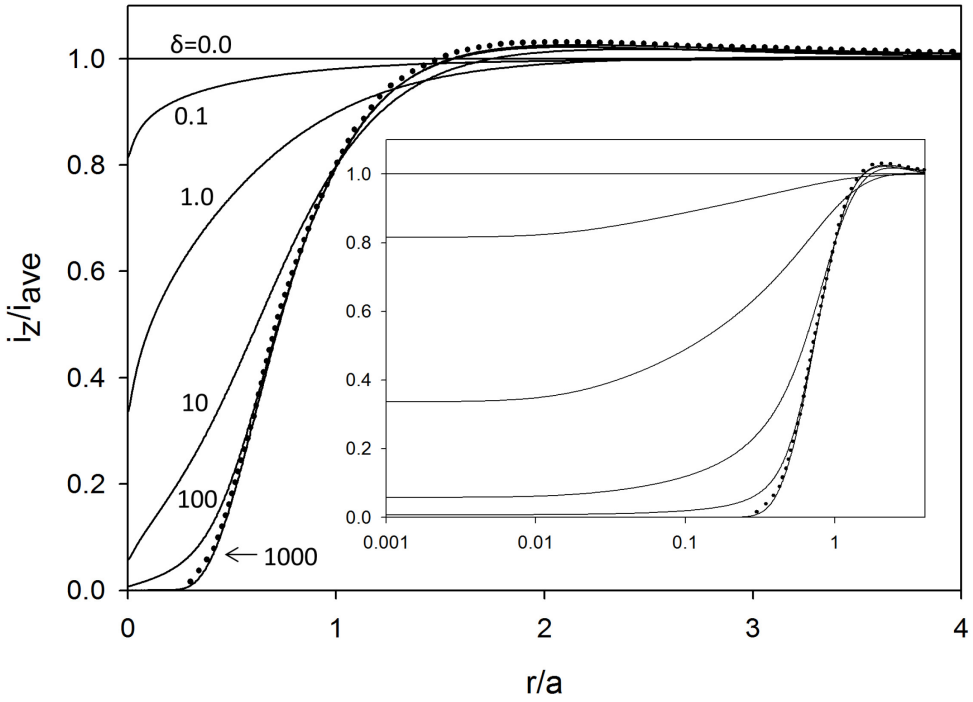

Fig. 2.9. Current density normal to the an electrode tangent a dielectric colloidal sphere, as a function of the radial distance away from the point of contact, normalized by the current density far from the particle. The inset shows the same data on a linear/log scale, to illustrate the behavior of the system at small values of r/a. The dotted line indicates data calculated assuming a uniform potential on the electrode surface.

The current density distribution with a constant δ=0.01 and varying values of J was also explored, as shown in Fig. 2.10. This shows clearly the transition between the uniform potential and uniform current density cases, given constant electric field strength far from the particle. Similar trends are observed here as are shown in Fig. 2.9, with deviations between the two figures due to the slightly greater impact of J on the current distribution as compared to δ when examining the intermediate cases between uniform current density and uniform potential on the electrode.

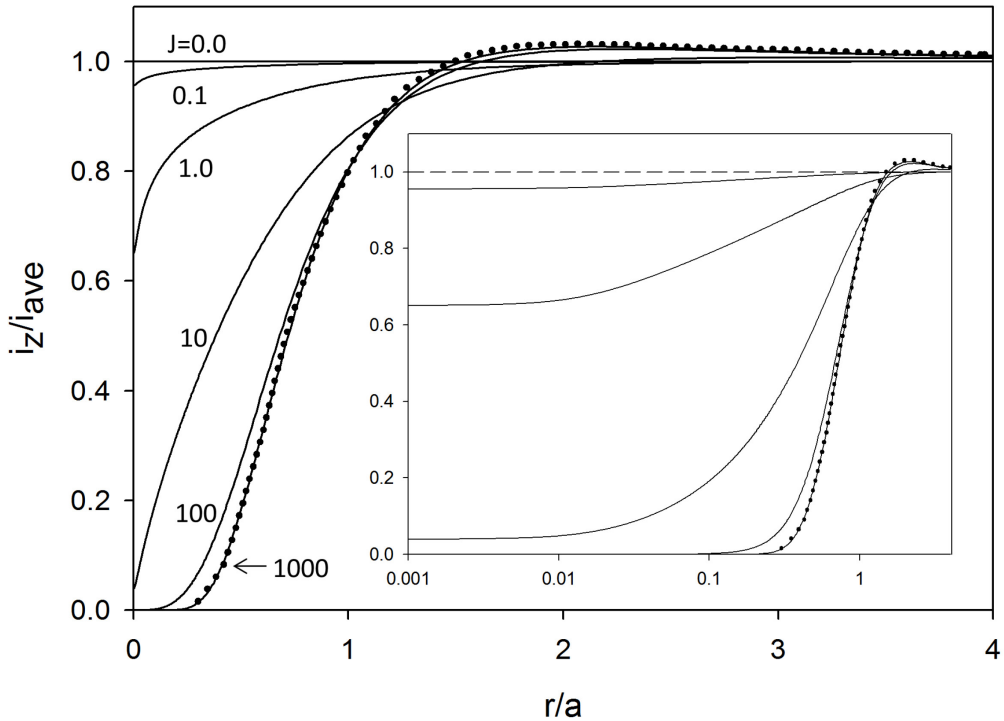

Fig. 2.10. Current density normal to the an electrode tangent a dielectric colloidal sphere, as a function of the radial distance away from the point of contact, normalized by the current density far from the particle. The inset shows the same data on a linear/log scale, to illustrate the behavior of the system at small values of r/a. The dotted line indicates data calculated assuming a uniform potential on the electrode surface.

To observe the effects of both J and δ on the nonuniformity of the current distribution, the current density at r=0 is plotted as a function of δ for varying values of J in Fig. 2.11. This is analogous to the analysis done by John Newman for a circular disk electrode.[20] Regardless of the value of J, the current density at r=0 approaches zero with increasing values of δ, indicating that the system is moving away from the uniform current density condition and towards the primary current distribution, where $i|_{r=0} = 0$ in this particle-wall geometry. This plot also demonstrates plainly that to obtain the uniform current density distribution, both δ and J must be at a minimum. With increasing values of J, the current at r=0 drops off rapidly. It is important to note that for these computations, r=0 is

allowable since h/a = 5×10^{-5} to facilitate solving of the finite element system. Given a particle truly tangent to the electrode surface, these data can be taken to be the current density infinitesimally far away from the point of contact between the particle and the wall.

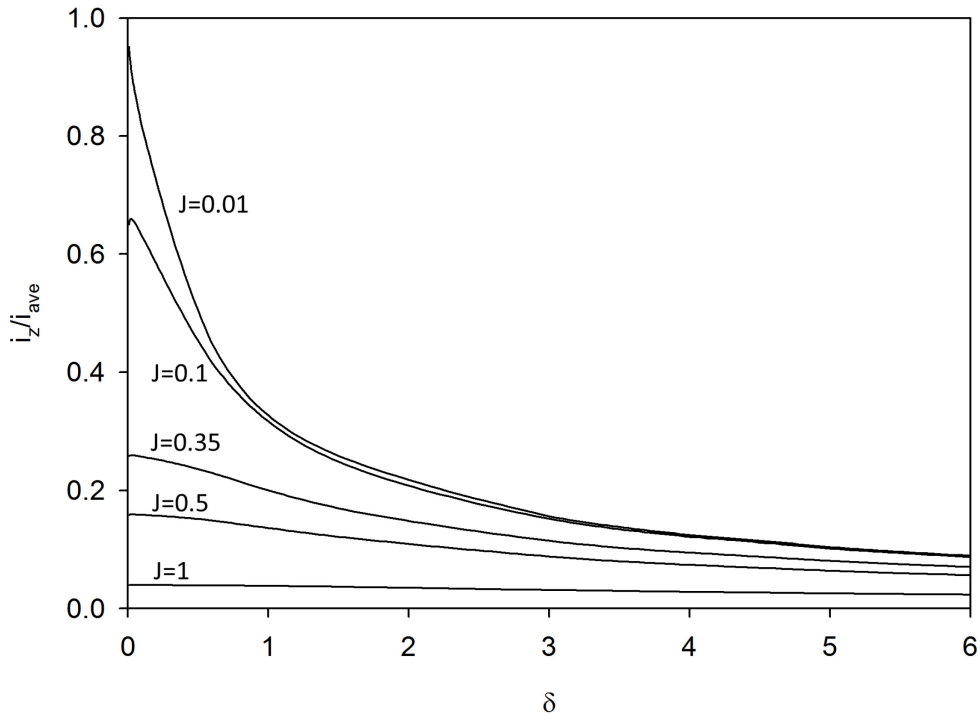

Fig. 2.11. Current density $i_z/i_{ave}|_{r=0}$ infinitesimally far away from the point of contact between an electrode surface and a tangent particle, normalized by the current density far from the particle. Current densities are plotted at constant values of dimensionless exchange current density J, for varying values of dimensionless current density δ. A uniform current distribution is obtained only for small J and small δ, where $i_z/i_{ave}|_{r=0}$ approaches unity. Given large J or large δ, the system approaches the primary current distribution.

2.5 Conclusions

The electrokinetic forces on an insulating colloidal particle electrostatically levitated over an electrode surface have been computationally explored here using finite element analysis, to determine the impact of the current

distribution around the particle on these forces. This current distribution is determined by the relationship between the kinetic resistance to electric current at the electrode and the ohmic resistance to electric current in the electrolyte. Theory exists for determining the force on a particle in either of two limiting cases of the current distribution—either the current distribution on the electrode under the particle is uniform or the potential is.[9,13,15] The theory developed to establish the electrokinetic force on the particle in these two limiting cases was verified here, and the analysis was extended to explore the variable space between these cases, using previously defined dimensionless kinetic parameters J and δ. The electrophoretic force originating from the particle was isolated from the fluid entrainment force from electroosmotic flow originating from the electrode surface, and the former was found to be greater than the latter by at least 50% for typical particle-wall separations. Use of these data will be a key part of future work that relies on accurate determination of the electrokinetic force on the particle as a function of electric field strength and physical characteristics of the particle-wall system, such as in the implementation of the colloidal imaging ammeter.

2.6 Acknowledgement

The work presented here was supported by The National Science Foundation under CBET grant 1133082.

2.7 Appendix.

2.7.0 Description of Fitting

Fitting was performed to establish an empirical relationship between the force on the particle, and the parameters J, δ and h*. Multiple parameter fitting was performed in Matlab. At a fixed h*, 1D cross sections of the F_{EO} data for constant J were fit to a complementary error function, with three arbitrary fitting parameters, giving an expression for the force across each 1D cross section $(J = J_0, \delta, h^* = h_0^*)$.

$$F_{EO}^*(J, \delta, h^* = h_0^*) = A_1(J) \times \operatorname{erfc}\left(\frac{\log_{10}\delta - A_2(J)}{A_3(J)}\right)$$

where A_n are initially fit as constants. To fit a 2D cross section of J and δ at a constant h^*, A_n are fit to separate, arbitrary functions to determine their dependence on J.

$$A_1 = B_1 \times \operatorname{erfc}\left(\frac{\log_{10} J - B_2}{B_3}\right)$$

$$A_2 = C_1 \times \{\exp(\log_{10} J - C_2) + C_3\}$$

$$A_3 = D_1 \times \operatorname{erfc}\left(\frac{\log_{10} J - D_2}{D_3}\right)$$

These expressions represent the force on the particle at a single value of h*. To express the height dependence of the force, an exponential prefactor is added to the equation with several more fitting parameters.

$$F_{EO}^*(J, \delta, h^*) = F_{EO}^*(J, \delta, h^* = h_0^*) \times \frac{E_1(J)}{\left(h^* - E_2(J)\right)^{1.3}}$$

$$E_1 = F_1 \times \operatorname{erfc}\left(\frac{\log_{10} J - F_2}{F_3}\right) + F_4$$

$$E_2 = G_1 \times \operatorname{erfc}\left(\frac{\log_{10} J - G_2}{G_3}\right) + G_4$$

The $h^{-1.3}$ dependence of the force is arbitrary, and was found to fit the data well for F^*_{EO} and F^*_{EP} for h*<1. F^*_{EP} was fit in a very similar manner, with one notable difference. The initial 1-D fit for varying values of δ is modified to account for the fact that the minimum in the electrophoretic force in the limit of uniform potential on the electrode is $C(h)$, not zero. All of the other expressions remain the same.

$$F^*_{EP}(J, \delta, h^* = h^*_0) = A_1(J) \times \operatorname{erfc}\left(\frac{\log_{10} \delta - A_2(J)}{A_3(J)}\right) + C(h)$$

The full set of fitting parameters is shown in Table 2.3, and an example of the fit is shown in Fig. 2.12 for the force at $h^* = 0.02$ and varying values of δ and J. Seventeen fitting parameters were used to fit each set of 455 data points, occupying the variable space 0.01<J<10, 0.01<δ<10, and 0.02<h*<0.1. Effectively fitting the data required a large number of parameters, given the highly non-linear nature of the force in this parameter space. The fit here is clearly quite good, but the true strength of this method is the ability to extrapolate to values of J, δ and h* beyond the parameter space explicitly explored in this study. Matlab code which can be used to calculate the force for any set of physical parameters using this fitted expression can be found in the appendix. Forces calculated using these parameters has an average $|F_{fitted}/F_{simulated}|$ of

4%, a maximum offset at any single point of 10%. The full set of data for F^*_{EP} and F^*_{EO}, as well as a Matlab script which uses these fitting parameters to determine the forces as a function of input parameters, can be found in the auxiliary materials.

Table 2.3. Fitting parameters.

Variable	F_{EO}	F_{EP}
B_1	2.634	2.847
B_2	-0.1053	-0.1052
B_3	0.9816	0.9883
C_1	0.02834	0.02749
C_2	-3.330	-3.309
C_3	7.806	8.026
D_1	1.376	0.6341
D_2	-2.728	0.4704
D_3	8.371	2.064
F_1	0.2203	0.7663
F_2	2.555	1.918
F_3	1.477	1.194
F_4	0.2398	0.8044
G_1	-0.04942	-0.7313
G_2	1.157	1.718
G_3	1.086	1.172
G_4	-0.05738	-0.7677

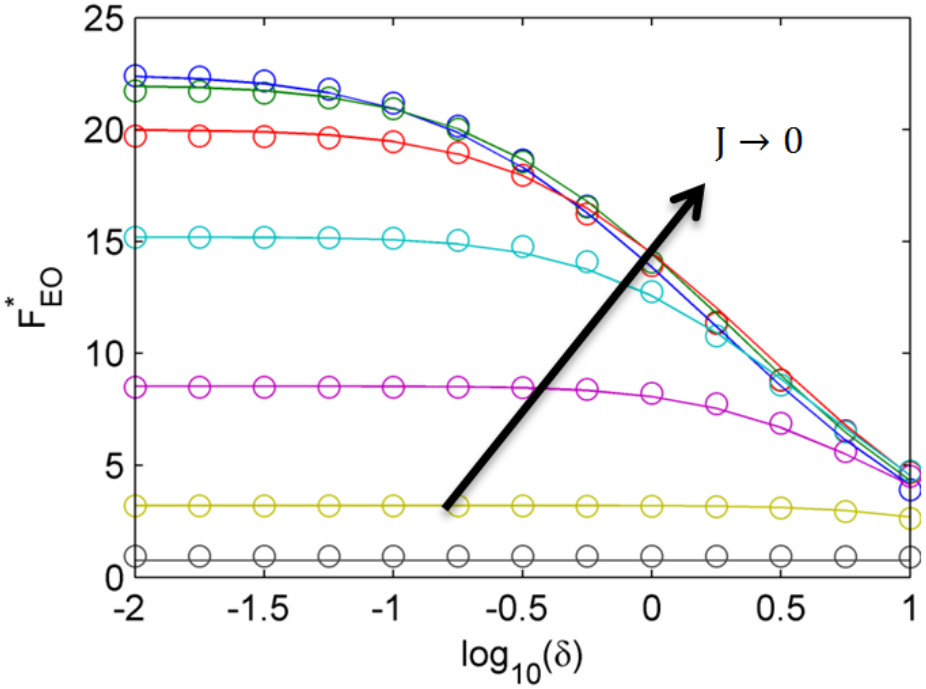

Fig. 2.12. An example of the fitting accuracy in F^*_{EO} for h*=0.02. Circles indicate results from FEM calculations, and curves indicate the fit resulting from the parameters given in Table 2.3. Each line indicates a different value of J, ranging from 10 to 0.01, decreasing along the arrow shown.

2.7.1 Instrumental MATLAB Code.

What follows is a MATLAB function written to return the normalized electrokinetic forces on a particle, using the fitting described in Appendix A.

```
function [F_EO_star, F_EP_star] = EK_Forces(J,delta,hStar)

%[F_EO_star, F_EP_star] = EK_Forces(J,delta,hStar)
%This takes the variables delta, J, h/a (hStar) and spits out
FEO_Star and
%FEP_star
% Constants format is [Letter]([FEO=1,FEP=2], Subscript), so that
it comes
% out as
% B=[FEO1 FEO2 FEO3
%    FEP1 FEP2 FEP3]
```

```
% clear; clc;

Ch = (1.554+hStar)./(0.3+hStar);

lJ = log10(J);
ld = log10(delta);

A = zeros(2,3);
B = [2.634, -0.1053, 0.9816; 2.847, -0.1052, 0.9883];
C = [0.02834, -3.33, 7.806; 0.02749, -3.309, 8.026];
D = [1.376, -2.728, 8.371; 0.6341, 0.4704, 2.064];
E = zeros(2);
F = [0.2203, 2.555, 1.477, 0.2398; 0.7663, 1.918, 1.194, 0.8044];
G = [-0.04942 1.157, 1.086, -0.05738; -0.7313, 1.718, 1.172, -
0.7677];

%Now we solve for the other parameters, E and A, with the same
format

E(:, 1) = F(:,1) .* erf ( (lJ-F(:,2))./F(:,3) ) + F(:,4);
E(:, 2) = G(:,1) .* erf ( (lJ-G(:,2))./G(:,3) ) + G(:,4);
A(:, 1) = B(:,1) .* erfc ( (lJ-B(:,2))./B(:,3) );
A(:, 2) = C(:,1) .* (exp ( lJ - C(:,2)) + C(:,3));
A(:, 3) = D(:,1) .* erfc ( (lJ-D(:,2))./D(:,3) );

F_EO_star = A(1,1) .* erfc ( (ld-A(1,2))/A(1,3) ) * E(1,1)
./((hStar-E(1,2)).^1.3);
F_EP_star = (A(2,1) .* erfc ( (ld-A(2,2))/A(2,3) ) + Ch ) *
E(2,1) ./((hStar-E(2,2)).^1.3);
```

2.7.2 Data Tables

What follows are tables of the raw simulation data for F_{EO}^{*} and F_{EP}^{*}, as defined by Eq. 2.10.

Table 2.4. F_{EO}^{*} as a function of h*, J and δ. Base of logs is $\log_{10}$.

Table 2.4(a). F_{EO}^{*}, h* = 0.02

	log J→						
log δ↓	-2	-1.5	-1	-0.5	0	0.5	1
-2	22.4171	21.73	19.7203	15.1904	8.5003	3.1847	0.9345
-1.75	22.3439	21.7039	19.7136	15.1895	8.5004	3.1846	0.9344
-1.5	22.1669	21.6275	19.6945	15.1867	8.5002	3.1846	0.9344
-1.25	21.8118	21.4182	19.6341	15.1768	8.4994	3.1846	0.9344
-1	21.1806	20.9363	19.4547	15.1473	8.4974	3.1844	0.9345
-0.75	20.1581	20.0244	18.98	15.0555	8.4905	3.1842	0.9344
-0.5	18.6354	18.5687	17.957	14.7882	8.4694	3.1836	0.9344
-0.25	16.5787	16.5465	16.2389	14.1104	8.4043	3.1814	0.9344
0	14.0891	14.0772	13.9358	12.7599	8.2163	3.1743	0.9342
0.25	11.4049	11.4044	11.3431	10.7812	7.7461	3.1528	0.9337
0.5	8.8225	8.8202	8.7973	8.5918	6.8843	3.0903	0.932
0.75	6.5516	6.532	6.5368	6.495	5.6168	2.9318	0.9268
1	3.9136	4.7065	4.694	4.754	4.51	2.6316	0.9118

Table 2.4(b). F_{EO}^{*}, h* = 0.04

	log J→						
log δ↓	-2	-1.5	-1	-0.5	0	0.5	1
-2	10.4545	10.1906	9.3797	7.531	4.6143	1.9961	0.6725
-1.75	10.4253	10.1802	9.3772	7.5307	4.6142	1.9961	0.6725
-1.5	10.3556	10.1489	9.369	7.5293	4.6141	1.9961	0.6725
-1.25	10.2137	10.0652	9.3439	7.525	4.6137	1.9961	0.6725
-1	9.96	9.8703	9.2697	7.5117	4.6126	1.9961	0.6725
-0.75	9.5443	9.4984	9.0726	7.4705	4.609	1.9959	0.6725
-0.5	8.9153	8.8953	8.6428	7.3504	4.5978	1.9955	0.6725
-0.25	8.045	8.0381	7.9086	7.0436	4.5634	1.994	0.6724
0	6.9524	6.9593	6.8977	6.4259	4.4637	1.9894	0.6723
0.25	5.7465	5.7508	5.7326	5.5032	4.2144	1.9752	0.6719
0.5	4.5366	4.5389	4.5309	4.4467	3.7569	1.9338	0.6705
0.75	3.4324	3.4308	3.4323	3.4173	3.0805	1.8294	0.6664

1	2.6152	2.5092	2.5021	2.5336	2.506	1.6333	0.6544

Table 2.4(c). F_{EO}^{*}, h* = 0.06

	log J→						
log δ↓	-2	-1.5	-1	-0.5	0	0.5	1
-2	6.5688	6.3031	5.9495	4.8684	3.1149	1.4337	0.5195
-1.75	6.5519	6.2973	5.9482	4.8682	3.1149	1.4337	0.5195
-1.5	6.5117	6.2798	5.9433	4.8672	3.1149	1.4336	0.5195
-1.25	6.43	6.2324	5.9286	4.8646	3.1146	1.4337	0.5195
-1	6.2835	6.1222	5.885	4.8565	3.114	1.4336	0.5195
-0.75	6.0416	5.9102	5.7689	4.8312	3.1114	1.4335	0.5195
-0.5	5.672	5.565	5.5144	4.7575	3.1039	1.4332	0.5195
-0.25	5.1543	5.0669	5.0752	4.5686	3.0809	1.4321	0.5195
0	4.4976	4.4283	4.4619	4.1858	3.0141	1.4286	0.5194
0.25	3.7497	3.6976	3.7357	3.6215	2.8465	1.4178	0.519
0.5	2.9873	2.9483	2.9838	2.9491	2.5394	1.3867	0.5179
0.75	2.2801	2.2507	2.2754	2.2836	2.0843	1.308	0.5144
1	1.5427	1.6527	1.6701	1.7117	1.7068	1.1546	0.5043

Table 2.4(d). F_{EO}^{*}, h* = 0.08

	log J→						
log δ↓	-2	-1.5	-1	-0.5	0	0.5	1
-2	4.6598	4.5555	4.2447	3.5142	2.3073	1.1124	0.4168
-1.75	4.6486	4.5517	4.2437	3.5141	2.3072	1.1124	0.4168
-1.5	4.6216	4.5397	4.2404	3.5136	2.3073	1.1123	0.4168
-1.25	4.5668	4.5068	4.2305	3.5117	2.3071	1.1124	0.4168
-1	4.4681	4.4307	4.2007	3.5059	2.3065	1.1123	0.4168
-0.75	4.3048	4.2843	4.1217	3.4884	2.3047	1.1122	0.4168
-0.5	4.0538	4.0437	3.9479	3.4368	2.2991	1.112	0.4168
-0.25	3.6992	3.6944	3.646	3.3043	2.282	1.111	0.4168
0	3.2441	3.242	3.2204	3.0346	2.2323	1.1082	0.4167
0.25	2.7192	2.719	2.7098	2.6346	2.1081	1.0995	0.4164
0.5	2.1766	2.1762	2.1752	2.1563	1.88	1.0743	0.4154
0.75	1.6673	1.6646	1.6637	1.6749	1.542	1.0109	0.4124
1	1.1501	1.2298	1.2227	1.2593	1.2688	0.8936	0.4037

Table 2.4(e). F^*_{EO}, h* = 0.10

	log J→						
log δ↓	-2	-1.5	-1	-0.5	0	0.5	1
-2	3.5371	3.4614	3.2346	2.6825	1.8028	0.8921	0.3426
-1.75	3.5288	3.4586	3.2337	2.6824	1.8028	0.8921	0.3426
-1.5	3.5091	3.4498	3.2314	2.6819	1.8027	0.8921	0.3426
-1.25	3.469	3.4258	3.224	2.6806	1.8026	0.8921	0.3426
-1	3.3969	3.3701	3.2022	2.6763	1.8021	0.8921	0.3426
-0.75	3.277	3.2624	3.1438	2.663	1.8007	0.892	0.3426
-0.5	3.0919	3.085	3.0151	2.6245	1.7964	0.8917	0.3426
-0.25	2.8289	2.8255	2.7905	2.5254	1.7828	0.891	0.3426
0	2.4886	2.4875	2.4716	2.323	1.7438	0.8886	0.3425
0.25	2.0925	2.0925	2.086	2.0133	1.6459	0.8813	0.3422
0.5	1.6789	1.6788	1.6768	1.6427	1.4667	0.8603	0.3414
0.75	1.2868	1.2856	1.285	1.2694	1.201	0.8075	0.3387
1	0.8801	0.9462	0.9434	0.9359	0.9922	0.7104	0.3311

Table 2.5. F^*_{EP} as a function of h*, J and δ. Base of logs is $\log_{10}$.

Table 2.5(a). F^*_{EP}, h* = 0.02

	log J→						
log δ↓	-2	-1.5	-1	-0.5	0	0.5	1
-2	28.8637	28.1339	26.0006	21.2017	14.1173	8.4477	5.9899
-1.75	28.7859	28.1074	25.9935	21.2009	14.1172	8.4476	5.99
-1.5	28.5982	28.025	25.9727	21.1971	14.1173	8.4476	5.99
-1.25	28.2202	27.8022	25.9083	21.1872	14.1162	8.4476	5.9899
-1	27.5488	27.2891	25.7174	21.155	14.1138	8.4475	5.9899
-0.75	26.4597	26.3177	25.2131	21.0572	14.1063	8.4473	5.99
-0.5	24.8394	24.768	24.1215	20.7704	14.0835	8.4463	5.9899
-0.25	22.6473	22.614	22.2885	20.0426	14.0116	8.4439	5.9899
0	19.9931	19.9783	19.8297	18.5947	13.8053	8.4356	5.9896
0.25	17.1285	17.1218	17.0583	16.4717	13.2883	8.4103	5.9888
0.5	14.3579	14.355	14.3287	14.0694	12.2961	8.3372	5.9864
0.75	11.9205	11.9195	11.9078	11.7974	10.9228	8.1528	5.9798
1	9.935	9.9348	9.93	9.883	9.4768	7.7916	5.9599

Table 2.5(b). F_{EP}^{*}, h* = 0.04

log δ↓ \ log J→	-2	-1.5	-1	-0.5	0	0.5	1
-2	15.9942	15.6985	14.8216	12.8131	9.6801	6.8734	5.4384
-1.75	15.9622	15.6872	14.8187	12.8124	9.6802	6.8734	5.4385
-1.5	15.8858	15.6537	14.8099	12.8111	9.68	6.8734	5.4384
-1.25	15.7306	15.5615	14.7825	12.8062	9.6794	6.8734	5.4387
-1	15.4531	15.3479	14.7012	12.7917	9.6783	6.8734	5.4384
-0.75	14.9985	14.941	14.4857	12.7466	9.6743	6.8731	5.4385
-0.5	14.3109	14.2827	14.0158	12.6147	9.6621	6.8726	5.4384
-0.25	13.361	13.3478	13.2141	12.2788	9.6234	6.8708	5.4382
0	12.1786	12.1727	12.1121	11.6036	9.5125	6.8654	5.4381
0.25	10.861	10.8584	10.8329	10.5968	9.2347	6.8487	5.4375
0.5	9.5428	9.5418	9.5315	9.4319	8.7011	6.8003	5.4356
0.75	8.3467	8.3462	8.3419	8.3007	7.9604	6.6784	5.4302
1	7.3432	7.3453	7.3417	7.3254	7.1777	6.4428	5.4146

Table 2.5(c). F_{EP}^{*}, h* = 0.06

log δ↓ \ log J→	-2	-1.5	-1	-0.5	0	0.5	1
-2	11.5804	11.4084	10.8946	9.7107	7.8192	6.0345	5.0491
-1.75	11.5616	11.4017	10.893	9.7104	7.8193	6.0346	5.0491
-1.5	11.5171	11.3818	10.8875	9.7091	7.8192	6.0345	5.0491
-1.25	11.4259	11.3276	10.8716	9.7064	7.8188	6.0348	5.0491
-1	11.2628	11.2019	10.823	9.6973	7.8181	6.0345	5.0491
-0.75	10.9941	10.961	10.6942	9.6695	7.8153	6.0344	5.049
-0.5	10.5849	10.568	10.412	9.5879	7.8068	6.0339	5.049
-0.25	10.0134	10.006	9.9278	9.3787	7.7813	6.0327	5.049
0	9.2917	9.2884	9.2534	8.9574	7.7063	6.0285	5.0488
0.25	8.4747	8.4733	8.4586	8.3234	7.5198	6.0159	5.0483
0.5	7.6437	7.6431	7.6372	7.5815	7.1615	5.9797	5.0467
0.75	6.8776	6.8771	6.875	6.8528	6.6647	5.8889	5.0422
1	6.2262	6.2279	6.2256	6.2166	6.1394	5.7138	5.0295

Table 2.5(d). F_{EP}^{*}, h* = 0.08

	log J→						
log δ↓	-2	-1.5	-1	-0.5	0	0.5	1
-2	9.3071	9.1912	8.8427	8.0383	6.7373	5.4737	4.7442
-1.75	9.2945	9.1867	8.8416	8.038	6.7373	5.4736	4.7443
-1.5	9.2641	9.1732	8.838	8.0374	6.7372	5.4736	4.7443
-1.25	9.2022	9.1362	8.827	8.0354	6.7371	5.4736	4.7443
-1	9.0914	9.0507	8.7936	8.029	6.7364	5.4737	4.7442
-0.75	8.9083	8.8861	8.7053	8.0094	6.7344	5.4734	4.7443
-0.5	8.6279	8.6169	8.5113	7.9521	6.7281	5.4732	4.7442
-0.25	8.2336	8.2288	8.176	7.805	6.7091	5.472	4.7442
0	7.7322	7.7301	7.7066	7.5078	6.6538	5.4687	4.7439
0.25	7.1589	7.158	7.1482	7.0586	6.516	5.4589	4.7435
0.5	6.5699	6.5694	6.5657	6.5295	6.2517	5.43	4.7423
0.75	6.0221	6.0221	6.0205	6.0062	5.8858	5.3584	4.7385
1	5.5531	5.5546	5.5528	5.5474	5.4996	5.2209	4.7276

Table 2.5(e). F_{EP}^{*}, h* = 0.10

	log J→						
log δ↓	-2	-1.5	-1	-0.5	0	0.5	1
-2	7.9054	7.8207	7.5643	6.9726	6.0098	5.0583	4.4937
-1.75	7.8961	7.8173	7.5634	6.9724	6.0098	5.0583	4.4937
-1.5	7.8738	7.8073	7.5606	6.9719	6.0097	5.0583	4.4936
-1.25	7.8283	7.7802	7.5524	6.9706	6.0094	5.0582	4.4936
-1	7.7467	7.7167	7.5277	6.9655	6.0089	5.0583	4.4937
-0.75	7.6112	7.5952	7.4622	6.9508	6.0075	5.0582	4.4937
-0.5	7.4036	7.3956	7.3182	6.9076	6.0026	5.0578	4.4936
-0.25	7.1107	7.107	7.0684	6.7968	5.9877	5.0569	4.4935
0	6.7355	6.734	6.7171	6.5724	5.9447	5.0541	4.4934
0.25	6.3044	6.3038	6.2968	6.2323	5.837	5.0461	4.493
0.5	5.8588	5.8585	5.8559	5.8303	5.6314	5.0225	4.4918
0.75	5.4424	5.4419	5.4413	5.4313	5.3473	4.9637	4.4886
1	5.0845	5.0856	5.0842	5.0806	5.0485	4.8521	4.4794

2.8 Works Cited

(1) Bohmer, M. *Langmuir* **1996**, *12*, 5747–5750.

(2) Guelcher, S. A.; Solomentsev, Y.; Anderson, J. L. *Powder Technology* **2000**, 90–97.

(3) Wirth, C. L.; Sides, P. J.; Prieve, D. C. *Journal of Colloid and Interface Science* **2011**, *357*, 1–12.

(4) Wirth, C. L.; Rock, R. M.; Sides, P. J.; Prieve, D. C. *Langmuir* **2011**, *27*, 9781–91.

(5) Gong, T.; Wu, D. T.; Marr, D. W. M. *Langmuir* **2003**, *19*, 5967–5970.

(6) Trau, M.; Saville, D. A.; Aksay, I. A. *Langmuir* **1997**, *13*, 6375–6381.

(7) Velev, O. D.; Kaler, E. W. *Langmuir* **1999**, *15*, 3693–3698.

(8) Juárez, J. J.; Feicht, S. E.; Bevan, M. a. *Soft Matter* **2012**, *8*, 94.

(9) Solomentsev, Y.; Bohmer, M.; Anderson, J. L. *Langmuir* **1997**, *13*, 6058–6068.

(10) Ma, F.; Wang, S.; Smith, L.; Wu, N. *Advanced Functional Materials* **2012**, n/a–n/a.

(11) Wu, H.-J.; Bevan, M. A. *Langmuir* **2005**, *21*, 1244–54.

(12) Gong, T.; Wu, D. T.; Marr, D. W. M. *Langmuir* **2002**, *18*, 10064–10067.

(13) Yariv, E. *Journal of Fluid Mechanics* **2010**, *645*, 187.

(14) Ristenpart, W. D.; Aksay, I. a; Saville, D. a *Langmuir* **2007**, *23*, 4071–80.

(15) Keh, H.-J.; Lien, L.-C. *J. Chin. Inst. Chem. Eng.* **1989**, *20*, 283–290.

(16) Ristenpart, W. D.; Aksay, I. a.; Saville, D. a. *Physical Review E* **2004**, *69*, 1–8.

(17) Solomentsev, Y.; Guelcher, S. A.; Bevan, M. A.; Anderson, J. L. *Langmuir* **2000**, *16*, 9208–9216.

(18) Newman, J.; Thomas-Alyea, K. E. *Electrochemical Systems*; 3rd ed.; John Wiley & Sons, Inc.: Hoboken, NJ, 2004.

(19) Rock, R. M.; Sides, P. J.; Prieve, D. C. Ensemble Average TIRM for Imaging Amperometry. *TBD* **2013**.

(20) Newman, J. *Journal of The Electrochemical Society* **1966**, *113*, 1235.

(21) Sides, P. J.; Tobias, C. W. *Journal of The Electrochemical Society* **1980**, *485*, 288–291.

(22) Fagan, J. A.; Sides, P. J.; Prieve, D. C. *Langmuir* **2002**, *18*, 7810–7820.

(23) Fagan, J. A.; Sides, P. J.; Prieve, D. C. *Langmuir* **2004**, *20*, 4823–34.

(24) Sides, P. J. *Langmuir* **2003**, *19*, 2745–2751.

(25) Happel, J.; Brenner, H. *Low Reynolds Number Hydrodynamics*; Publishers, M. N., Ed.; Martinus Nijhoff Publishers, 1983; Vol. 40.

Chapter 3

Ensemble Average TIRM for Imaging Amperometry

Reproduced in part from "Ensemble Average TIRM for Imaging Amperometry", Reza M. Rock, Paul J. Sides, Dennis C. Prieve, accepted for publication by the Journal of Colloid and Interface Science, 2013, DOI: 10.1016/j.jcis.2013.04.010

3.0 Abstract

Colloidal particles can function as probes of local electrochemical current density if a functional relationship between the response of the particles and the electric field in the vicinity of the particles can be established. The nanometer scale movement of a single colloidal particle during cyclic voltammetry can be observed with the aid of total internal reflection microscopy. The intensity of scattered light can be related back to the current density local to that particle, and hence the method is called imaging amperometry. Data acquisition and optical constraints, however, make a single-particle method impractical for analysis of macro-scale (~1cm^2) surfaces covered by several hundred thousand particles. Subdivision of the electrode into small patches, each containing an ensemble of particles, solves this problem if the scattering from the ensembles can be related to the local electric field. For example, a 100 × 100 array of square 100 μm patches each containing approximately two dozen particles would form a mosaic of electrochemical activity with 0.01% area resolution on a 1cm^2 electrode having location-dependent electrocatalytic properties. The focus of this contribution, therefore, is adaptation of the method from single particles to particle ensembles. The algebraic relationship between current density and scattering intensity for single particles holds for ensembles if the mean scattering intensity is corrected to

its mode. Currents calculated from particle light scattering at different locations on a single ITO/gold patterned electrode agree well with currents measured on these two electrode materials, which have quite different electrocatalytic properties.

3.1 Introduction

High throughput testing of electrocatalysts and corrosion resistant materials accelerates research. Some methods for rapid testing utilize electrodes made from composition spread alloy films (CSAFs) that exhibit continuously varying compositions.[1–5] A means for measuring the local current on these CSAF electrodes would enable researchers to map the electrochemical activity over the entire composition space of the sample in a single experiment. While such electrodes would enable rapid testing of many alloy compositions in parallel or rapid succession, local electrochemical measurements on films of varying composition are difficult because current density in a typical electrochemical cell is the quotient of the total current and the entire electrode area.

Investigators nevertheless have attempted to exploit the high-throughput concept.[6] The scanning drop cell (SDC) is a serial method for surface characterization. Using this method, one measures local current on an inhomogeneous surface by rastering a small drop of electrolyte at the tip of an electrode across the surface, stopping to take data at different locations on the sample.[1,2,7,8] The resolution of this method scales with the radius of the droplet, generally between 50 and 500 μm, although smaller sizes have been reported.[9] The SDC method offers good resolution, at the cost of increased longer experiments because data are acquired serially; collecting data over a large composition space takes time. Surface plasmon resonance (SPR) or specific fluorescent tags, among other imaging techniques, indicate local electrochemical reactions on the electrode.[3,10–12] These methods allow parallel testing over a large

composition space but have drawbacks. SPR requires that the electrode consist of noble metals, such as gold, while lateral diffusion of fluorescent tags degrades resolution. Electrode arrays, coated with a CSAF or separately prepared electrocatalyst samples,[13–16] allow accurate electrochemical measurements but limit the composition space of experimentation to the number of electrodes available. A method combining flexibility, speed, and resolution has yet to appear.

We have proposed using colloidal particles as probes of local current density. [17,18] Based on observing the electrophoretic motion of colloidal particles in the vicinity of a working electrode (WE), the method is advantageous for electrochemical sensing because the particles are passive probes; they do not rely on chemical interactions with the products or reactants of the electrochemistry. We established that the motion of a single particle above tin-doped indium oxide (ITO) and gold surfaces can be monitored using total internal reflection microscopy (TIRM) and used to infer the electrochemical current density local to that particle with no adjustable parameters. The particle scattered light from an evanescent wave adjacent to the electrode surface. The scattered light was measured by means of a photomultiplier tube (PMT) and was used to deduce the instantaneous separation between the particle and the wall during a cyclic voltammetry (CV) experiment.

Gathering scattering intensity from a single particle proved the concept, but the overall goal is to image the motion of hundreds of thousands of “probes” distributed across an entire electrode simultaneously. Furthermore, the method

should have sufficient local resolution to distinguish the electrochemical reactivity of one site from another. Since implementation of this method for characterization of large-scale (~1cm^2) CSAF surfaces involves levitating colloidal particles over the entire surface to give a surface coverage of 5-10%, simultaneous measurements must be taken across the entire surface by means of a CCD camera instead of the PMT. For example, Bevan and co-workers perform TIRM experiments with ensembles of particles using video microscopy and tracking the location and scattering intensity of each individual particle.[19–21] Ideally, an analogous approach could be applied to the current problem. The particles could then be treated as individual experiments and the data from each particle would be analyzed using the theory developed in a previous publication on the topic.[17] The success of this method, however, requires tracking several hundred thousand individual particles during an entire experiment and resolving the scattered light from each particle, which is not practical.

We propose a grid of patches, squares approximately 100 μm to a side and containing 20-40 particles each. Average scattering intensities are measured over each of these patches during CV experiments and analyzed to create a map of electrocatalytic activity across the surface, with a resolution limited by the length scale of the patches. The contrast provided by the scattering from ensembles of particles is dramatic, which provides confidence that the method can be quite sensitive. Example images of a patch of particles scattering light during ETIRM experiments appear in Fig. 3.1. As positive current passes through the electrode, the particles are driven toward the electrode surface and the scattering is intense.

Conversely the particles are driven away by negative current and the field is black. In the presence of small capacitive currents, the particles scatter an intermediate amount of light from the evanescent wave, with fluctuations due to Brownian motion of the particles.

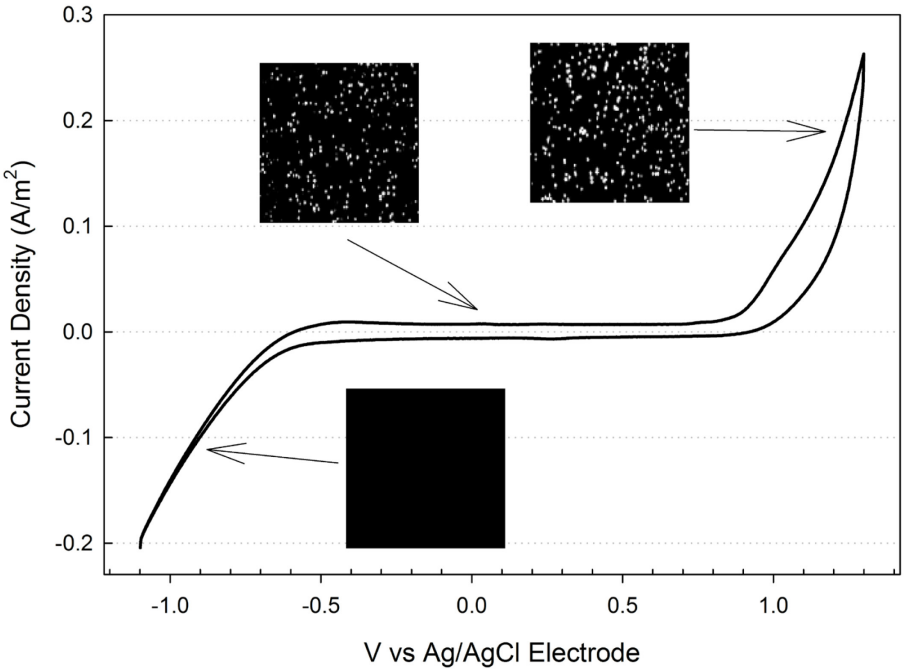

Fig. 3.1. Current density and light scattering from particles (inset images) in a typical Ensemble TIRM cyclic voltammetry experiment. Potentials are relative to an Ag/AgCl electrode in the same solution. Large potentials result in positive faradiac current passing through the electrode and a net downward electrokinetic force on the particles. Downward and upward motion of the particles is indicated by an increase and decrease in the scattering intensity, respectively.

In this contribution we show that the single particle theory can be adapted to ensembles, but some issues must be addressed. First, particles are polydisperse in size, zeta potential, and their scattering intensity in TIRM experiments.[20] In addition, taking average measurements removes the ability to construct full

potential energy diagrams for the particles. Thus the intensity corresponding to the mode height of the particle (which is the quantity used to deduce the local electric field in single-particle experiments) cannot be directly measured; instead, it must be inferred from the mean intensity using a theory for the expected distribution. These concerns have been addressed successfully; we demonstrate that the equation for scattering from a single particle can be used for particle ensembles if one corrects for the difference between the mean of the scattering intensity and the mode.

3.2 Theory

Here we present the theoretical basis for ensemble-average imaging amperometry. The description begins with theory for single particles and proceeds to ensembles. The single particle theory is reprised because recent work has shown that accuracy even for a single particle depends on details of the current distribution around each particle, which enhances the sensitivity of the method to electrode kinetics. After the new complete theory for a single particle and arbitrary values of electrode kinetic parameters is established, we treat the ensembles.

3.2.0 Theory for single particles with a uniform potential on the electrode

When illuminated by an evanescent wave, a particle scatters light whose intensity I(h) is very sensitive to the elevation h, as pictured in Fig. 3.2.

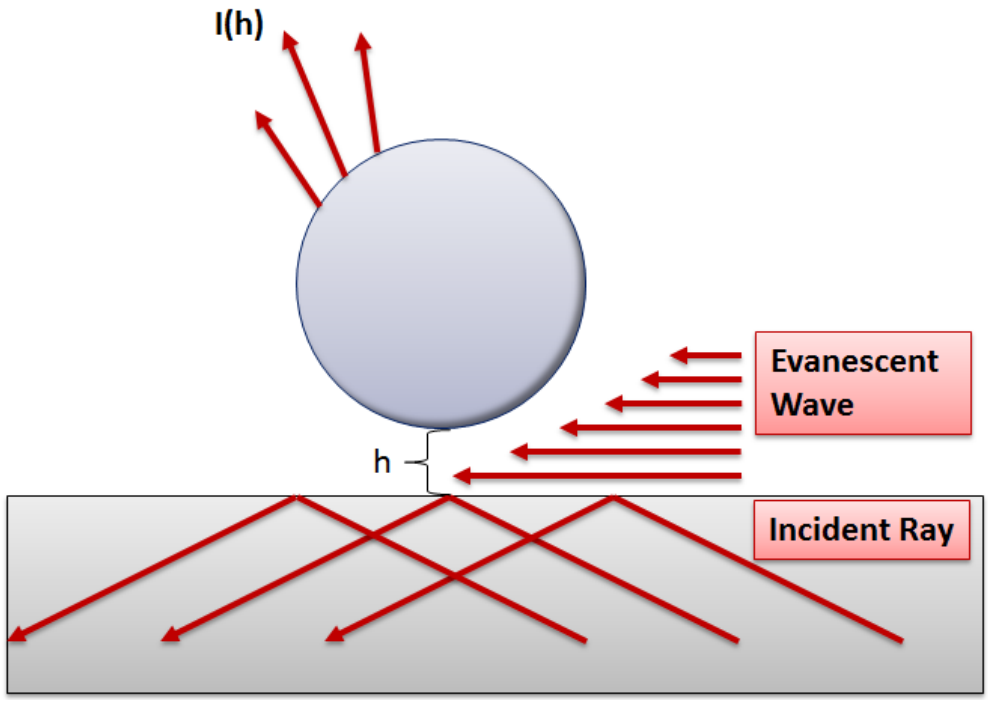

Fig. 3.2. A diagram of a particle scattering light during a TIRM experiment. Light strikes the interface from within a transparent electrode at an angle greater than the critical angle for that interface, engendering an evanescent wave adjacent to the interface. A particle in close proximity to the interface scatters light with an intensity I(h) that depends on the particle height h.

In TIRM, rays of a laser beam strike the interface from within the solid phase at an angle (measured from the normal) greater than the critical angle of that interface, resulting in total internal reflection of the rays and the formation of an evanescent wave that propagates parallel to the interface and whose intensity decays exponentially with distance. Upon interacting with the colloidal particle, light from the evanescent wave is scattered away from the electrode with an intensity that also decays exponentially with the particle-wall separation h. This intensity, measurable by means of a PMT or CCD camera, is given by:

$$\frac{I(h)}{I_m} = \exp[\beta(h_m - h)] \qquad (3.1)$$

where I(h) and I_m are the scattering intensities of a single particle at heights h and h_m, respectively, and β^{-1} is the decay length of the evanescent wave. The parameter h_m is the most probable (mode) height of the particle above the interface at open circuit and I_m is the scattering intensity at that height.

Consider a colloidal particle that has sedimented near to a rigid horizontal surface. If the particle and the surface have sufficient charge of like sign, electrostatic double-layer repulsion prevents the particle from sticking to the solid. The Brownian particle samples elevations according to a Boltzmann distribution given by

$$p(h) = A \exp\left[-\frac{\phi(h)}{k_B T}\right] \tag{3.2}$$

where p(h) is the probability density function (PDF) for the particle's instantaneous height, and A is a normalization constant defined such that

$$\int_0^\infty p(h)dh = 1$$

k_BT is the thermal energy and $\phi(h)$ is the potential energy of the particle at separation h. If only double-layer repulsion and gravity act on the particle, the potential energy is given by

$$\phi = B\exp(-\kappa h) + Gh \qquad (3.3(a))$$

where κ^{-1} is the Debye length of the electrolyte, G is the net weight of the particle, and B is the electrostatic parameter approximated as

$$B = 64\pi\varepsilon a\left(\frac{k_B T}{e}\right)^2 \tanh\left(\frac{e\zeta_p}{4k_B T}\right)\tanh\left(\frac{e\zeta_w}{4k_B T}\right) \qquad (3.3(b))$$

Eq. 3.3 does not include van der Waals interactions which become significant only at much smaller values of h than encountered in these experiments. Examples of potential energy profiles calculated using Eq. 3.3 appear in Fig. 3.3 for polystyrene particles with two different radii.

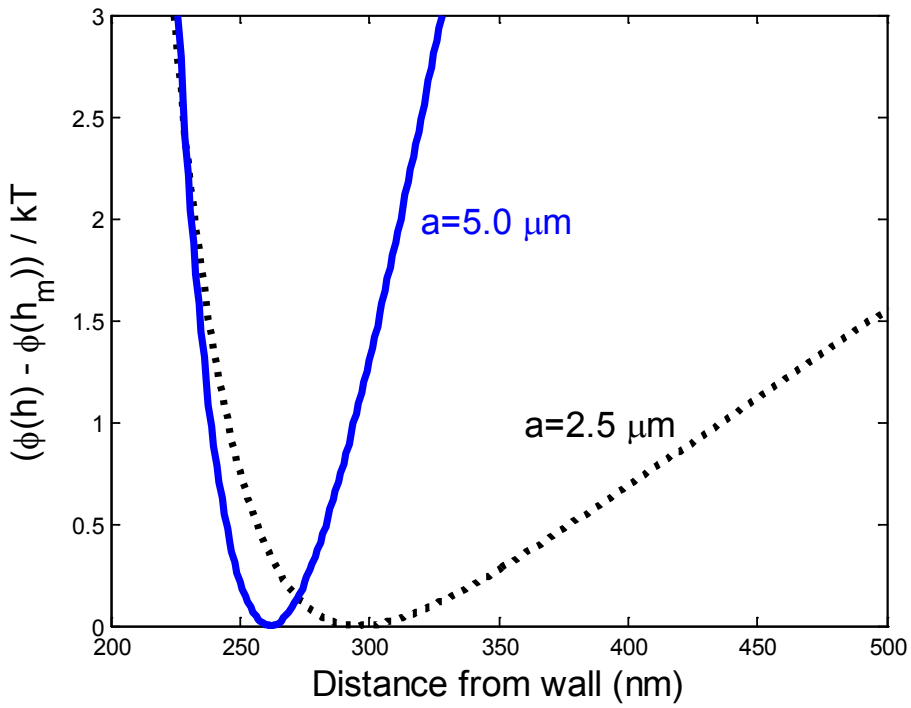

Fig. 3.3. The potential energy of polystyrene particles as a function of separation between the particle and the wall for $\zeta_w = \zeta_p = 100\ mV$ and $\kappa^{-1} = 25$ nm. The increase in ϕ at large separations is a result of the force of gravity on the particle, while the exponential increase in ϕ at small separations is due to electrostatic repulsion.

According to Eq. 3.2, the most probable height of these particles above the surface is the height corresponding to minimum potential energy. This is also the height at which the forces sum to zero (as in Eq. 3.5 below). The parameter h_m introduced in Eq. 3.1 represents this mode height in the absence of any imposed electric field. Solving for h in Eq. 3.3, with $d\phi/dh = 0$, thus yields

$$h_m = \kappa^{-1} \ln \frac{\kappa B}{G} \tag{3.4}$$

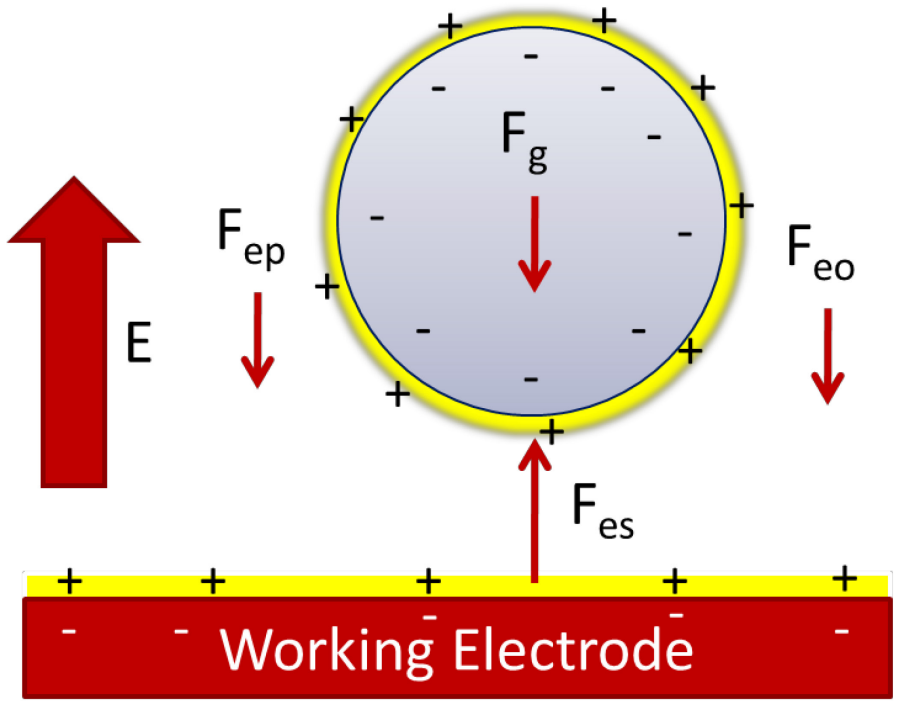

Fig. 3.4. Schematic of the particle-electrode system, where ζ_p and ζ_w are negative. Electrostatic repulsion pushes the particle away from the electrode while gravity pulls the particle down. With E > 0 as shown here, the electrokinetic forces F_{eo} and F_{ep} both pull the particle down towards the electrode surface. If E < 0, these forces would reverse direction as well.

When the solid is an electrode and an electric field E_∞ is imposed, additional forces act on the charged particle, as shown in Fig. 3.4 for the case where E_∞ is positive, and ζ_p and ζ_w are negative. We denote the new most-probable height as h'_m where

$$F_g + F_{es}(h'_m) + F_{ep}(h'_m, E_\infty) + F_{eo}(h'_m, E_\infty) = 0 \qquad (3.5)$$

In this work, a prime on the variable denotes a quantity measured or inferred in the presence of a non-zero electric field. The sign convention adopted for the

forces in Eq. 3.5 is that any force or E_∞ directed away from the electrode is positive. F_g is the particle's weight:

$$F_g = -\frac{4}{3}\pi a^3(\rho_p - \rho_f)g = -G \qquad (3.6)$$

ρ_p and ρ_f are the density of the particle and the fluid, respectively, a is the radius of the particle and g is the acceleration due to gravity. F_{es} is the electrostatic double-layer repulsion between the particle and the surface,

$$F_{es} = \kappa B exp(-\kappa h) \qquad (3.7)$$

F_{ep} is the electrophoretic force caused by the electroosmotic flow generated by the action of the electric field on the diffuse cloud on the particle;

$$F_{ep} = C(h)6\pi\varepsilon a\zeta_p E_\infty \equiv Q_{ep}E_\infty \qquad (3.8)$$

ζ_p is the zeta potential of the particle in question; ε is the electric permittivity of the fluid; and C(h) is a wall hindrance factor that weakly depends on h and is defined by Eq. 3.9.

$$C(h) = \frac{1.554+h/a}{0.300+h/a} \qquad (3.9)$$

Solomentsev et al. deduced this relationship as an empirical fit to numerical calculations by Keh & Lien,[22,23] derived in the limit of fast electrochemical reaction kinetics and a uniform potential adjacent to the electrode surface. The coefficients of E_∞ in Eq. 3.8 can be lumped into Q_{ep}, which represents the effective electrokinetic charge on the particle. Q_{ep} is not the actual charge fixed to the particle; the enveloping counterion cloud shields most of the true charge.[17]

F_{eo} in Eq. 3.5 is the force on the particle as a result of electroosmotic flow generated by the action of the electric field on the diffuse cloud <u>on the electrode</u>. In the limit of uniform potential on the electrode surface, the tangential electric field vanishes at the electrode; hence, no lateral electroosmotic flow occurs along the electrode, i.e. $F_{eo} = 0$ for a uniform potential on the electrode.[24]

The function C(h) is approximately constant for the range of heights h_m probed in this work; $C \approx 4.5$. Therefore, Q_{ep} can be treated as a constant whose value can be calculated from Eq. 3.8. Substituting Eqs. 3.6, 3.7 and 3.8 into Eq. 3.5 and solving for the equilibrium particle-wall separation, h'_m, in the presence of an electric field yields

$$h'_m = \kappa^{-1} \ln \frac{\kappa B}{G - Q_{ep} E_\infty} \qquad (3.10)$$

Substituting Eqs. 3.4 and 3.10 into Eq. 3.1, taking $h = h'_m$, and $I(h) = I'_m$, and then solving for E_∞ yields:[17]

$$E_\infty = \frac{i}{\sigma} = \frac{G}{-Q_{ep}}\left(\left[\frac{I'_m}{I_m}\right]^{\frac{\kappa}{\beta}} - 1\right) \qquad (3.11)$$

Given measured scattering intensities I'_m and I_m that correspond to the most probable elevations of the particle with and without the applied electric field, respectively, and after calculating Q_{ep} from Eq. 3.8 and G from Eq. 3.6, one uses Eq. 3.11 to calculate the local electric field strength E_∞ or the local current density i, where σ is the specific conductance of the solution. The exponent $\kappa\beta^{-1}$ is approximately 5 in typical conditions, which makes the inferred E_∞ quite sensitive to the measured intensities.

3.2.1 Theory for single particles with a uniform current density on the electrode

The expressions for F_{ep} and F_{eo} are different, however, for a uniform current distribution on the electrode under the particle. Yariv[25] evaluated the electroosmotic and electrophoretic forces using an asymptotic analysis valid when the Debye length κ^{-1} is infinitesimal compared to the other length scales h and a; thus $\kappa^{-1} << h << a$.

$$F_e = F_{ep} + F_{eo} = 3E_\infty \varepsilon\pi\left(\frac{a^2}{h}\right)\left(\zeta_w + \zeta_p\right) \qquad (3.12)$$

Here, ζ_w is the zeta potential of the electrode surface. The simple addition of zeta potentials of the wall and particle means that F_{eo} and F_{ep} contribute equally (at least when $\zeta_w = \zeta_p$) to the total force on the particle in the limit of small h.

Owing to the significant dependence of F_e on h, Eq. 3.5 can no longer be solved explicitly for h'_m; no closed-form expression like Eq. 3.11 for the E_∞ is possible in this case. Instead, we must first infer h'_m from the measured scattering intensities and then calculate E_∞ from Eq. 3.5. Here are the necessary steps:

- I_m is first determined by monitoring the scattering intensity of the particles with no applied electric field over a long time and determining the intensity corresponding to the minimum potential energy.
- The corresponding elevation h_m must be calculated from Eq. 3.4 using values of B estimated from Eq. 3.3(b) and G from Eq. 3.6.
- Given some average intensity $I(h'_m)$, averaged at one voltage over multiple cycles of a CV scan, one can then estimate the corresponding elevation from Eq. 3.1, which is assumed to represent h'_m. In previous implementations of this algorithm,[17] no attempt was made to correct for the difference between the intensities corresponding to the mean and mode particle heights, although corrections similar to those described below for ensembles could be made.
- Once h'_m is thus determined, E_∞ can finally be calculated as the root of Eq. 3.5 after Eq. 3.12 is substituted.

3.2.2 Theory for single particles with a current density governed by arbitrary electrode kinetics

Calculations based on the two limiting cases described in the previous sections indicate that the current distribution beneath each particle profoundly affects the force on the particle. Calculating the electrical forces F_{ep} and F_{eo} is much more complicated, however, if neither the potential nor the current is uniform on the electrode around the particle. The current density distribution then depends in general on two parameters, J and δ.[24]

$$J \equiv \frac{(\alpha_a+\alpha_c)ae}{\sigma k_B T} i_0 \tag{3.13}$$

$$\delta \equiv \frac{(\alpha_a+\alpha_c)ae}{\sigma k_B T} i_{avg} \tag{3.14}$$

where α_a and α_c are the coefficients of symmetry for the anodic and cathodic reactions, respectively, i_0 is the exchange current density, e is the elementary charge and i_{avg} is the actual current density averaged over the surface of the entire electrode. J and δ are therefore dimensionless current densities. In the limit of $J \gg 1$ or $\delta \gg 1$, the potential is uniform on the electrode under the particle because the electrode kinetics are facile; Eq. 3.11 was derived in this limit. In the opposite limit of $J \approx \delta \ll 1$, the current density (instead of the potential) becomes increasingly uniform under the particle.

Recent work employed a finite element analysis to determine the relationship between the electrokinetic forces on these particles, the electrode

kinetic parameters J, δ, and h/a for arbitrary particle size and zeta potential.[26] This advance allows calculation of the electrokinetic forces for any pair of J and δ. Given the large differences between forces reported in analytical studies under the assumption of either a uniform current density or uniform potential at the electrode surface, this contribution improves the estimate of current density calculated from the motion of the colloidal particles. Given values of J≈2 and δ < 0.005, which are characteristic of a fast reaction on the electrode below the particle, the electrophoretic and electroosmotic forces on the particle can then be closely approximated by the following separate expressions, which are empirical fits to numerical results from those investigations.[26]

$$F_{eo}(h) = \varepsilon a \zeta_w E_\infty \frac{1.459}{\left(\frac{h}{a}+0.02110\right)^{1.3}} \qquad (3.15(a))$$

$$F_{ep}(h) = \varepsilon a \zeta_p E_\infty \frac{11.82}{\left(\frac{h}{a}+0.1002\right)^{1.3}} \qquad (3.15(b))$$

3.2.3 Theory for particle ensembles

Using measurements of the light scattered by multi-particle ensembles complicates the analysis (even if the particles are acting as independent scatterers) because summing over multiple particles at different elevations erases information needed to form the probability distribution. Consider the open-circuit case. If the ensemble contains a very large number of identical particles and the total scattering intensity is divided by the number of particles, we measure the

mean scattering intensity I_a which differs from the intensity corresponding to the most probable elevation, I_m. One solution is to use the expected potential energy profile and Boltzmann's equation to calculate the distribution and the ratio of the two intensities.

According to the ergodic hypothesis, the mean of any fluctuating property of a single particle over a long time is the same as the instantaneous mean of a very large ensemble of identical independent particles observed at a single time. In particular, if the property is the scattering intensity, then

$$\frac{I_{a,single\ particle}}{I_m} = \frac{I_{a,ensemble}}{I_m} \equiv \theta \qquad (3.16)$$

Assuming enough samples of the intensity are observed to avoid statistical errors in calculating the average, no distinction needs to be made between the I_a/I_m ratios for a single particle and for an ensemble of identical particles because this ratio is the same for each particle. If one determines the ratio θ *a priori* as a function of particle properties, then Eq. 3.16 can be used to convert the measured average intensity values I_a to the intensities corresponding to the mode heights, I_m.

We calculate θ as a function of particle properties first by using Eq. 3.4 to eliminate B from Eq. 3.3:

$$\phi(h) - \phi(h_m) = \frac{G}{\kappa}\left[e^{-\kappa(h-h_m)} - 1\right] + G(h - h_m) \quad (3.17)$$

The height $h = h_m$ is taken as the reference state for potential. Thus $\phi(h_m) \equiv 0$ and Eq. 3.17 becomes

$$\frac{\phi}{k_B T} = \frac{G}{\kappa k_B T}\left(e^{-x} + x - 1\right) \tag{3.18}$$

where $x \equiv \kappa(h - h_m)$. The mean intensity of light scattered from an ensemble of particles can be calculated as

$$I_a = \int_{-\infty}^{\infty} I(x)p(x)dx \tag{3.19}$$

Substituting $I(x)$ from Eq. 3.1 and $p(x)$ from Eq. 3.2, one obtains

$$\theta \equiv \frac{I_a}{I_m} = \frac{\int_{-\infty}^{\infty} \exp\left(-\frac{\beta}{\kappa}x\right)\exp\left(-\frac{\phi}{k_B T}\right)dx}{\int_{-\infty}^{\infty} \exp\left(-\frac{\phi}{k_B T}\right)dx} \tag{3.20}$$

with $\phi(x)$ given by Eq. 3.18. This expression can be evaluated numerically for arbitrary particle properties. Dividing the measured I_a by θ gives I_m, as required by Eq. 3.11 for a single particle or for an ensemble of identical particles.

A similar approach can be used to obtain the ratio of the scattering intensities corresponding to the mode and mean heights of the particle in the presence of an electric field, $I'_a/I'_m = \theta'$. With the inclusion of the total electrokinetic force $F_e = F_{ep} + F_{eo}$ in the force balance from Eq. 3.5 and a reference state of $h = h'_m$, Eq. 3.18 is now expressed as

$$\frac{\phi'}{k_B T} = \frac{1}{k_B T}\left\{\frac{G - F_e(h'_m)}{\kappa}\left[e^{-\kappa(h-h'_m)} - 1\right] + G(h - h'_m) - \int_{h'_m}^{h} F_e(h)dh\right\} \quad (3.21)$$

With a model for F_e like those provided in Eqs. 3.8, 3.12, or 3.15, θ' can be evaluated by substituting ϕ' into Eq. 3.20 and ϕ. Since θ' depends on the electric field E_∞, which is unknown, both θ' and E_∞ must be determined iteratively. An initial guess for E_∞ is first determined from the measured light scattering intensity, I'_a, taking $\theta' = 1$ as an initial guess, using the method outlined above. This electric field can be used to calculate θ', which is then used in the next iteration to convert I'_a to I'_m for determining the new electric field strength. After several iterations, I'_m and θ' converge to constant values. Since θ is not a function of the electric field strength, it remains constant during the iterative process.

While Eq. 3.20 was derived for a single particle, the correction can also be applied to total intensities collected over many particles, assuming that polydispersity in the colloidal sample can be assumed to be negligible. In the case of particle size and charge, which determine in part the values of B and G, one might expect a 5% variation around the mean from one particle to the next in commercially available colloidal suspensions. These small variations around the mean are neglected in this work, because their effect is small in Eqs. 3.11 or 3.20, when averaged.

One potential complication arises because virtually identical latex particles have been observed to scatter light at very different intensities (differing by a factor or two or even four) even when they are located at the same elevation (say

h=0).[27] Bevan et al.[20] have shown that resonant scattering for latex particles in this size range cause the intensity of scattering to be exquisitely sensitive to particle diameter. Fortunately, this resonant-scattering effect is the same at all elevations of the latex particle in the evanescent wave. When ratios of scattering intensity for the same particle are taken (as Eq. 3.20), this sensitivity cancels. Similarly, when the intensity is summed over an ensemble of virtually identical particles having nearly the same θ, and the mean intensity $I_{a,i}$ for each particle is separately converted into the mode $I_{m,i}$ using Eq. 3.20, then this sum of the means is divided by the sum of the modes and the sensitivity from resonance again cancels, leaving the same correction factor as for single particles:

$$\frac{\sum I_{a,i}}{\sum I_{m,i}} = \frac{\sum \theta I_{m,i}}{\sum I_{m,i}} = \theta \qquad (3.22)$$

3.2.4 Brownian Dynamics Simulations

Brownian dynamics simulations were performed following the method of Ermak & McCannon[28] as reproduced in Wirth et al.[17] for ensembles of particles to demonstrate the impact of polydispersity of particle parameters on ensemble average TIRM (EATIRM) experiments. Particles were simulated individually and assumed to be non-interacting. Simulations were performed with a time-step of 2 ms for one simulated hour. The results from these simulations were verified by comparing the potential energy profiles constructed for the simulated particles to potential energy profiles calculated with Eq. 3.3. These calculations allowed

investigation of the effects of particle polydispersity and ensemble size on EATIRM measurements.

3.3 Experimental

A sketch of the apparatus appears in Fig. 3.5. The particles interacted with the evanescent wave from a 632.8 nm, 10 mW HeNe laser, with an incident angle with the interface of 68°. A Photon Technology Inc. photomultiplier tube collected and generated an analog intensity signal subsequently digitized and recorded by a Princeton Applied Research versaSTAT3 potentiostat. The total scattering intensity from ensembles of colloidal particles was recorded during open circuit and cyclic voltammetry (CV) experiments, and used to infer the current density, which was also independently recorded for comparison. In the CV experiments, intensity and current curves were averaged over 20 cycles. The scan rate was 50 mV/s in experiments involving only ITO electrodes, and 15 mV/s during experiments involving gold coated electrodes, to reduce capacitive current.

Transparent, 30-60 nm thick ITO thin film electrodes (Sigma-Aldrich), functioned as the working and counter electrodes. Working electrodes were also prepared by magnetron sputtering thin films of gold on top of the masked ITO surface to make a 2-component surface, with some area of exposed ITO and some area of exposed gold. A thin film of <1 nm of chromium was sputtered first to bond the gold to the ITO surface. Gold films prepared in this manner were approximately 3 nm thick and sufficiently transparent. A thin sheet of silver was

squeezed between PTFE gaskets; its exposed inner cross-section was treated to form a Ag/AgCl reference electrode for the working electrode polarization.

The particles were IDC™ sulfonated latex (Life Technologies) electrostatically stabilized by covalently attached sulfonate groups in the absence of surfactant, giving a corresponding zeta potential of approximately ζ_p=-120 mV. The particles had nominal diameters of 5.6 and 10.1 μm.

Before each experiment, 18.2 MΩ Millipore water was thoroughly purged of atmospheric CO_2 by sparging nitrogen gas through it for two hours; experiments were performed in 0.15 mM KOH solutions. Under these conditions the ITO surfaces have a zeta potential of $\zeta_w \approx$ -80 mV, sufficient to levitate the negatively charged particles electrostatically.

Ensemble average measurements were acquired with particle coverage of 5-10% on the electrode surface. The field of view was approximately 150 μm x 150 μm, with 20-30 particles scattering light from that area.

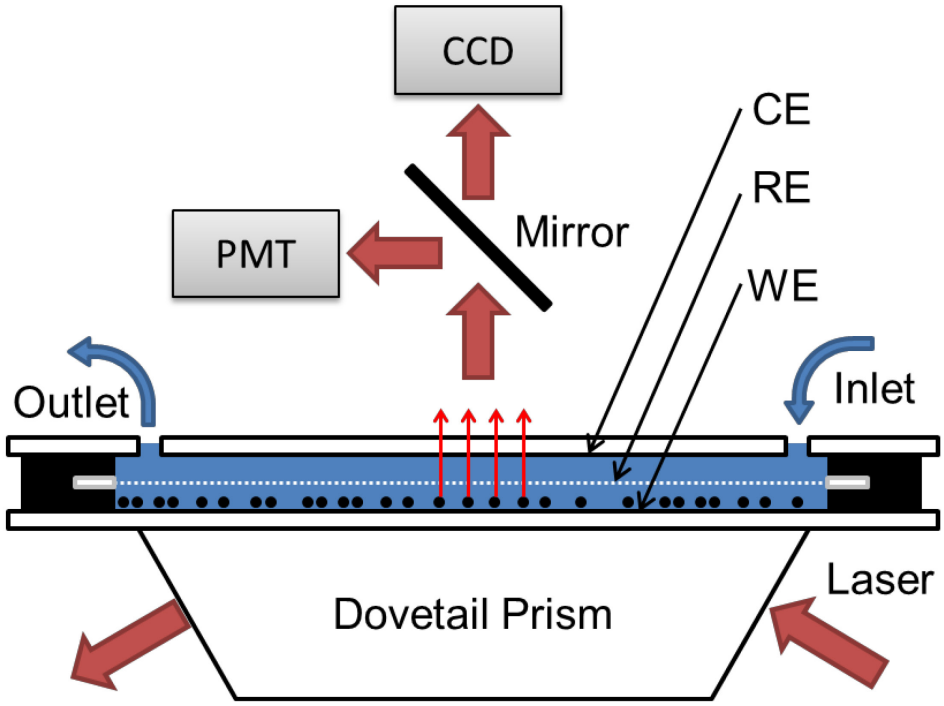

Fig. 3.5. Schematic of the TIRM apparatus used in patch-level ensemble average experiments. The working electrode (WE) and counter electrode (CE) are conductive layers of ITO on glass slides. The reference electrode (RE) is a thin Ag/AgCl sheet sandwiched between two Teflon gaskets to ensure insulation and seal.

3.4 Results & Discussion

3.4.0 Determination and use of the correction factor θ

The Brownian dynamics simulations generate intensity-based PDFs to simulate the total scattering intensity that would be measured in experiments using ensembles of particles, and to gain insight into the mean heights of the particles in those ensembles. The probability distributions of the mean intensity and mean particle-wall separation for ensembles of varying numbers (n) of identical simulated particles appear in Fig. 3.6. The asymmetry present in the single-particle PDFs in both Fig. 3.6(a) and 3.6(b) reflects the asymmetric expo-

linear nature of the potential energy profiles appearing in Fig. 3.3. Note that due to the non-linear relationship between particle height and scattering intensity, the scattering intensity I_m at the most probable height of the particle does not correspond to the most probable scattering intensity for that particle.[29] This can be seen in this figure, where h_m (see 3.6(b)) corresponds to the peak of the single particle height PDF, while I_m (see 3.6(a)) does not correspond to the peak of the single particle intensity PDF. Also, h_a does not correspond exactly to the peak of the 10-particle PDF in Fig. 3.6(b). The distribution becomes increasingly Gaussian around this mean with increasing numbers of particles, but becomes wholly symmetrical about h_a only as $n \to \infty$.

As the number of particles increases, the PDFs become more symmetric around the mean intensity of the particles, I_a, and the mean particle height h_a. Since the height PDF is skewed toward higher elevations where the light scattering is less, $h_a > h_m$ and I_a must always be less than I_m. As a result, using the raw average intensity I_a in place of I_m in Eq. 3.11 results in an over-prediction of the current density.

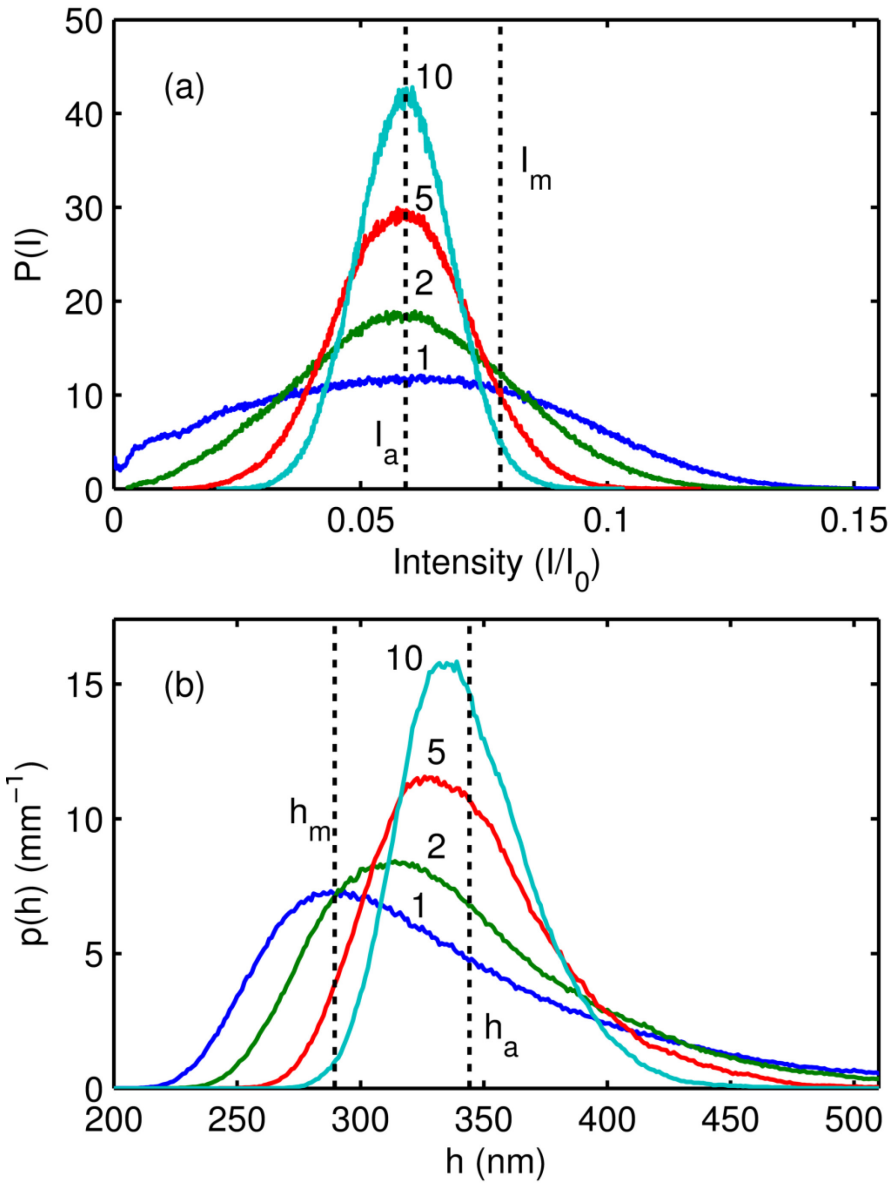

Fig. 3.6. (a)The probability density functions for simulated total scattering intensity (divided by the number of particles) and (b) the mean height h of ensembles of varying numbers of particles during open circuit experiments. Simulated parameters correspond to expected experimental values: a=2.65μm, ζ_p=-80mV, ζ_w=-123mV, $\sigma = 25\ \Omega^{-1}cm^{-1}$. I_0 is the intensity of light scattering when h=0. Note (see (b)) that the peak of the mean height distribution shifts from the most probable height of the particles, h_m, towards the time-averaged mean height of the particles, h_a, with increasing ensemble size.

The correction factor θ, defined in Eq. 3.16, was calculated for polystyrene particles over a range of sizes, both from simulation data and from Eq. 3.20, as shown in Fig. 3.7. The line indicates θ as calculated from Eq. 3.20. The points indicate the ratio of the sum of the scattering intensities for an ensemble of particles to the sum of the I_m values for that ensemble of particles for two ensembles of 40 particles: one of identical particles, and one of particles which had arbitrary I(h=0) values ranging from values of 1 to 2. All three sets of values fall on the same curve, as expected from the arguments advanced in the Theory section.

The correction factor θ approaches unity as the size of the particles increases because the potential energy well becomes more symmetric with a larger force of gravity on the particle, as seen in Fig. 3.3. These results point to two possible options for avoiding the over-prediction of current based on inaccurate I_m values obtained in ensemble average measurements. 1. Using larger or denser particles minimizes the impact of this effect in the first place. 2. Given sufficient physical information about the system to compute θ and θ' using Eq. 3.20, this I_a/I_m ratio can be divided out of the measured I_a value to give the true value of I_m for use in calculating the current density.

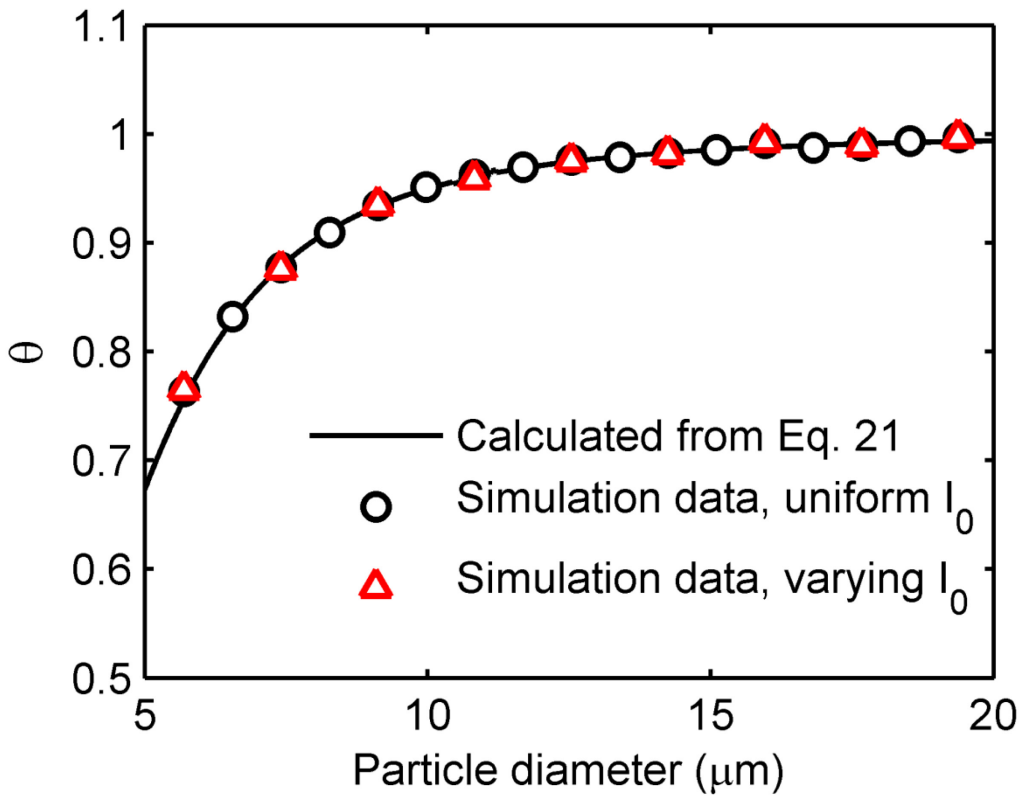

Fig. 3.7. θ is the ratio of I_a measured in ensemble experiments, which is also the mean light scattering intensity of a single particle, to the actual average I_m for the particles in that ensemble, defined as the light scattering intensity of the particles at the minimum of their potential energy wells. The larger the particle, the more symmetric the probability distribution and the closer the mean and mode heights are to each other.

Both of these methods are demonstrated in Fig. 3.8, which shows the anodic region of a CV curve acquired from an ITO electrode. CV experiments were performed with a scan rate of 50 mV/s, with a minimum voltage of 0V and maximum voltages of 1.0V and 0.95V for the 5.7 μm and 10.1 μm particles, respectively. The maximum voltage necessary to obtain similar current densities in these experiments varied due to variations in the pH of the electrolyte. The currents were measured externally in the conventional way and were calculated from the measured average scattering intensity of an ensemble of particles with

the aid of Eq. 3.11. Given the experimental parameters presented here, Q_{ep} = -2.11×10^{-14} C and -3.69×10^{-14} C for the 5.7 and 10.1 μm particles, respectively. Note that use of Eq. 3.11 means that the potential at the electrode was taken as uniform. The region on the right of the plots indicates anodic current. Hydroxyl ion is being oxidized on the electrode to form oxygen at a rate, i.e. faradaic current, that increases with increasing voltage. To the left, at voltages less than 800 mV, only capacitive current charges the ITO surface and the electric double layer at the interface with a current density that depends only on the CV scan rate. In the case of the 5.7 μm particles, the current calculated using the as-measured ensemble-average intensity I_a exceeds the electrically measured current density by almost a factor of four. The use of the raw I_a also overpredicts the current when the larger, 10.1 μm particles were used as the probe particles, but by much less. The calculated θ values for these particles were 0.76 and 0.95, for the 5.7 and 10.1 μm particles, respectively. The value of θ' calculated with Eqs. 3.20 and 3.21 varied over the course of the experiments, as it is a function of the electric field strength. In the case of the 5.7 μm particles, θ' varied from 0.52 to 0.97 for a negative and positive electric field, respectively. For the 10.1 μm particles, θ' varied from 0.90 to 0.99. Dividing the measured I_a and I_a'values by θ and θ', respectively, gives the red curves in Fig. 3.8. In both cases the current calculated after applying the corrections matched the externally measured current density much better than the current density calculated from the as-measured average intensities.

The impact and necessity of the θ and θ' corrections is substantially less if larger particles are used in imaging ammeter experiments. In subsequent experiment and analysis, 10.1 micron particles were used exclusively, reducing the effect of the θ and θ' corrections.

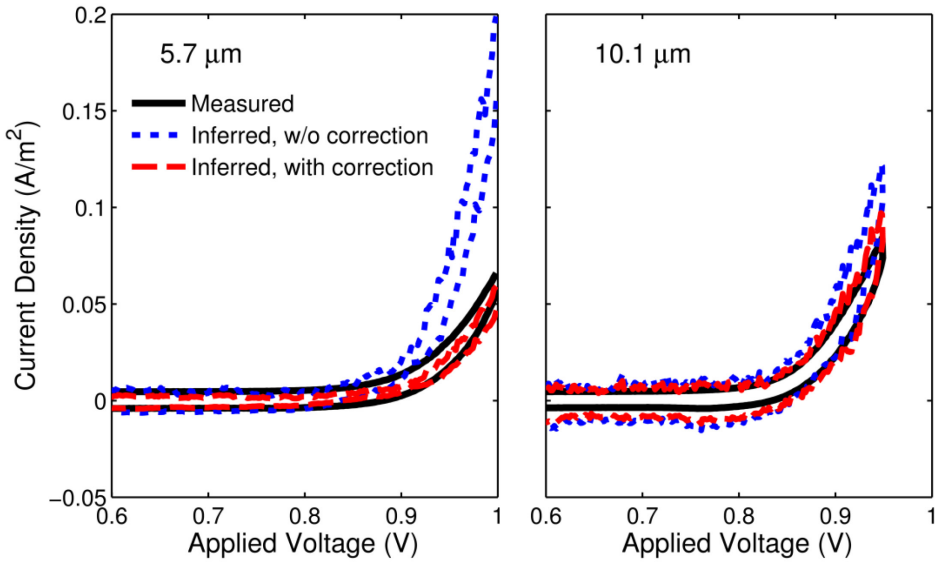

Fig. 3.8. Currents calculated from ensemble average electrochemical TIRM experiments, for particles of two sizes, with and without correcting the scattered light intensity to account for the difference between the mean of the scattering intensity distribution and the desired scattering intensity corresponding to the most probable height of the particles. The agreement is much improved when heavier particles, with smaller differences between the mean and mode heights, are used.

3.4.1 Distinguishing between gold regions and ITO regions on the same electrode

CV experiments were performed using 10.1 μm particles on an electrode with side-by-side areas of ITO and gold in order to demonstrate the applicability of this method to electrodes having a heterogeneous surface composition (extreme in this case). The measured scattering intensity over the two areas of the electrode are shown in Fig. 3.9. From these raw data, the difference in particle behavior between the two regions of the electrode are readily apparent. The particles over the ITO section of the electrode do not stray far from their equilibrium position regardless of applied voltage, which results in a scattering intensity that does not vary significantly over the course of the experiment. The particles over the gold portion of the electrode do react to the electric field resulting from the applied voltage, resulting in scattering intensity that varies substantially during the CV, as seen in this plot.

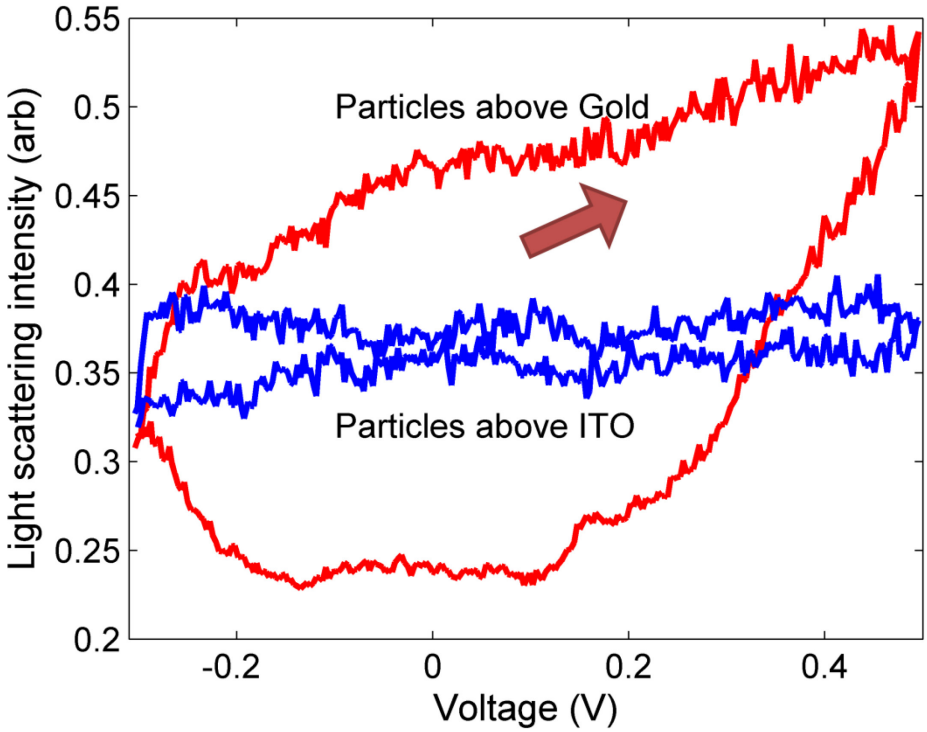

Fig. 3.9. Light scattering intensity measured from ensembles of particles adjacent to two portions of the same electrode: one region where the electrode surface was gold, and another region of exposed indium doped tin oxide (ITO), as a function of applied voltage vs. a Ag/AgCl reference electrode. From these raw intensity data, the differentiation between the two regions of the electrode is clear. Direction of the CV sweep is indicated by the arrow.

From these intensity data, the mean of the most probable particle heights for the particles in the ensemble were calculated by first correcting the measured intensities with Eqs. 3.20 and 3.21, and using Eqs. 3.1 and 3.4 to obtain the particle-wall separation values. These data are plotted as a function of applied voltage in Fig. 3.10. In this plot we can see quite clearly that the particles over the gold are drawn down towards the electrode on the upswing of the CV, coming into closest approach to the electrode surface at the maximum polarization of 0.5 V. The calculated heights for the particles over the ITO portion of the electrode

do not vary far from h_m, as expected due to the minimal current passing through that portion of the electrode.

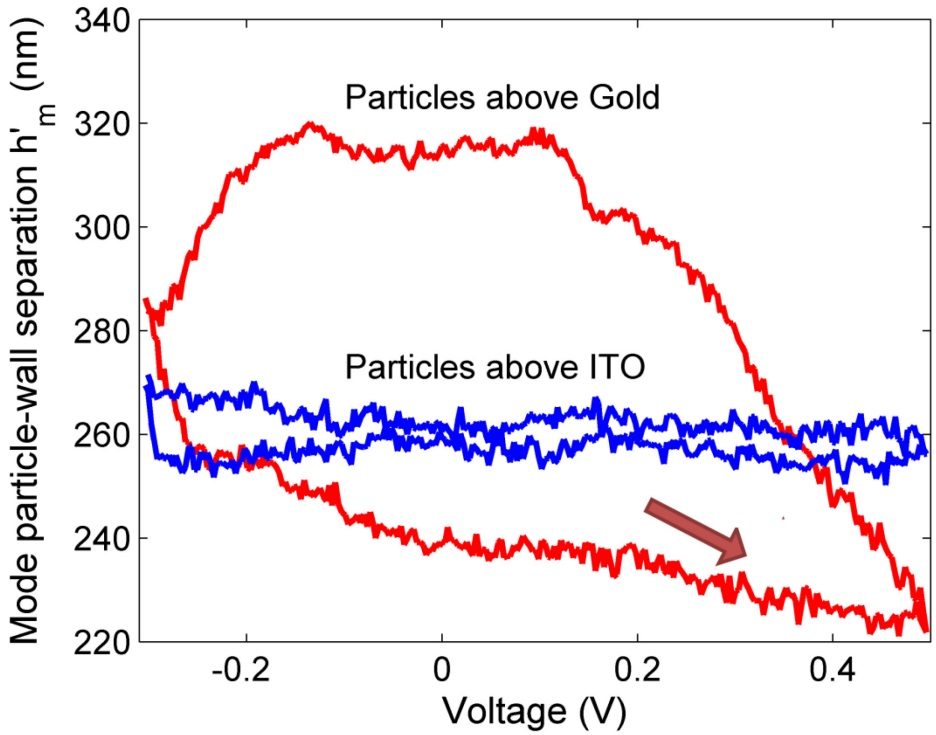

Fig. 3.10. The average of the most probable heights of particles in ensembles adjacent to two portions of the same electrode: one region where the electrode surface was gold, and another region of exposed indium doped tin oxide (ITO), as a function of applied voltage vs. a Ag/AgCl reference electrode. The particles over the gold portion of the electrode move in response to the electric field in their vicinity, while the particles over the ITO portion of the electrode do not stray far from h_m. Direction of the CV sweep is indicated by the arrow.

While direct measurement of the current was in principle no longer possible because the current density was not uniform over the entire electrode, the known inertness of the ITO in the -0.3V to 0.8V window (see Figure 8) allowed the assumption that only capacitive current was passing on the ITO region of the electrode surface. Given the known capacitance of these ITO films, the coverage fraction of the gold film, and the measured total current, we determined the actual

current density on the gold and ITO portions of the electrode from the total current passing through the electrode as a function of applied voltage. These current densities are compared with the currents inferred from the measured particle scatter of an ensemble of 10 μm particles in Fig. 3.11. The current density on the ITO was much smaller than the current density on the gold. A larger current density through the gold electrode might be expected because gold is a better catalyst than ITO for the oxygen evolution reaction. The ~0.04 A/m^2 difference between the current on the upper and lower halves of the CV on the gold surface, however, indicated substantial capacitive-like charging of the gold by comparison with ITO. Capacitive current on the gold electrode should not differ from that on the ITO by enough to account for this discrepancy. Another possible explanation for this opening in the CV is another electronic process occurring at the electrode, taking place at the interfaces between the ITO, the chromium and the gold that were layered in that region of the electrode. Indeed, the thickness of the thin gold layer was visibly reduced after the experiments, indicating that some destructive process was occurring in that region of the electrode.

The imaging ammeter clearly distinguishes current density on the two regions of the electrode, whatever the reason for that difference. In fact the scattering response confirms that most of the current is crossing the interface through the gold. On the ITO portion of the electrode, the particles responded weakly to the applied voltage. The variations in intensity of scattering from this region were low and yielded a very small inferred current. The current calculated

from the light scattering in the gold-coated region in the same experiment was substantial by comparison in the same voltage range. The current density calculated from scattering over the gold surface followed the trend of the measured current density but over-predicted the magnitude of the current. The reason and cure for that over–prediction is described in the next section.

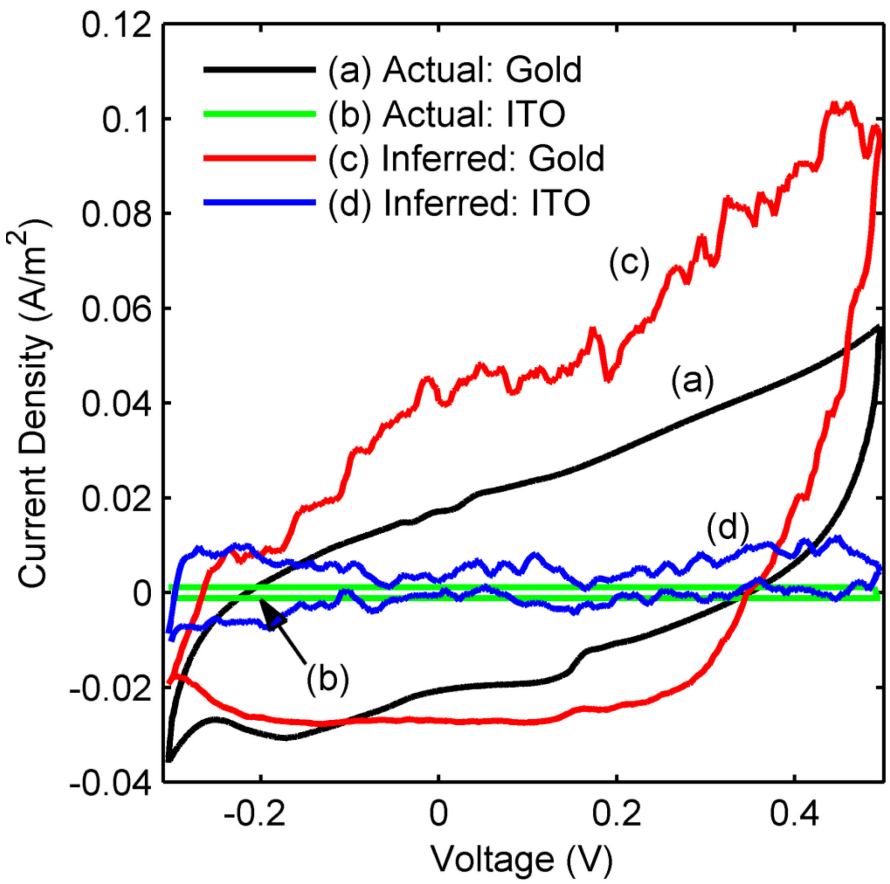

Fig. 3.11. Actual and inferred current densities normal to gold and ITO coated sections of the electrode. Inferred currents are calculated from Eq. 3.11, after applying the appropriate corrections to I_m and I'_m. The response of the gold is easily distinguishable from the response of the ITO, but the difference between the inferred current on gold and the actual current on gold indicates something is missing in the model.

3.4.2 The effect of current density distribution below the particles

The current calculated from the scattering data and presented in Fig. 3.11 were obtained using Eq. 3.11, thereby neglecting electroosmotic flow along the electrode surface under the assumption that the potential distribution under the particles was uniform. Non-uniformity of current distribution around each particle can affect the force that the particle experiences. The force on a 10.1 μm particle as a function of particle height and potential distribution is plotted in Fig. 3.12, normalized by the electrophoretic force that particle would feel far from the electrode surface. As stated in the theory section, the Keh & Lien model assumes a uniform potential across the electrode under the particle, the Yariv model assumes uniform current density on the electrode under the particle, and intermediate cases, where neither the current or potential distributions are uniform, have been computationally explored in other studies.[22,25,26,30] As seen in Fig. 3.12, the magnitude of the combined electrophoretic and electroosmotic force is significantly larger with the assumption of uniform current density on the electrode, as expected.

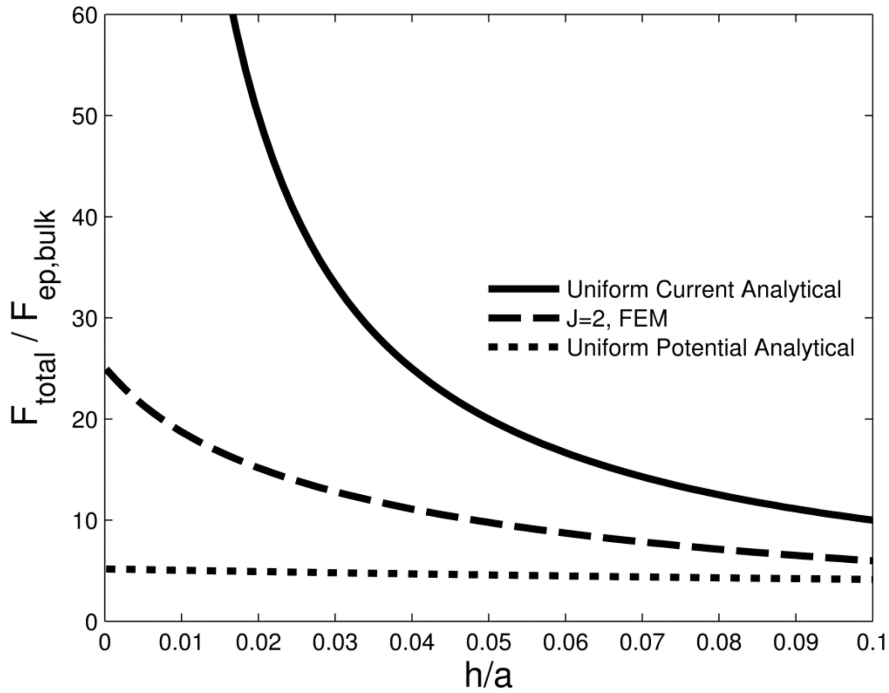

Fig. 3.12. The total electrokinetic force on a colloidal particle as a function of the separation between the particle and the nearby electrode, normalized by the electrophoretic force that particle would feel at large h. Curves are plotted for analytical solutions in the limiting cases of electrode kinetics, and one intermediate case. The current distribution in the immediate vicinity of each particle profoundly affects the force on the particle.

Incorporating the force terms given in Eqs. 3.12 and 3.15 into the current calculation, which means positing that the electric potential distribution below the particle was nonuniform, current densities were calculated from the particle ensemble scattering intensity data shown in Fig. 3.9, used to construct Fig. 3.11. These calculated current curves are plotted in Fig. 3.13, compared to the data calculated using Eq. 3.11.

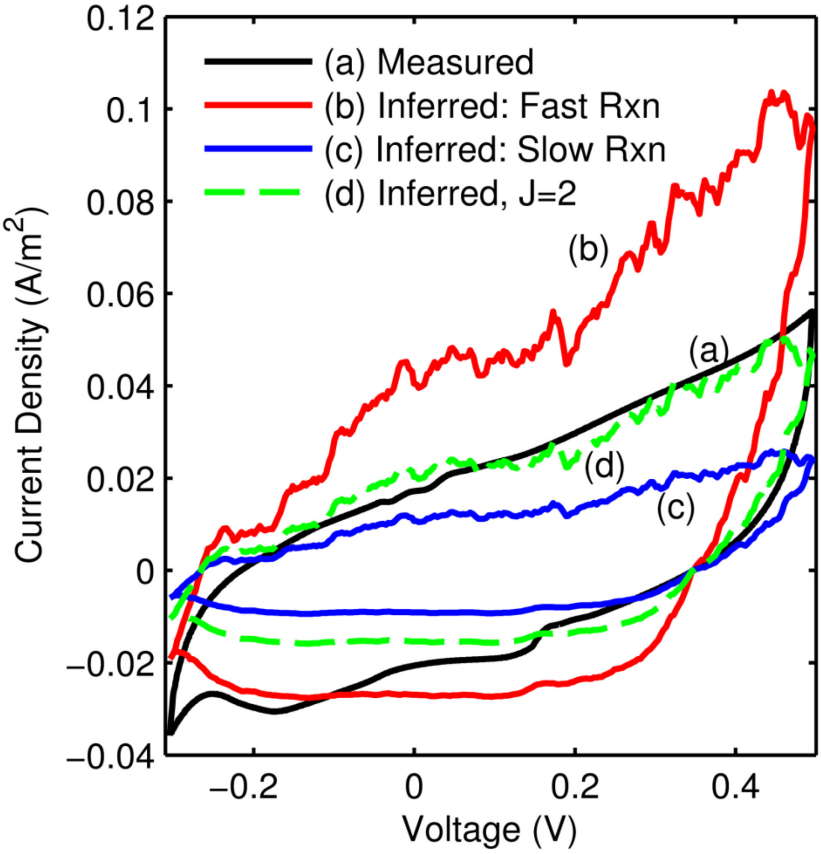

Fig. 3.13. The actual current passing through a gold electrode is plotted, along with currents inferred from measured light scatter from particles adjacent that electrode. The three inferred current plots represent data calculated assuming the three electrokinetic models represented in Fig. 3.12. The currents calculated assuming limiting kinetic cases bracket the actual current, which closely approximates the intermediate case.

Given $\zeta_p < 0$ and $\zeta_w < 0$, the agreement between the measured current and the current inferred from the light scatter is best when $E_\infty > 0$, where the particles are pulled towards the electrode surface. When $E_\infty < 0$ such that $F_e > G$, the particles are electrokinetically driven away from the electrode with a non-zero velocity. This precludes accurate application of the methods described here for electric fields which push the particle strongly away from the wall, since the analysis performed here assumes a steady-state particle-wall separation, and

because the particles rapidly leave the evanescent wave as they move away from the wall.

Eq. 3.8 represents the smallest estimate of electrokinetic forces because the electroosmotic force F_{eo} on the particle is zero for uniform potential on the electrode below the particle. The consequence of an assumed uniform potential distribution is an upper limit in the current density back-calculated from the scattering. More current is required to cause a given change in scattering intensity when the force per unit current is less. On the other hand, assuming a uniform current density maximizes the potential gradients under the particle and therefore the electrokinetic forces, resulting in the force term given in Eq. 3.12. This, conversely, results in a minimum in the calculated current, because much weaker electric fields, now with lateral components producing electroosmotic flow near the electrode, would exert the same amount of force on the particle and give the same change in measured scattering intensity. The electrokinetic forcing terms derived from finite element calculations for J=2 result in a calculated current between the two limiting cases.[26] This is all substantiated by the results in Fig. 3.13: the two limiting cases frame both the actual current density and the current density calculated using Eq. 3.15 for F_{eo} and F_{ep}.

3.5 Conclusions

Adapting the imaging ammeter method as previously put forth for analysis of CSAF electrocatalysts surfaces necessitates average measurements over tens of particles in patch areas on the order of 100 μm in size, due to imaging constraints on the system. Previously proposed theory for translating measured scattering intensities into current densities has been adapted in this work with the inclusion of a correction factor on the measured open and closed circuit intensities. This was done to address the fact that the intensities measured in ensemble experiments correspond to the average location of the particles, not the most probable, or minimum energy, location as required by the theory. This error results in an overprediction of current density based on TIRM measurements if not corrected. The use of larger or denser colloidal particles was also found to partially obviate the need for this correction factor.

Ensemble average TIRM experiments were done on ITO surfaces with 5.7 and 10.1 μm diameter particles to investigate the impact of this correction factor. It was found that the current inferred from measured scattering intensities without the inclusion of the correction factor overshot the externally measured current densities to a much greater extent in the 5.7 micron particle case than in the 10.1 micron particle calculations. In both cases the application of the correction factor to the open circuit equilibrium intensities used in current calculations reduced the calculated current to a reasonable approximation for the actual value. In further work, the larger 10.1 μm particles will be used exclusively, in addition to the correction factor.

Experiments were performed with 10.1 μm particles on patterned ITO/gold surfaces to demonstrate the utility of this method on non-uniform electrode surfaces. It was found that qualitative differences in current density between the two surfaces were readily apparent in the calculated current, although quantitative agreement between the calculated and measured current density values is more difficult to achieve. To this end, modification of the electrokinetic forcing terms used in the calculation of current density from scattering intensity was also investigated. The amount of electroosmotic flow along the electrode surface is determined by the potential distribution under the particle, which has two limiting cases: uniform potential, where no electroosmotic flow is present, and uniform current, which maximizes the potential gradients and therefore the electroosmotic flow. This electroosmotic flow results a vertical force on the particle, and changing the model used for this has a profound impact on the calculated current values. It was shown that for particles over a gold surface, currents calculated under the assumption of the two limiting cases framed the actual current density. With an assumed, intermediate potential distribution under the electrode, the calculated current density agreed very well with the measured values.

The next step in the progression of this work is to use the theory and methods developed here to inform future work on CSAF surfaces, collecting data from many patches simultaneously with a CCD camera.

3.6 Acknowledgement

The work presented here was supported by The National Science Foundation under CBET grant 1133082.

3.7 Appendix

What follows is a collection of MATLAB code used to assemble and analyze the measured light scatter data to calculate the current density. For these, a "control" script was written to define overall constants and call the other functions.

```
clear; clc;
tic
% Loads data as a struct with fields for OC (open circuit) and CV
(cyclic
% voltammogram) fields.  The CV fields are formatted as columns
load rawdata_2011_09_29_with_pts;

% This script takes the PMT and versaSTAT data and formats it for
the
% subsequent data analysis
CV_PMT_Handling_2011_09_29;

%Assumed or measured background intensity.  Zero for this data
set.
I_BG = [0 0];

J=2; %dimensionless exchange current density
delta = 0.001; %dimensionless current density
numThetaLoops = 30; % Number of loops for determination of the
active theta value
jumpStep = 4; % To reduce the computational time, every nth point
is analyzed.
              % Total computational time multiplied by 1/jumpStep

I_m_corr = 1/0.9512; %0.9512 is the theta value in the absence of
electric field

i_calc_active_theta;
plots_2011_09_29
toc

save 2011_09_09_data_KL_limit
```

The function i_calc_active_theta is defined below:

```
%Play script
clear sumUp sumDown capCurrDiff %To save memory
close all %closes any open figures

%Variable Inputs

% This code was adapted from previous versions.  These
adjustments helped
% remove copy/paste errors
aveInt = aveInt3;
V=V3;

% scanSpeed = 0.01; %V/Sec
a = 10.1e-6/2; %radius of particles, m
Cn = 0.15; %Nominal concentration of KOH, mM
sigma = 0.00388; %A/V/m
zp = -0.123; %V, zeta of particle
zw = -0.08; %V, zeta of electrode

rho_f = 1000; %Water, kg/m^3
rho_p = 1055; %PS
G=-(4/3)*pi*a.^3*(rho_p-rho_f)*9.81;  %Newtons, buoyant force on
the particle

%Constants
beta = 1/113.7e-9; %1/m, decay length of evanescent wave
eta = 1e-3; %Water at ~300 K, viscosity of water
epsilon = 80*8.854e-12; %(J/(V^2*m)), water
k = 1.38e-23; %J/K
T = 295; % temperature
e = -1.602e-19; %C, elementary charge
R=8.314; %Gas constant, used in calculation of lambda
z=1; %Valence, assumes symmetric electrolyte
F = 96485.3; %A*s/mol
Qstar_eo = (1.909e-8)*epsilon*zw/eta; % Keh&Lien adjustment for
                                      % electrophoretic charge

%Calculated Values
kappa = 1/sqrt((epsilon*R*T./(2*z^2*F^2*Cn)));  %C in mM or
mol/m^3; %1/m,
Qep=6*pi*epsilon*a*zp; %C  Qep = -2.177e-14; %C abouts
B = 64*pi*epsilon*a*(k*T/e)^2*tanh(e*zp/4/k/T)*tanh(e*zw/4/k/T);
%electrostatic parameter

heq = -(1/kappa)*log(-G/(kappa*B)); %equilibrium height,
corresponds to
                                    % h_m in the manuscript

V=V(1:jumpStep:end); %data reduction

cycleLength = length(V);

%% Initialize arrays
theta = ones(numThetaLoops, cycleLength, numPatches);
hm = zeros(cycleLength, numPatches);
```

```
Ch = zeros(cycleLength, numPatches);
i_Keh = zeros(cycleLength, numPatches);
hm_opt = zeros(cycleLength, numPatches);
Ch_opt = zeros(cycleLength, numPatches);
i_Keh_opt = zeros(cycleLength, numPatches);
i_Yariv= zeros(cycleLength, numPatches);
i_Fagan = zeros(cycleLength, numPatches);
i_Fitted = zeros(cycleLength, numPatches);
currentHistory = zeros(cycleLength, numThetaLoops);

%% Calculate currents
for i_ = 1:numThetaLoops

    % This loop adjusts the intensity to facilitate the active
theta
    % correction
    for j_=1:numPatches;
        %I_BG is zero, here.  This is only correcting for the
equilibrium intensity.
        I_m_ens_BGsub(j_) = I_m_corr*(I_m_ens(j_));
        tempo = (aveInt(:, j_) - I_BG(j_)); %This is the averaged
intensity during experiment
        aveInt_BGsub(:, j_)=tempo(1:jumpStep:end)./(theta(i_,:,
j_)');
    end

    %This loop calculates the current densities for the different
assumed
    %current density distributions.
    for j_=1:numPatches;

        % hm is the calculated particle heights as a function of
current
        % density, calculated from the adjusted scattering
intensity
        hm(:,j_) = -log(aveInt_BGsub(:,
j_)./I_m_ens_BGsub(j_))/beta+heq;
        Ch(:,j_) = (hm(:,j_)+1.554*a)./(hm(:,j_)+0.3*a);
%electrophoretic term coefficient, based on particle height
        [FeoStar FepStar] =  EK_Forces(J,delta,hm(:,j_)./a);

        i_Keh(:,j_) =
(G*sigma./(Qep.*Ch(:,j_))).*((aveInt_BGsub(:,j_)./I_m_ens_BGsub(j
_)).^(kappa/beta)-1); %current density without EO, via original
theory
        i_Yariv(:,j_) = -sigma*(G+kappa*B*exp(-kappa*hm(:,j_)))
./ (epsilon*3*pi*(a^2./hm(:,j_))*(zw+zp));
        i_Fagan(:,j_) = -sigma*( (G+kappa*B*exp(-kappa*hm(:,j_)))
./ (Qep.*Ch(:,j_)+Qstar_eo*(a./hm(:,j_)).^0.976));

        i_Fitted(:,j_) = -sigma*( (G+kappa*B*exp(-
kappa*hm(:,j_))) ./ (6*pi*epsilon*a*(FeoStar*zw + FepStar*zp ) )
);
```

```
        % This loop calculates theta with the new current
density, and
        % outputs the progress of the loop
        if i_ ~= numThetaLoops
            for k_=1:length(i_Fitted(:,j_))
                theta(i_+1,k_,j_) =
theta_calc_fun((i_Fitted(k_,j_)/sigma)*(i_/numThetaLoops), a, J,
delta);
                progress = [i_ j_ k_]
            end
        end
    end

    %currentHistory allows for tracking of the calculated
currents with the
    %changing values of theta
    currentHistory(:,i_) = i_Fitted(:,1) ;

end
```

The functions theta_calc_fun, EK_Forces and EK_Forces_Int are required to execute this code:

```
function theta = theta_calc_fun(E, a, J_val, delt)

%% Initialize

epsilon = 80*8.854e-12; %(J/(V^2*m)), water @ T=295
Cn = 0.15; %Nominal concentration of KOH, mM
rho_f = 1000; %Water, kg/m^3
rho_p = 1055; %PS
%rho_p = 1960; %Silica, 2648 from wikipedia
R=8.314; %Gas constant, used in calculation of lambda
I_0=1;
beta = 1/113.7e-9;%1/113.7e-9; %1/m, decay length of evanescent
wave
% beta = 1/3e-08;%1/113.7e-9; %1/m, decay length of evanescent
wave
k = 1.38e-23; %J/K
T = 295;
e = -1.602e-19; %C
zw = -0.08; %V, zeta potential of the electrode
zp = -0.123; %V, base value for zeta potential of particles
z=1; %Valence, assumes symmetric electrolyte
F = 96485.3; %A*s/mol

%% Calculate thetas
close all;
kappa = 1/sqrt((epsilon*R*T./(2*z^2*F^2*Cn)));  %C in mM or
mol/m^3;
```

```
vec_a = a;

vec_G = (4/3)*pi*vec_a.^3*(rho_p-rho_f)*9.81;
vec_B =
64*pi*epsilon*vec_a.*(k*T/e)^2*tanh(e*zp/4/k/T)*tanh(e*zw/4/k/T);
theta = zeros(1, length(vec_a));

% E = 2; %V/m
J=J_val;
delta=delt;


%loops over every particle size input
for i_= 1:length(vec_a)

    G= vec_G(i_);
    B= vec_B(i_);

    hm = log(kappa*B/G)/kappa;

    % This loop iterates to find the new value of h_m.  Usually
it
    % converges after a few iterations
    for j_=1:100
        [Feo_star_hm Fep_star_hm] = EK_Forces(J, delta, hm/a);
        F_EK_hm = 6*pi*epsilon*a*E* (Feo_star_hm*zw +
Fep_star_hm*zp);
        hm_new = log(kappa*B/(G-F_EK_hm))/kappa;
        if abs(hm/hm_new-1)<0.0001;
            j_;
            hm=hm_new;
            break
        end
        hm=hm_new;
    end
    if i_ == 100
        output = 'WARNING maximum iterations on hm determination'
    end

    % Forces and integrated forces calculated in a manner
consistent with
    % the derivation in the manuscript
    [Feo_star_hm Fep_star_hm] = EK_Forces(J, delta, hm/a);
    F_EK_hm = 6*pi*epsilon*a*E* (Feo_star_hm*zw +
Fep_star_hm*zp);
    F_EK_int_hm =  6*pi*epsilon*a*E*(EK_Forces_int(J, delta,
(hm)/a,1)*zw + EK_Forces_int(J, delta, (hm)/a,2)*zp);
    F_EK_int_h = @(hdiff) 6*pi*epsilon*a*E*(EK_Forces_int(J,
delta, (hm+hdiff)/a,1)*zw + EK_Forces_int(J, delta,
(hm+hdiff)/a,2)*zp);


    xi = @(hdiff) kappa*hdiff;
```

```
    phi_kT= @(hdiff) ((G- F_EK_hm)/kappa/k/T) * (exp(-
xi(hdiff))+xi(hdiff)-1) + (F_EK_int_hm-F_EK_int_h(hdiff));

    theta_top_integrand = @(hdiff) exp((-
beta/kappa).*xi(hdiff)).*exp(-1*phi_kT(hdiff));
    theta_bottom_integrand = @(hdiff)  exp(-1*phi_kT(hdiff));

    %Calculation of theta.  Outputs for tracking.  Add a ; to the
statement
    %to suppress it
    theta(i_)=integral(theta_top_integrand,-
1*hm,hm*10)./integral(theta_bottom_integrand,-1*hm,hm*10)

end


%}
%% Calculate theta no force
%{
    % This section calculates the theta correction with no
applied electric
    % field.  This is much quicker than the method shown above.
    hm = log(kappa*B/G)/kappa;

    xi = @(hdiff) kappa*hdiff;
    phi_kT= @(hdiff) (G/kappa/k/T) * (exp(-xi(hdiff))+xi(hdiff)-
1);

    theta_top_integrand = @(hdiff) exp((-
beta/kappa).*xi(hdiff)).*exp(-1*phi_kT(hdiff));
    theta_bottom_integrand = @(hdiff)  exp(-1*phi_kT(hdiff));

    theta(i_)=integral(theta_top_integrand,-
1*hm,hm*10)./integral(theta_bottom_integrand,-1*hm,hm*10);
%}


function [F_EO_star, F_EP_star] = EK_Forces(J,delta,hStar)

%[F_EO_star, F_EP_star] = EK_Forces(J,delta,hStar)
%This takes the variables delta, J, h/a (hStar) and spits out
FEO_Star and
%FEP_star
% Constants format is [Letter]([FEO=1,FEP=2], Subscript), so that
it comes
% out as
% B=[FEO1 FEO2 FEO3
%    FEP1 FEP2 FEP3]

% clear; clc;

Ch = (1.554+hStar)./(0.3+hStar);

lJ = log10(J);
ld = log10(delta);
```

```
A = zeros(2,3);
B = [2.634, -0.1053, 0.9816; 2.847, -0.1052, 0.9883];
C = [0.02834, -3.33, 7.806; 0.02749, -3.309, 8.026];
D = [1.376, -2.728, 8.371; 0.6341, 0.4704, 2.064];
E = zeros(2);
F = [0.2203, 2.555, 1.477, 0.2398; 0.7663, 1.918, 1.194, 0.8044];
G = [-0.04942 1.157, 1.086, -0.05738; -0.7313, 1.718, 1.172, -
0.7677];

%Now we solve for the other parameters, E and A, with the same
format

E(:, 1) = F(:,1) .* erf ( (lJ-F(:,2))./F(:,3) ) + F(:,4);
E(:, 2) = G(:,1) .* erf ( (lJ-G(:,2))./G(:,3) ) + G(:,4);

A(:, 1) = B(:,1) .* erfc ( (lJ-B(:,2))./B(:,3) );
A(:, 2) = C(:,1) .* (exp ( lJ - C(:,2)) + C(:,3));
A(:, 3) = D(:,1) .* erfc ( (lJ-D(:,2))./D(:,3) );


F_EO_star = A(1,1) .* erfc ( (ld-A(1,2))/A(1,3) ) * E(1,1)
./((hStar-E(1,2)).^1.3);
F_EP_star = (A(2,1) .* erfc ( (ld-A(2,2))/A(2,3) ) + Ch ) *
E(2,1) ./((hStar-E(2,2)).^1.3);


function [F_star_int] = EK_Forces_int(J,delta,hStar, idx)

% This function outputs the integral of the EK forces, from zero
to h.
%input delta, J, h/a (hStar) and spits out EO:idx=1,EP:idx=2
%
% Constants format is [Letter]([FEO=1,FEP=2], Subscript), so that
it comes
% out as
% B=[FEO1 FEO2 FEO3
%    FEP1 FEP2 FEP3]

lJ = log10(J);
ld = log10(delta);

A = zeros(2,3);
B = [2.634, -0.1053, 0.9816; 2.847, -0.1052, 0.9883];
C = [0.02834, -3.33, 7.806; 0.02749, -3.309, 8.026];
D = [1.376, -2.728, 8.371; 0.6341, 0.4704, 2.064];
E = zeros(2);
F = [0.2203, 2.555, 1.477, 0.2398; 0.7663, 1.918, 1.194, 0.8044];
G = [-0.04942 1.157, 1.086, -0.05738; -0.7313, 1.718, 1.172, -
0.7677];

%Now we solve for the other parameters, E and A, with the same
format
```

```
E(:, 1) = F(:,1) .* erf ( (lJ-F(:,2))./F(:,3) ) + F(:,4);
E(:, 2) = G(:,1) .* erf ( (lJ-G(:,2))./G(:,3) ) + G(:,4);

A(:, 1) = B(:,1) .* erfc ( (lJ-B(:,2))./B(:,3) );
A(:, 2) = C(:,1) .* (exp ( lJ - C(:,2)) + C(:,3));
A(:, 3) = D(:,1) .* erfc ( (lJ-D(:,2))./D(:,3) );

% A = A*(-10/3);

Ch = @(hStar)(1.554+hStar)./(0.3+hStar);
F_EO_star =@(h) A(1,1) .* erfc ( (ld-A(1,2))/A(1,3) ) * E(1,1)
./((h-E(1,2)).^1.3);
F_EP_star =@(h) (A(2,1) .* erfc ( (ld-A(2,2))/A(2,3) ) + Ch(h) )
* E(2,1) ./((h-E(2,2)).^1.3);
% hStar
if idx == 1
    F_fun = F_EO_star;
else
    F_fun = F_EP_star;
end

F_star_int = zeros(size(hStar));
for j_=1:length(hStar)
    F_star_int(j_) = integral(F_fun,0,hStar(j_));
end
```

3.8 Works Cited

(1) Klemm, S. O.; Kollender, J. P.; Walter Hassel, A. *Corrosion Science* **2011**, *53*, 1–6.

(2) Mardare, A. I.; Yadav, A. P.; Wieck, A. D.; Stratmann, M.; Hassel, A. W. *Science and Technology of Advanced Materials* **2008**, *9*, 035009.

(3) Reddington, E. *Science* **1998**, *280*, 1735–1737.

(4) Prochaska, M.; Jin, J.; Rochefort, D.; Zhuang, L.; DiSalvo, F. J.; Abruña, H. D.; Van Dover, R. B. *Review of Scientific Instruments* **2006**, *77*, 054104.

(5) Barber, Z. H.; Blamire, M. G. *Materials Science and Technology* **2008**, *24*, 757–770.

(6) Smotkin, E. S.; Diaz-Morales, R. R. *Annual Review of Materials Research* **2003**, *33*, 557–579.

(7) Hassel, A. W.; Seo, M. *Electrochimica Acta* **1999**, *44*, 3769–3777.

(8) Wittstock, G.; Burchardt, M.; Pust, S. E.; Shen, Y.; Zhao, C. *Angewandte Chemie (International ed. in English)* **2007**, *46*, 1584–617.

(9) Williams, C. G.; Edwards, M. a; Colley, A. L.; Macpherson, J. V; Unwin, P. R. *Analytical chemistry* **2009**, *81*, 2486–95.

(10) Shan, X.; Patel, U.; Wang, S.; Iglesias, R.; Tao, N. *Science (New York, N.Y.)* **2010**, *327*, 1363–6.

(11) Engstrom, R. C.; Ghaffari, S.; Qu, H. *Anal. Chem.* **1992**, 26, 2525–2529.

(12) Panova, A. A.; Pantano, P.; Walt, D. R. *Analytical chemistry* **1997**, *69*, 1635–41.

(13) Whitacre, J. F.; Valdez, T.; Narayanan, S. R. *Journal of The Electrochemical Society* **2005**, *152*, A1780.

(14) Tevar, a. D.; Whitacre, J. F. *Journal of The Electrochemical Society* **2010**, *157*, A870.

(15) Muster, T. H.; Trinchi, a.; Markley, T. a.; Lau, D.; Martin, P.; Bradbury, a.; Bendavid, a.; Dligatch, S. *Electrochimica Acta* **2011**, *56*, 9679–9699.

(16) Muster, T. H.; Hughes, a. E.; Furman, S. a.; Harvey, T.; Sherman, N.; Hardin, S.; Corrigan, P.; Lau, D.; Scholes, F. H.; White, P. a. *Electrochimica Acta* **2009**, *54*, 3402–3411.

(17) Wirth, C. L.; Sides, P. J.; Prieve, D. C. *Journal of Colloid and Interface Science* **2011**, *357*, 1–12.

(18) Sides, P. J.; Wirth, C. L.; Prieve, D. C. *Electrochemical and Solid-State Letters* **2010**, *13*, F10–F12.

(19) Wu, H.-J.; Pangburn, T. O.; Beckham, R. E.; Bevan, M. A. *Langmuir* **2005**, *21*, 9879–9888.

(20) Wu, H.-J.; Shah, S.; Beckham, R. E.; Meissner, K. E.; Bevan, M. A. *Langmuir* **2008**, *24*, 13790–5.

(21) Wu, H.-J.; Everett, W. N.; Anekal, S. G.; Bevan, M. a *Langmuir* **2006**, *22*, 6826–36.

(22) Keh, H.-J.; Lien, L.-C. *J. Chin. Inst. Chem. Eng.* **1989**, *20*, 283–290.

(23) Solomentsev, Y.; Bohmer, M.; Anderson, J. L. *Langmuir* **1997**, *13*, 6058–6068.

(24) Newman, J.; Thomas-Alyea, K. E. *Electrochemical Systems*; 3rd ed.; John Wiley & Sons, Inc.: Hoboken, NJ, 2004.

(25) Yariv, E. *Journal of Fluid Mechanics* **2010**, *645*, 187.

(26) Rock, R. M.; Sides, P. J.; Prieve, D. C. *Journal of Colloid and Interface Science* **2013**, *393*, 306–13.

(27) Prieve, D. C.; Walz, J. Y. *Applied optics* **1993**, *32*, 1629–41.

(28) Ermak, D. L.; McCammon, J. A. *Journal of Chemical Physics* **1978**, *69*, 1352–1360.

(29) Prieve, D. *Advances in Colloid and Interface Science* **1999**, *82*, 93–125.

(30) Fagan, J. A.; Sides, P. J.; Prieve, D. C. *Langmuir* **2004**, *20*, 4823–34.

Chapter 4

Use of Colloidal Particles for Imaging Amperometry on a Macroscopic CSAF Electrode

4.0 Abstract

High-throughput methods of electrochemical experimentation can increase the pace of discovery of promising new alloys and materials for electrocatalytic applications. A common approach in this field is the deposition and subsequent testing of composition spread alloy film (CSAF) electrodes, which present surfaces with continuously varying compositions. Simultaneous measurement of electrochemical activity across these surfaces allows for rapid selection of optimum alloy compositions for a wide range of applications. Previous work showed that the electrokinetic motion of colloidal particles proximate to electrode surfaces can be measured using total internal reflection microscopy and used to infer the current density at the electrode, with reasonable accuracy compared to electronic current measurements. The strength of this method as compared to traditional electrochemical measurement is that it allows for determination of local current density at any location on an electrode, as opposed to the total current over the available surface. Recently published and submitted work has focused on developing the fundamental theory and methods for translating imaging data into current density from single particles and from average measurements over ensembles of particles, at individual locations on both uniform and non-uniform electrodes. The work presented here demonstrates the

efficacy of this imaging ammeter for measuring the current density across a Ni/Fe CSAF electrode. Light scattering from particles over a region representing a range of compositions from 20% Fe to 100% Fe was collected with a CCD camera and used to infer the current density across that entire composition space as a function of applied voltage. Inferred current densities agree with established trends for the electrochemical activity of this alloy system.

4.1 Introduction

High throughput investigation of electrocatalysts and corrosion resistant materials accelerates discovery of promising new materials and alloys. Using classical electrochemical methods, testing of electrocatalyst alloy combinations is a time consuming and costly process, involving the synthesis of multiple samples with different compositions and testing each individually.[1] One approach for rapid testing utilizes electrodes made from composition spread alloy films (CSAFs), which exhibit continuously varying surface concentrations.[2–14] Deposition of these CSAFs onto electrode surfaces represents part of the challenge in this problem, the other part being the development of an accurate method for measuring the current density at different locations on the same electrode in a single experiment, as traditional electronic measurements of current density yield only the total current passing through the electrode. There are numerous examples of approaches to this problem in the literature, but to date the optimal method combining flexibility, speed, and resolution has yet to be fully developed.[1,15]

There is interest in both serial and parallel methods for characterizing CSAF surfaces for electrocatalysis. The use of a scanning drop cell (SDC) electrode is an example of one serial approach, and a number of imaging methods have also been investigated.[2,4,16–21] In this work, we explore the use of ensemble average total internal reflection microscopy (TIRM) as a method for imaging amperometry. This method involves measuring the light scattering from colloidal particles interacting with an evanescent wave adjacent an electrode surface during electrochemical experiments, translating these measured intensities into information about the motion of the particles. With an appropriate model for the relationship between the electrokinetic forces on the particles and the electric field strength, it is then possible to infer the current density at the electrode from the motion of the particles. Initial work on this imaging ammeter demonstrated that the current density on a tin doped indium oxide (ITO) electrode could be inferred from the motion of a single particle during electrochemical experiments, using a basic model for the electrokinetic forces acting on the particle.[22,23] Further investigations involved a computational study to investigate the significant impact of electrode kinetics on the electrokinetic forces acting on the particle and further work to allow for translation of measured intensities averaged over ensembles of particles to current density.[24,25] Previous experimental studies also showed that the imaging ammeter could distinguish between two regions of varying electrochemical activity on the same patterned gold/ITO electrode.[25]

The current contribution represents the first demonstration of the colloidal imaging ammeter in parallel operation, for measuring current at different points

on a CSAF surface in a single experiment. The nickel/iron alloy system for the oxygen evolution reaction was used as the test case for this study. The behavior of this system has been characterized in the past through more traditional methods: a sharp peak in oxygen generation is observed at 10-20% Fe in the electrode surface, with rapidly decreasing electrochemical activity with increasing iron content in the catalyst.[26–28] The well-understood nature of this catalyst system, the stability of the CSAF electrode in the basic solutions commonly utilized for TIRM, and the established method for deposition of Ni/Fe CSAF films[29] makes this an ideal proof-of-concept case for the imaging ammeter.

4.2 Theory

4.2.0 Measurement of particle motion with TIRM

Total internal reflection microscopy (TIRM) is used in this study to measure the motion of particles proximate to the working electrode. In TIRM, rays of a laser beam strike the interface from within the solid phase at an angle (measured from the normal) greater than the critical angle of that interface, resulting in total internal reflection of the rays and the formation of an evanescent wave that propagates parallel to the interface and whose intensity decays exponentially with distance. A schematic of this system is shown in Fig. 4.1.

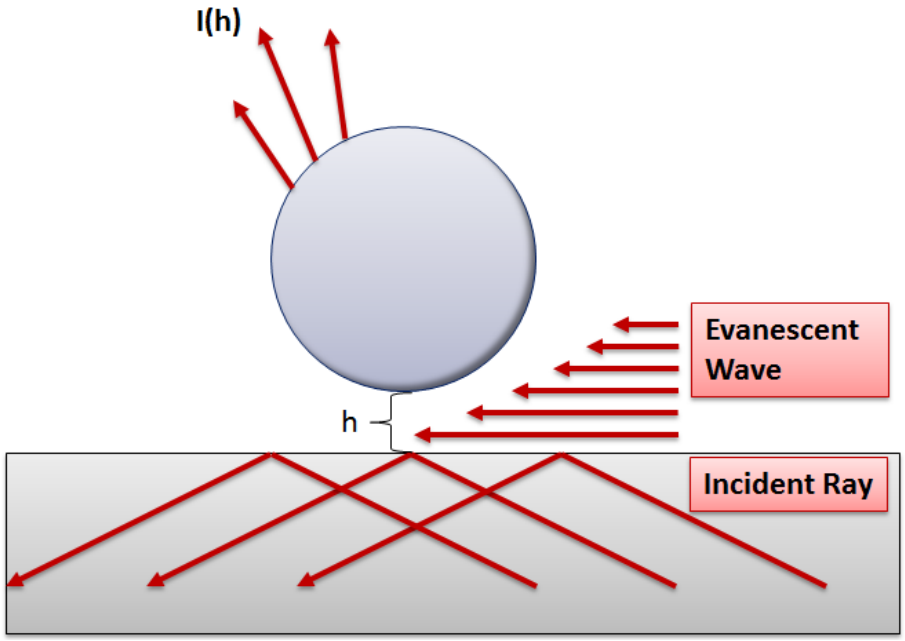

Fig. 4.1. A colloidal particle scattering light from the evanescent light wave adjacent a clear electrode surface. The evanescent wave forms when incident laser light strikes the interface at an angle greater than the critical angle of that interface. The intensity of light scattering I(h) increases with decreasing particle-wall separation h.

Upon interacting with the colloidal particle, light from the evanescent wave is scattered away from the electrode with an intensity that decays exponentially with the particle-wall separation h. This intensity, measurable by means of a photomultiplier tube (PMT) or CCD camera, is given by:

$$\frac{I(h)}{I_m} = \exp[\beta(h_m - h)] \qquad (4.23)$$

where I(h) and I_m are the scattering intensities of a single particle at heights h and h_m, respectively, and β^{-1} is the decay length of the evanescent wave. The parameter h_m is the most probable (mode) height of the particle above the interface at open circuit and I_m is the scattering intensity at that height.

In this study, the measured intensities are averaged over ensembles of particles, but the discussion of the theory involved focuses on the interactions between electrodes and single particles. The relationship between scattering intensities measured from single particles and ensembles of particles as it pertains to the imaging ammeter has been explored in previous work, as described in Chapter 3. [25] The correction described therein to allow for the use of ensemble average measurements in equations derived for single particles is applied to the data presented here.

4.2.1 Relationship between particle motion and electric field strength

Consider the charged particle and electrode system pictured in Fig. 4.2, where the zeta potentials of the particle (ζ_p) and wall (ζ_w) are both negative. In the absence of an applied electric field, the weight of the particle is defined as

$$F_g = -\frac{4}{3}\pi a^3(\rho_p - \rho_f)g = -G \qquad (4.24)$$

where ρ_p and ρ_f are the density of the particle and the fluid, respectively, a is the radius of the particle and g is the acceleration due to gravity. This force will act to pull the dense particle down towards the electrode surface. Once the particle approaches to close proximity with the surface, the double-layer repulsion between the two surfaces becomes significant, given by:

$$F_{es} = \kappa B exp(-\kappa h) \qquad (4.25)$$

where κ^{-1} is the Debye length of the electrolyte, G is the net weight of the particle, and B is the electrostatic parameter approximated as

$$B = 64\pi\varepsilon a\left(\frac{k_B T}{e}\right)^2 \tanh\left(\frac{e\zeta_p}{4k_B T}\right)\tanh\left(\frac{e\zeta_w}{4k_B T}\right) \qquad (4.26)$$

where ε is the permittivity of the medium. When the particle is at its equilibrium position in the absence of an electric field h_m, the force of gravity on the particle

and the double layer force balance each other, resulting in an equilibrium particle-wall separation of some hundreds of nanometers.

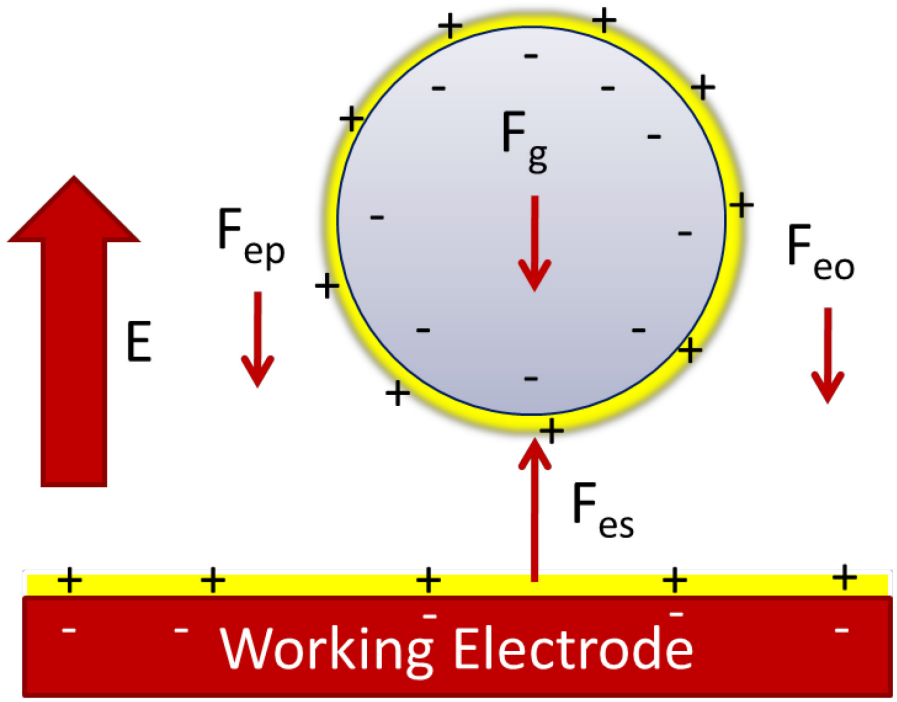

Fig. 4.2. Schematic of the particle-electrode system, where ζ_p and ζ_w are negative. Electrostatic repulsion pushes the particle away from the electrode while gravity pulls the particle down. With E > 0 as shown here, the electrokinetic forces F_{eo} and F_{ep} both pull the particle down towards the electrode surface. If E < 0, these forces would reverse direction as well.

When an electric field E_∞ is imposed across the electrochemical cell, additional forces act on the charged particle, as shown in Fig. 4.4 for the case where E_∞ is positive. We denote the new most-probable height as h'_m where

$$F_g + F_{es}(h'_m) + F_{ep}(h'_m, E_\infty) + F_{eo}(h'_m, E_\infty) = 0 \quad (4.27)$$

In this work, a prime on the variable denotes a quantity measured or inferred in the presence of a non-zero electric field. The sign convention adopted for the forces in Eq. 4.5 is that any force or E_∞ directed away from the electrode is positive. F_{eo} and F_{ep} refer to the electrokinetic forces acting on the particle from fluid flow originating at the electrode and at the particle, respectively. Previous work by Keh & Lien[30] and Yariv[31] has demonstrated that these forces are strong functions of the kinetics of the electrode reaction occurring below the particle; for a given electric field strength, the force on the particle in the case of fast electrode kinetics may differ from the force on the particle in the case of slow electrode kinetics by an order of magnitude.[32] These studies involve analytical solutions for the force on the particle in two limiting cases of electrode kinetics: infinitely fast kinetics, which results in a uniform potential at the electrode, and infinitely slow kinetics, which results in a uniform current density at the electrode. Recent computational studies of the system allows for scaling between these two limiting cases, as seen in Chapter 2.[24] Dimensionless parameters J and δ, can be used to define the current distribution:[33,34]

$$J \equiv \frac{(\alpha_a+\alpha_c)ae}{\sigma k_B T} i_0 \tag{4.28}$$

$$\delta \equiv \frac{(\alpha_a+\alpha_c)ae}{\sigma k_B T} i_{avg} \tag{4.29}$$

where α_a and α_c are the coefficients of symmetry for the anodic and cathodic reactions, respectively, i_0 is the exchange current density, e is the elementary charge and i_{avg} is the actual current density far from the particle. J and δ are therefore dimensionless current densities. In the limit of J ≫1 or δ ≫1, the potential is uniform on the electrode under the particle because the electrode kinetics are facile. In the opposite limit of J ≈ δ ≪ 1, the current density (instead of the potential) becomes increasingly uniform under the particle. For the purposes of this study, values of J=2 and δ=0.005 are assumed, corresponding to the small current densities present in these studies and an intermediate exchange current density at the electrode. This assumption results in the following form for F_{eo} and F_{ep}, as fit from the computational results presented in Chapter 2:[24]

$$F_{eo}(h) = \varepsilon a \zeta_w E_\infty \frac{1.459}{\left(\frac{h}{a}+0.02110\right)^{1.3}} \qquad (4.30)$$

$$F_{ep}(h) = \varepsilon a \zeta_p E_\infty \frac{11.82}{\left(\frac{h}{a}+0.1002\right)^{1.3}} \qquad (4.31)$$

Summing these expressions to obtain a force balance on the particle gives

$$F_g + F_{es}(h'_m) + F_{ep}(h'_m, E_\infty) + F_{eo}(h'_m, E_\infty) = 0 \qquad (32)$$

which can be used to determine the electric field strength E_∞ with known physical parameters and particle-wall separation during cell polarization h'_m, using the method outlined in Chapter 3.[25]

4.3 Methods & Materials

A sketch of the apparatus appears in Fig. 4.3. To obtain evanescent wave illumination over macroscopic electrodes, adjustments were made to the standard TIRM methodology, which is generally used to illuminate particles across a comparatively small field of view. First, the beam from a 30 mW, 632.8 nm HeNe laser with a 0.8 mm spot diameter was expanded through a 3x Edmund Optics beam expander, and then formed into an ellipse with a pair of anamorphic prisms, giving beam dimensions of 2.4 mm by 11 mm. In addition to this expanded laser beam, a new TIRM cell was designed in which the bottom glass slide (n=1.5) electrode acts as a waveguide for the laser light, as seen in Fig. 4.3. The laser enters the cell normal to a equilateral prism made from F2 glass(n=1.63), resulting in an incident angle at the electrode surface of 70°. This gives an evanescent wave decay length of $\beta^{-1} = 111$ nm, which is comparable to the evanescent wave decay length used in other studies.[23,35,36] Repeated total internal reflection of the laser beam within glass slide results in the formation of evanescent waves at each region of contact with the top or bottom of the slide. With proper alignment and laser spot shape, this result in an evanescent wave present across the entire surface of the electrode, allowing for imaging of particles across the surface. In this study, the input laser was masked, reducing the size of

the initial laser spot in order to eliminate undesired additional reflections and background signal.

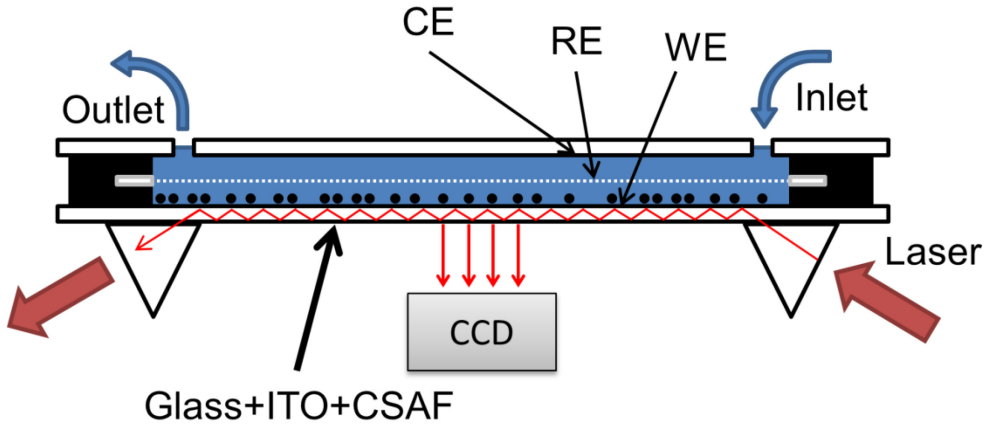

Fig. 4.3. Schematic of the TIRM cell used in these experiments. Laser light enters from the right, normal to the surface of a equilateral F2 glass prism. The bottom glass slide electrode acts as a waveguide for the laser beam, which reflects down the length of the cell and exits through another equilateral prism. The light scattering from the particles interacting with the evanescent wave adjacent the working electrode is collected by a CCD camera beneath the cell.

The working electrode (WE) present in this cell was a transparent 30-60 nm ITO coated glass slide(Sigma-Aldrich), with a Ni/Fe CSAF deposited on top using a rotatable shadow mask apparatus.[29] Measurements of composition of the CSAF were performed via energy dispersive X-ray (EDX) analysis. The reference electrode (RE) was a Ag/AgCl gasket ring, which was sandwiched by 1/32" Buna-N-Rubber gaskets to provide a seal. The counter electrode (CE) was gold, electrodeposited onto copper plate. Voltage sweeps were performed using a Princeton Applied Research versaSTAT3 potentiostat, which also recorded the gross current passing through the entire working electrode. Images of the light scattering from the particles as a function of applied voltage were captured with a DAGE-MTI CCD100 video camera, attached to an Edmund Optics zoom lens set

to 1x magnification, and digitized with a USB Live 2 Analog Video Digitizer. The measured intensities were averaged over 10 cycles of a cyclic voltammogram, with a scan rate of 100 mV/s. Video was taken of the light scattering from particles over a rectangular region of the CSAF electrode representing alloy compositions between 20% Fe and 100% Fe. Measured intensities were averaged over patch regions of two sizes: the data were processed by averaging intensities around each point in a circle of radius 100 μm with a pillbox filter, alternatively, intensities were averaged over patch regions of 100 μm × 1 mm, with each patch containing alloy compositions over a range of approximately 2.5%. The current was calculated from these average intensity measurements in the manner described in Chapter 3.

The particles were IDC™ sulfonated latex (Life Technologies) electrostatically stabilized by covalently attached sulfonate groups in the absence of surfactant, giving a corresponding zeta potential of approximately ζ_p=-120 mV. The particles had nominal diameters of 10.1±0.5 μm.

4.4 Results & Discussion

The first step in this study of the Ni/Fe alloy system for the oxygen evolution reaction in base was to deposit a CSAF onto the ITO coated glass slide. A schematic showing the location of the CSAF on the electrode surface, as well as the composition map of that CSAF obtained with EDX, is shown in Fig. 4.4. The dotted red rectangle represents the region imaged in this study.

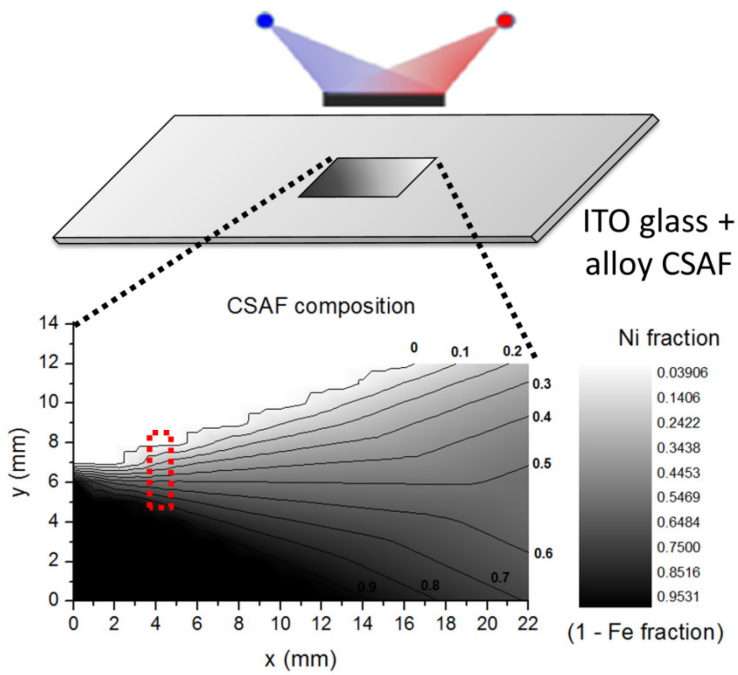

Fig. 4.4. Schematic of the working electrode surface with the Ni/Fe CSAF deposited on top. The CSAF was deposited in the middle of the glass slide, as pictured here. The composition on the CSAF surface are shown below. The red dotted rectangle represents the region over which imaging was performed in this study. Thanks to Matthew Payne for deposition and characterization of the CSAF electrode.

The light scattering at open circuit was first measured to determine the reference I_m at every location on the electrode. This image is shown in Fig. 4.5(a). By referencing the light scattering intensity during negative and positive

cell polarization (Figs. 4.5(b) and 4.5(e), respectively) to this open circuit intensity, it is possible to calculate current densities across the electrode surface, as shown in Figs. 4.5(c) and 4.5(f), again for negative and positive polarization. These currents were calculated using intensities averaged in a circle (r=100μm) about each point. The irregular nature of the currents seen in Fig. 4.5(f) is likely due to a combination of unaccounted-for background signal, non-uniformity in the particle distribution on the surface, and insufficient signal/noise of the camera itself. All of these concerns will be addressed in future work, but to allow for more reliable mapping of the current density based on these data, patch averaging of the intensity signal was performed for strips of 1×5 mm^2, resulting in the current densities shown in Figs. 4.5(d) and 4.5(g).

One important feature to note in Fig. 4.5(a) is the non-uniformity of the illumination across the 1×5 mm^2 region with no applied electric field. This is due to a combination of the Gaussian nature of the laser beam intensity profile and the varying surface opacity of the electrode. This should have no impact on the currents calculated from the measured light scatter, since the current is calculated on the basis of changes in the light scattering, not with the absolute intensity. This effect is clear when comparing Fig. 4.5(e) to Fig. 4.5(f): while the absolute intensity on the top of the frame is greater, the current density is at a maximum near the bottom of the frame, since this is where the ratio of the intensity shown in Fig. 4.5(e) to the open circuit intensity in Fig. 4.5(a) is largest.

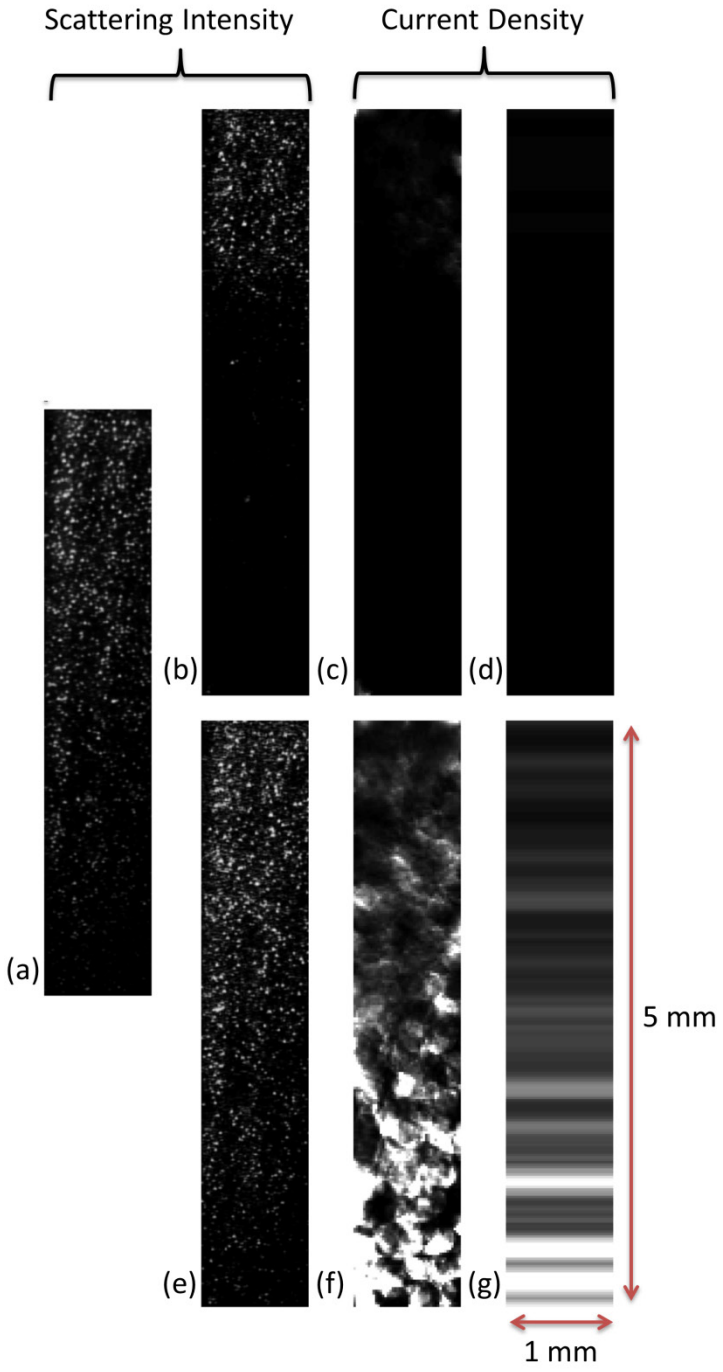

Fig. 4.5. Scattering intensities and current densities over the region of interest. (a) Light scattering intensity at open circuit. (b), (e) Light scattering during negative and positive polarization, respectively. (c), (f) Current density calculated with circular pillbox averaging during negative and positive polarization, respectively. (d), (g) Current density calculated averaging over 1×5 mm^2 patch regions during negative and positive polarization, respectively. In (c), (d), (f) and (g), lighter regions indicate greater positive current, with a maximum of 1 A/m^2.

Current densities were calculated from measured light scattering at different locations in the red window pictured in Fig. 4.4 as a function of CSAF composition. One way to display these data is shown in Fig. 4.6, where the current data for three different alloy compositions are plotted as a function of applied potential for the upward sweep up the CV experiments. The average current density of the entire electrode surface, measured electronically with a potentiostat, is also plotted for comparison.

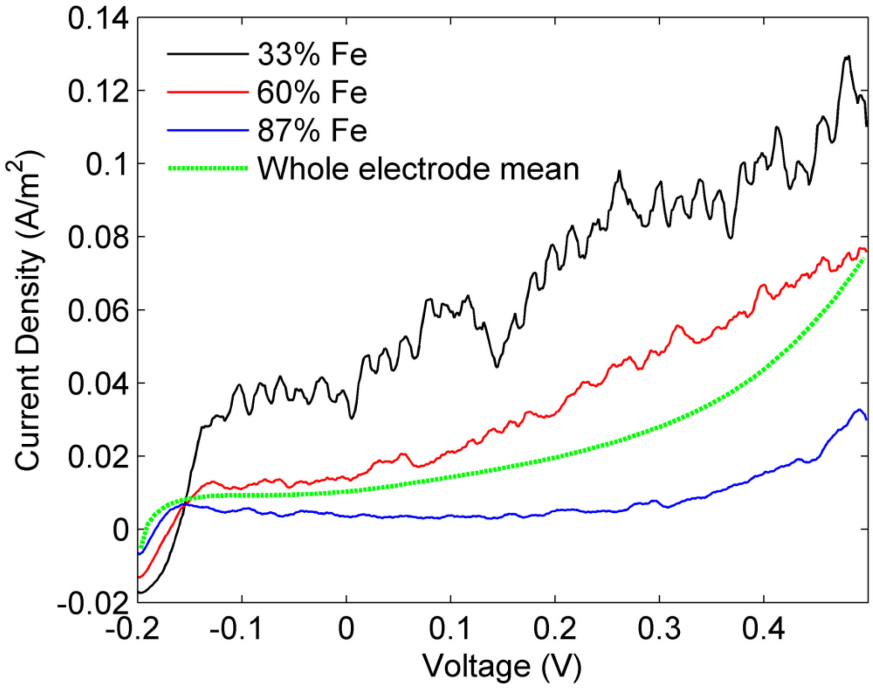

Fig. 4.6. Current densities inferred from light scatter measurements as a function of applied voltage for the upwards sweep of a CV, averaged over ten cycles, for three different alloy compositions are plotted here. Also plotted in green is the mean current density across the entire electrode surface, measured electronically.

Over this range of alloy compositions, it is expected that the electrochemical activity should increase with decreasing iron content, and indeed that is the trend observed the current densities inferred from the motion of the particles adjacent the CSAF electrode. The mean current density across the entire electrode is between the two extremes plotted here, which is not surprising, as the average surface makeup of the electrode is some intermediate between 100% Fe and 100% Ni.

Polarizations probed in this study were not sufficiently large to reliably obtain Tafel parameters from the inferred current densities, so other measures were used to quantify the activity of the electrode surface as it relates to electrode alloy composition. One way to examine the activity of the electrode for varying alloy compositions is to plot the maximum current density observed as a function of composition. These data are shown in Fig. 4.7, plotted against data from Landon et al.[28], who tested electrodes synthesized using several different methods over a wide range of compositions. The data are not quantitatively comparable, as the currents from Landon et al. is the current density per mg substrate at a fixed overpotential as opposed to maximum current densities per area, but they are plotted together nevertheless to illustrate the qualitative agreement between previously established trends in electrochemical activity and the data obtained with the imaging ammeter. Despite the scatter in the data plotted here, the upward trend in current density with decreasing iron content over the range of 30-100% iron is clear.

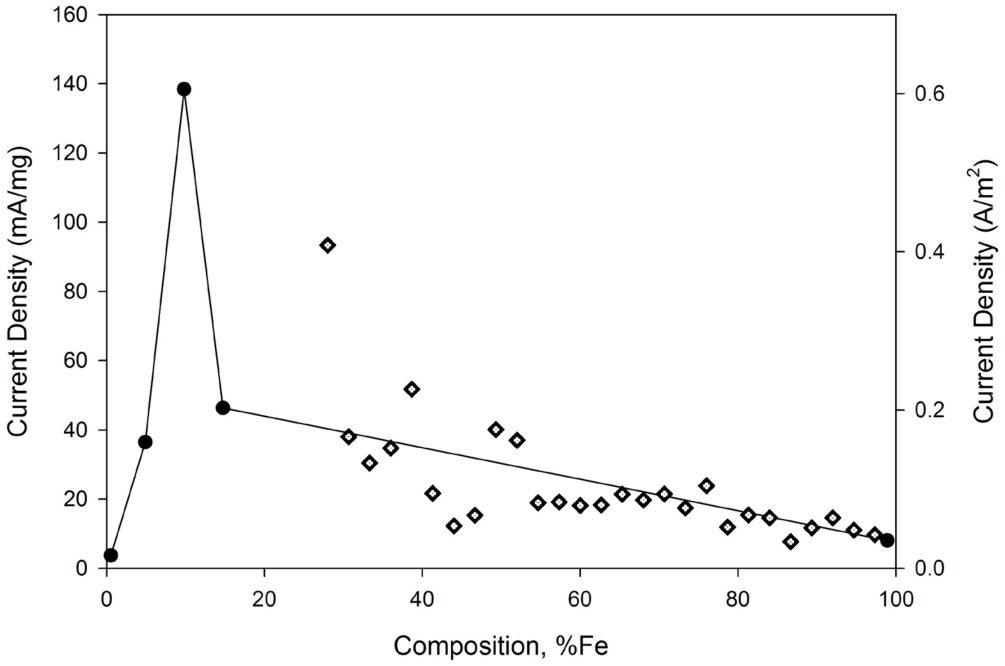

Fig. 4.7. The maximum current densities during the CV experiments described here, inferred from light scattering measurements, as a function of electrode composition, plotted as diamonds against the right ordinate axis. Also plotted against the left ordinate axis are current densities at a fixed overpotential of 360 mV on an alloy oxide electrode coated onto a nickel mesh support, as described by Landon et al.[28] Both current densities trend downwards with increasing iron content in the electrode, above 20% iron. Axis scaling is arbitrary, and was chosen to illustrate the qualitative agreement between the two data sets.

There is some noise present in the plots shown in Figs. 4.5 and 4.7. While these errors do not detract significantly from the overall trend observed in this study, future studies will demand measures to address the underlying issues causing this. One reason for this noise is insufficient light scattering intensity at certain locations on the electrode. Given a large number of particles scattering light on the electrode in the absence of an electric field, variations in the light

scattering intensity are due predominantly to variations in the incident laser light, governed by the Gaussian nature of the original beam, and variations in the opacity of the electrode itself, both of which impact the intensity of the evanescent light. In theory, the light scattering is referenced to the constant I_m as shown in Eq. 4.1, meaning that variations in the intensity of the evanescent wave should have no impact on inferred particle heights and current densities. In practice, however, imperfect collection of the light scattering from the particles means that insufficient illumination of the particles can lead to unreliable calculation of current density from light scattering measurements. Possible solutions to this issue include the purchase and use of a more sophisticated camera for image acquisition and deposition of thinner CSAF films to reduce the variations in surface opacity. Another possible cause for the noise in the plots presented here is the misinterpretation of light scattering from blemishes on the surface or "stuck" particles, which results in a background light intensity. Addressing these issues calls for adjustments to the experimental protocol, to include acquisition of a background intensity image which can be subtracted out of subsequent measurements.

Additionally, smaller particles should be used in the future when working with CSAF surfaces that have lesser surface charge than the ITO films traditionally used for TIRM. Shortly after the data presented here were collected, the 10.1 μm particles here irreversibly adsorbed to the surface due to Van der Waals interactions, limiting the amount of data that was collected. Using the correction factors for intensity described in Chapter 3 allows for the reliable use

of smaller particles, which have a lesser tendency to adsorb to the surface given their smaller weight. Use of 4 to 6 μm diameter particles should be sufficient to avoid these issues in the future.

It is also important to note that a single set of kinetic parameters (J and δ) were assumed when calculating the electrokinetic forces in this experiment, and that this may be a source of error, considering the fact that the actual exchange current density will be varying as a function of alloy composition. Future work should include some effort to address this issue. Options include deposition of a "standard" material somewhere on the electrode, or imaging of the entire active area of the electrode to allow for fitting of the total current to externally measured data.

4.5 Conclusions

The oxygen evolution reaction on a Ni/Fe alloy surface was explored here, using colloidal imaging amperometry to determine the current density across compositions ranging between 20% Fe and 100% Fe in a single experiment. This was achieved by imaging the motion of colloidal particles proximate to a composition spread alloy film electrode during cell polarization and inferring the current density at each location on the electrode through the application of a force balance. Inferred currents agree with established trends in the electrochemical activity of this alloy system as a function of alloy composition. This work represents the proof-of-concept for the macroscopic colloidal imaging ammeter. Future advancements in the method include adjustments to the experimental

protocol and some equipment upgrades, which will make future work focusing on more complex systems with subtler behavior possible.

4.6 Acknowledgements

The authors would like to acknowledge support from The National Science Foundation under CBET 1133082, as well as Matthew Payne for providing the means and expertise to deposit and map the composition of the CSAF film tested here.

4.7 Appendix

The current density calculations performed here were done with the same methodology as that presented in Chapter 3, with the major difference being the manner in which the data was collected. The function used to open and filter the video files into a format usable in MATLAB is included below.

```
function [filt_vid] = CCvidHandlingSqueezeStrip(fileName,
filterType, squeezeFactor, startZ, endZ)

%{
This function reads in the video file designated by filename,
converts the
data to single format and applies a filter of filterType to the
data.

Example filter: filterType = fspecial('disk',filterRadius);
This will apply an averaging circular filter around each point in
the
matrix

squeezeFactor allows for data reduction *after* the filtering is
performed.
 The size of the matrix output is original_x/squeezeFactor by
 original_y/squeezefactor

startZ and endZ allow for cutting data out of the video output on
the top
and bottom of the video
%}
```

```
[video, audio] = mmread(fileName, [],[])
vidSize =
size(squeezeFrame(im2single(video.frames(1,1).cdata(startZ: endZ-
1,1:end-10,1)),squeezeFactor));
tempVid = zeros(vidSize(1),vidSize(2), video.nrFramesTotal,
'single');

for i_=1:video.nrFramesTotal
    temp = im2single(video.frames(1,i_).cdata(startZ:endZ-
1,1:end-10,1)); %im2double converts image format data to double
    tempVid(:,:,i_) = squeezeFrame(imfilter(temp, filterType,
'replicate'),squeezeFactor);
end

filt_vid = tempVid;


function [smallImg] = squeezeFrame(myImg, squeezeFactor)
%  This section reduces the size of the image to one where each
dimension
%  of size=n is n/squeezeFactor

rowsNotRemoved = 1 : squeezeFactor : size(myImg,1);
colsNotRemoved = 1 : squeezeFactor : size(myImg,2);

rowsRemoved = 1:size(myImg,1);
colsRemoved = 1:size(myImg,2);

rowsRemoved(rowsNotRemoved) = [];
colsRemoved(colsNotRemoved) = [];

myImg(rowsRemoved,:)=[];
myImg(:,colsRemoved)=[];

smallImg = myImg;
```

4.8 Works Cited

(1) Smotkin, E. S.; Diaz-Morales, R. R. *Annu. Rev. Mater. Res* **2003**, *33*, 557–79.

(2) Klemm, S. O.; Kollender, J. P.; Walter Hassel, A. *Corrosion Science* **2011**, *53*, 1–6.

(3) Mardare, A. I.; Yadav, A. P.; Wieck, A. D.; Stratmann, M.; Hassel, A. W. *Science and Technology of Advanced Materials* **2008**, *9*, 035009.

(4) Reddington, E. *Science* **1998**, *280*, 1735–1737.

(5) Prochaska, M.; Jin, J.; Rochefort, D.; Zhuang, L.; DiSalvo, F. J.; Abruña, H. D.; Van Dover, R. B. *Review of Scientific Instruments* **2006**, *77*, 054104.

(6) Jin, J.; Prochaska, M.; Rochefort, D.; Kim, D.; Zhuang, L.; Disalvo, F.; Vandover, R.; Abruna, H. *Applied Surface Science* **2007**, *254*, 653–661.

(7) Barber, Z. H.; Blamire, M. G. *Materials Science and Technology* **2008**, *24*, 757–770.

(8) Priyadarshini, D.; Kondratyuk, P.; Miller, J. B.; Gellman, A. J. *Journal of Vacuum Science & Technology A: Vacuum, Surfaces, and Films* **2012**, *30*, 011503.

(9) Muster, T. H.; Hughes, a. E.; Furman, S. a.; Harvey, T.; Sherman, N.; Hardin, S.; Corrigan, P.; Lau, D.; Scholes, F. H.; White, P. a. *Electrochimica Acta* **2009**, *54*, 3402–3411.

(10) Jiang, R. *The Review of Scientific Instruments* **2007**, *78*, 072209.

(11) Spong, a *Journal of Power Sources* **2003**, *119-121*, 778–783.

(12) Mardare, A. I.; Ludwig, A.; Savan, A.; Wieck, A. D.; Hassel, A. W. *Electrochimica Acta* **2009**, *54*, 5171–5178.

(13) Whitacre, J. F.; Valdez, T. I.; Narayanan, S. R. *Electrochimica Acta* **2008**, *53*, 3680–3689.

(14) Russell, A. E. *Physical Chemistry Chemical Physics : PCCP* **2008**, *10*, 3607–8.

(15) Muster, T. H.; Trinchi, a.; Markley, T. a.; Lau, D.; Martin, P.; Bradbury, a.; Bendavid, a.; Dligatch, S. *Electrochimica Acta* **2011**, *56*, 9679–9699.

(16) Williams, C. G.; Edwards, M. a; Colley, A. L.; Macpherson, J. V; Unwin, P. R. *Analytical chemistry* **2009**, *81*, 2486–95.

(17) Engstrom, R. C.; Ghaffari, S.; Qu, H. *Anal. Chem.* **1992**, 2525–2529.

(18) Bowyer, W. J.; Xie, J.; Engstrom, R. C. *Anal. Chem.* **1996**, *68*, 2005–9.

(19) Panova, A. A.; Pantano, P.; Walt, D. R. *Anal. Chem.* **1997**, *69*, 1635–41.

(20) Lohrengel, M. M.; Moehring, A.; Pilaski, M. *Electrochimica Acta* **2001**, *47*, 137– 141.

(21) Lohrengel, M. M.; Moehring, A.; Pilaski, M. *Fresenius' Journal of Analytical Chemistry* **2000**, *367*, 334–9.

(22) Sides, P. J.; Wirth, C. L.; Prieve, D. C. *Electrochemical and Solid-State Letters* **2010**, *13*, F10–F12.

(23) Wirth, C. L.; Sides, P. J.; Prieve, D. C. *Journal of Colloid and Interface Science* **2011**, *357*, 1–12.

(24) Rock, R. M.; Sides, P. J.; Prieve, D. C. *Journal of Colloid and Interface Science* **2013**, *393*, 306–13.

(25) Rock, R. M.; Sides, P. J.; Prieve, D. C. Ensemble Average TIRM for Imaging Amperometry. DOI: 10.1016/j.jcis.2013.04.010 **2013**.

(26) Krstajić, N.; Trasatti, S. In *Oxygen Electrochemistry*; Adzic, R.; Anson, F.; Kinoshita, K., Eds.; The Electrochemical Society, 1996; pp. 155–165.

(27) Guerrini, E.; Trasatti, S. In *Catalysis for Sustainable Energy Production*; 2009; pp. 235–269.

(28) Landon, J.; Demeter, E.; Nilay, I.; Keturakis, C.; Wachs, I. E.; Vasic, R.; Frenkel, A. I.; Kitchin, J. R. *ACS Catalysis* **2012**, *2012*, 1793–1801.

(29) Fleutot, B.; Miller, J. B.; Gellman, A. J. *Journal of Vacuum Science & Technology A: Vacuum, Surfaces, and Films* **2012**, *30*, 061511.

(30) Keh, H.-J.; Lien, L.-C. *J. Chin. Inst. Chem. Eng.* **1989**, *20*, 283–290.

(31) Yariv, E. *Journal of Fluid Mechanics* **2010**, *645*, 187.

(32) Solomentsev, Y.; Bohmer, M.; Anderson, J. L. *Langmuir* **1997**, *13*, 6058–6068.

(33) Newman, J. *Journal of The Electrochemical Society* **1966**, *113*, 1235.

(34) Newman, J.; Thomas-Alyea, K. E. *Electrochemical Systems*; 3rd ed.; John Wiley & Sons, Inc.: Hoboken, NJ, 2004.

(35) Fagan, J. A.; Sides, P. J.; Prieve, D. C. *Langmuir* **2002**, *18*, 7810–7820.

(36) Prieve, D. C.; Sides, P. J.; Wirth, C. L. *Current Opinion in Colloid & Interface Science* **2010**, *15*, 160–174.

Chapter 5

Summary and Future Directions

5.0 Summary

The work presented in this dissertation advances theory and experimental methods to test the following hypothesis:

Colloidal particles can be used as probes of electrochemical current across planar composition spread alloy film electrodes to enable rapid parallel screening of novel electrocatalysts. This method will allow for accurate, reaction-independent, high resolution testing of alloy materials.

This effort yielded three major contributions. (1) A computational exploration of the impact of electrode reaction kinetics on the electrokinetic forces acting on particles proximate to the electrode surfaces. This work is of general interest to the electrophoretic deposition community, and resulted in a much more sophisticated understanding of the relationship between electric fields and the resulting forces acting on the particles. (2) Theoretical and experimental advances to allow for application of this method to average measurements taken over ensembles of particles. This was a necessary step to adapt from previous work, which focused on relating the motions of a single particle to the electric field local to that particle. (3) Application of these advances to measure the current density as a function of applied potential across a Fe/Ni CSAF electrode. This represents the proof-of concept for the macroscopic imaging ammeter, and would not have been possible without the previous work outlined here.

5.1 Future Directions

There are a number of opportunities for future work on the imaging ammeter. The initial alloy electrode experiments described in Chapter 4 explore the electrochemical response of a Fe/Ni alloy surface undergoing the oxygen evolution reaction (OER) for compositions ranging from 20% Fe to 100% Fe, which unfortunately does not capture the region of greatest interest in this system, between 0% and 30% Fe content. Near future work should undertake further characterization of this system to provide more concrete validation of the method for macroscopic imaging amperometry. The refinements in the experimental method described here will provide for more reliable data collection and analysis going forward.

The imaging ammeter has matured to the point that it can be used to probe technologically relevant alloy systems to determine ideal alloy compositions. Expansion of the current work to alloy systems such as $Fe_{1-x-y}Ni_xCo_y$ or $Fe_{1-x-y}Ni_xMn_y$ for oxygen evolution is a natural progression of the work presented here. Alternatively, different reactions and alloy systems could be probed with some adjustments to the experimental method. A primary strength of the colloidal imaging ammeter is that the method can be used to infer current density regardless of electrolyte chemistry, so long as the surface and particles have sufficient like charge to maintain particle levitation. Probing cathodic reactions reaction as opposed to the anodic oxygen evolution reaction, for example, would require the use of positively charged particles and an acidic electrolyte, but would

be procedurally identical to the experiments described here. Corrosion resistant materials could also be probed using this method.

5.2 Qualifications and Limitations

The authors believe ensemble average TIRM for macroscopic imaging amperometry is a viable technique for high throughput testing of alloy electrocatalyst materials. Using colloidal particles as probes of electrochemical current allows for imaging measurement of current density for a wide variety of electrode materials, electrolytes and electrode chemistries. Some limitations of the method should be explicitly noted, however, to allow for effective application of the method in future work. The primary limitation of TIRM is the necessity of a clear electrode to allow for formation of the evanescent wave that facilitates particle motion measurement. As a result of this, electrode films used for testing must be very thin (<10 nm) and smooth, which can make electrode deposition and characterization difficult. The electrostatic levitation of colloidal particles over the electrode also necessitates the use of very dilute electrolytes in comparison to those used in traditional electrochemical methods, and limits the method to small current densities, as the electrokinetic forces that result from large current densities can be large enough to irreversibly deposit particles onto the electrode surface. High current densities and prolonged experiments must also be avoided, as this can also result in changing of the ionic strength in the vicinity of the electrode. Despite these drawbacks, the authors believe there is much promise for this method.